

1997

The preparation, characterization, and application of thin film devices.

Bob. Berno
University of Windsor

Follow this and additional works at: <http://scholar.uwindsor.ca/etd>

Recommended Citation

Berno, Bob., "The preparation, characterization, and application of thin film devices." (1997). *Electronic Theses and Dissertations*. Paper 4173.

This online database contains the full-text of PhD dissertations and Masters' theses of University of Windsor students from 1954 forward. These documents are made available for personal study and research purposes only, in accordance with the Canadian Copyright Act and the Creative Commons license—CC BY-NC-ND (Attribution, Non-Commercial, No Derivative Works). Under this license, works must always be attributed to the copyright holder (original author), cannot be used for any commercial purposes, and may not be altered. Any other use would require the permission of the copyright holder. Students may inquire about withdrawing their dissertation and/or thesis from this database. For additional inquiries, please contact the repository administrator via email (scholarship@uwindsor.ca) or by telephone at 519-253-3000ext. 3208.

INFORMATION TO USERS

This manuscript has been reproduced from the microfilm master. UMI films the text directly from the original or copy submitted. Thus, some thesis and dissertation copies are in typewriter face, while others may be from any type of computer printer.

The quality of this reproduction is dependent upon the quality of the copy submitted. Broken or indistinct print, colored or poor quality illustrations and photographs, print bleedthrough, substandard margins, and improper alignment can adversely affect reproduction.

In the unlikely event that the author did not send UMI a complete manuscript and there are missing pages, these will be noted. Also, if unauthorized copyright material had to be removed, a note will indicate the deletion.

Oversize materials (e.g., maps, drawings, charts) are reproduced by sectioning the original, beginning at the upper left-hand corner and continuing from left to right in equal sections with small overlaps. Each original is also photographed in one exposure and is included in reduced form at the back of the book.

Photographs included in the original manuscript have been reproduced xerographically in this copy. Higher quality 6" x 9" black and white photographic prints are available for any photographs or illustrations appearing in this copy for an additional charge. Contact UMI directly to order.

UMI

**A Bell & Howell Information Company
300 North Zeeb Road, Ann Arbor MI 48106-1346 USA
313/761-4700 800/521-0600**

NOTE TO USERS

The original manuscript received by UMI contains pages with indistinct and/or slanted print. Pages were microfilmed as received.

This reproduction is the best copy available

UMI

**THE PREPARATION, CHARACTERIZATION, AND
APPLICATION OF THIN FILM DEVICES**

by

Bob Berno

A Dissertation

**Submitted to the Faculty of Graduate Studies and Research
through the Department of Chemistry and Biochemistry
in Partial Fulfilment of the Requirements for
the degree of Doctor of Philosophy
at the University of Windsor**

Windsor, Ontario, Canada

1996

©1996 Bob Berno



**National Library
of Canada**

**Acquisitions and
Bibliographic Services**

395 Wellington Street
Ottawa ON K1A 0N4
Canada

**Bibliothèque nationale
du Canada**

**Acquisitions et
services bibliographiques**

395, rue Wellington
Ottawa ON K1A 0N4
Canada

Your file Votre référence

Our file Notre référence

The author has granted a non-exclusive licence allowing the National Library of Canada to reproduce, loan, distribute or sell copies of this thesis in microform, paper or electronic formats.

The author retains ownership of the copyright in this thesis. Neither the thesis nor substantial extracts from it may be printed or otherwise reproduced without the author's permission.

L'auteur a accordé une licence non exclusive permettant à la Bibliothèque nationale du Canada de reproduire, prêter, distribuer ou vendre des copies de cette thèse sous la forme de microfiche/film, de reproduction sur papier ou sur format électronique.

L'auteur conserve la propriété du droit d'auteur qui protège cette thèse. Ni la thèse ni des extraits substantiels de celle-ci ne doivent être imprimés ou autrement reproduits sans son autorisation.

0-612-30269-5

Canada

Abstract

This thesis deals with the preparation of two thin film devices, in particular a nitrogen dioxide (NO_2) gas sensor and a rechargeable lithium battery. A number of different thin film preparation techniques were used for a variety of applications and the resultant films were characterized by spectroscopic and electrochemical methods.

The NO_2 gas sensor was based on Langmuir-Blodgett (LB) monolayer films of the sandwich molecule europium bisphthalocyanine (EuPc_2). The intense UV-visible absorption spectrum of a monolayer of the EuPc_2 dye molecules was recorded before and after exposure to NO_2 gas. It was noted that with time the film spectrum returned to its original colour, thus indicating the process to be reversible. The powerful spectroscopic technique of surface enhanced Raman scattering (SERS) was also utilized for film characterization. As with the absorption spectroscopy, the SERS experiments also indicated a reversible NO_2 adsorption-desorption process.

An interdigitated gold electrode was used to measure the electrical conductivity of LB monolayers of EuPc_2 . The activation energy for conduction for this molecular semiconductor was determined to be 0.27 eV from thermal conductivity experiments. Upon exposure to NO_2 gas, the conductivity of the film increases considerably until it reaches saturation. Kinetics studies indicated that the conductivity changes resulted from two sources: the adsorption of NO_2 molecules on the surface, and the absorption of the molecules into the film. While the spectroscopic experiments suggested this process to be completely reversible, the electrical measurements indicated that heating was required to remove the residual absorbed NO_2 .

Thin film cathodes for a rechargeable lithium battery were fabricated by the magnetron sputtering technique. The cathodes were deposited from a sample of the LiMn_2O_4 pure spinel material. The Li-Mn-O film was characterized by grazing angle x-ray diffraction, Raman and infrared spectroscopies. Electrochemical analyses of the films deposited on aluminum gave charge/discharge capacities of around 78.9 mA h g^{-1} . Tests showed that these cells suffered from very high impedance most likely due to a

high degree of polarization at the cathode:substrate interface. Deposition of a gold film onto the aluminum substrate proved to greatly reduce the impedance losses, resulting in an improvement in the total charge capacity of the cathode film to 211 mA h g^{-1} .

**This work is dedicated to my parents,
Liberale and Maria,
whose unwavering love and support
have enabled me to continue to explore
the world.**

*"Trust me.
this will take time
but there is order here,
very faint, very human."*

From *In the Skin of a Lion*,
by Michael Ondaatje

Acknowledgements

As I sit here dotting the last of the “i’s” and crossing the final “t’s” of this dissertation, I am reminded of the many people who helped me through this ordeal known as a PhD. These people are too numerous to all be mentioned here now, but I do wish to highlight those whose contributions were critical.

First and foremost I wish to thank Dr. Ricardo Aroca. It may sound *cliché*, but without Dr. Aroca’s contribution, none of what follows could have been possible.

Next, I wish to thank two people whom I’ve never actually met: Dr. Najafi from the electrical engineering department of the University of Michigan, and Dr. Tomilova from Moscow State University. Dr. Najafi’s generous donation of the interdigitated electrodes made it possible to carry out the electrochemical gas sensor experiments on the phthalocyanine samples that were generously provided by Dr. Tomilova.

I would also like to thank all of the students and researchers who have worked with me in Dr. Aroca’s group at the University of Windsor. In particular I’d like to thank Barry for being a willing accessory during our many excursions to the grad house. And Wania whose *esprit de corps* bolstered the morale of the entire group even when the worst disasters struck. I am also deeply thankful to Andrew Ozarowski for the EPR studies.

I was very fortunate to have been able to spend some time studying in Spain, and I am indebted to Dr. Jose-Antonio deSaja from the Department of Condensed Matter Physics at the University of Valladolid for allowing me that privilege.

There were many people at the General Motors Research and Development Center who deserve special note here: Ian Hallalay, for his help with the electrochemical measurements, Blake (go Red Wings) Howie, for being a facilitator for so many odd jobs, Brian Gillispie, who was co-conspirator in the sputter deposition experiments, Y-T Cheng, without whose chamber Brian and I could not have made our films, and of course Abbas Nazri, who was always able to somehow find a few minutes to sit down with me to clarify things.

Table of Contents

Abstract	iii
Dedication	v
Acknowledgements	vii
List of Figures	x
List of Tables	xiii
List of Abbreviations	xiv
Chapter 1: Introduction	1
1.1 History of Oriented Molecular Monolayer Film Preparation	1
1.2 Background of Phthalocyanines	2
1.3 Introduction to Thin Film Microbatteries	4
Chapter 2: Thin Film Preparation Techniques	6
2.1 Thermal Evaporation in Vacuum	6
2.2 Magnetron Sputtering	8
2.3 The Langmuir-Blodgett Technique	13
Chapter 3: Preparation and Characterization of EuPc₂ Thin Films	17
3.1 Experimental	18
3.2 Langmuir-Blodgett Film Preparation	20
3.3 UV-Visible and Near-Infrared Absorption Spectra	21
3.4 Infrared Spectra	24
3.5 Raman and Resonance Raman	28
3.6 Surface Enhanced Raman Scattering	33
3.7 Conclusions	37

Chapter 4: Application of LB Films of EuPc₂ as an NO₂ Gas Sensor	38
4.1 Experimental	39
4.2 UV-Visible and SERRS Spectroscopy	41
4.3 Electrical Measurements	43
4.3.1 Thermal Conductivity of EuPc ₂ LB Films	45
4.3.2 Electrical Response of EuPc ₂ LB Films to NO ₂	48
4.4 Discussion of EPR Experiments	53
4.5 Conclusions	57
Chapter 5: Thin Film Lithium Microbattery	58
5.1 Introduction to Microbattery Research	58
5.2 Cathode Film Preparation	62
5.3 Characterization of the Cathode Thin Films	65
5.3.1 Grazing Angle X-ray Diffraction	65
5.3.2 Infrared and Raman Spectroscopy	67
5.4 Electrochemical Analyses of the Li-Mn-O Film	71
5.4.1 The Electrochemical Cell	71
5.4.2 Charge-Discharge Cycling	73
5.4.3 The Ratio of Charge:Discharge Capacity	76
5.4.4 Impedance Analyses of the Cell	77
5.5 Conclusions	80
Chapter 6: Summary	82
References	85
Vita Auctoris	90

List of Figures

1.1	Sketch of the metal-free phthalocyanine molecule.	3
2.1	Schematic diagram of the thermal evaporation system.	7
2.2	Illustration of the planar cathode discharge.	9
2.3	Illustration of magnetron sputter deposition.	10
2.4	Top view of the UHV magnetron sputter deposition chamber.	12
2.5	Diagram of a Langmuir trough equipped with a Langmuir Filmbalance	15
3.1	An illustration of europium bisphthalocyanine (EuPc_2).	18
3.2	The π -A isotherm of EuPc_2 at 15 °C.	20
3.3	The energy level diagram for 2Pc^{2-} and EuPc_2 .	21
3.4	The characteristic electronic transitions of EuPc_2 .	22
3.5	The UV-visible and near-IR spectra of EuPc_2 .	23
3.6	Diagram of thin film transmission infrared experiments.	25
3.7	The FTIR spectra of EuPc_2 .	26
3.8	The Raman spectra of EuPc_2 dispersed in KBr pellets.	29
3.9	The plasmon absorption spectra of: (a) a 6 nm silver island film, and (b) a 4nm gold island film.	34
3.10	The plasmon absorption spectrum of a 20 nm gold island film.	34
3.11	The SERS spectra of EuPc_2 LB monolayers.	35
4.1	Diagram of an interdigitated electrode.	39
4.2	Schematic diagram of the apparatus for mixing and controlling the NO_2/N_2 gas flow.	40
4.3	The UV-visible absorption spectra of LB monolayers of EuPc_2 before and after exposure to NO_2 .	42

4.4	The SERRS spectra of LB monolayers of EuPc ₂ before and after exposure to NO ₂ gas.	44
4.5	The test for Ohmic contact between the interdigitated gold electrode and the EuPc ₂ LB film.	45
4.6	Thermal conductivity measurements of an LB film of EuPc ₂ .	46
4.7	Analysis of the thermal conductivity data.	47
4.8	The electrical response from an LB film of EuPc ₂ to various concentrations of NO ₂ gas.	48
4.9	Elovich plots of adsorption and desorption of 24.9 ppm NO ₂ .	50
4.10	The response of the sensor to 105.8 ppm NO ₂ , demonstrating that heat was required to remove residual NO ₂ from the films.	51
4.11	The response of the gas sensor to various concentrations of NO ₂ at 500 K.	52
4.12	The sensor response to various gas concentrations after 5, 10, 15, and 20 minute intervals.	53
4.13	The EPR spectra of: (a) the pure EuPc ₂ compound, and (b,c) the same sample exposed to increasing amounts of NO ₂ gas.	54
4.14	The EPR spectra of a sample of GdPc ₂ at: (a) room temperature, and (b) at 100 K.	56
4.15	The temperature dependent EPR spectra of a sample of GdPc ₂ after exposure to NO ₂ gas.	57
5.1	The unit cell of the spinel, LiMn ₂ O ₄ .	60
5.2	One eighth of the unit cell of the LiMn ₂ O ₄ spinel.	61
5.3	The x-ray diffraction pattern of the target after sputter deposition.	64
5.4	The x-ray diffraction pattern of the same target material as in Figure 5.3 after reaction in oxygen atmosphere at 750 °C.	65
5.5	The grazing angle x-ray diffraction pattern for a 165 nm Li-Mn-O film deposited on a silicon wafer.	66
5.6	The FTIR spectra of: (a) a 165 nm Li-Mn-O film on silicon, and (b) the pure	

LiMn ₂ O ₄ powder in KBr.	67
5.7 The Raman spectrum of the pure LiMn ₂ O ₄ powder.	68
5.8 The Raman spectra of an Li-Mn-O film on silicon.	70
5.9 A sketch of the electrochemical cell used to test the cathode films.	72
5.10 A graph of the variation of the specific charge capacity versus voltage range.	73
5.11 The charge:discharge capacity of a 200 nm Li-Mn-O film over a number of cycles.	74
5.12 Plot of the specific charge capacity as a function of cycle number.	75
5.13 The charge:discharge capacity ration as a function of cycle number.	76
5.14 Plot of the real vs imaginary impedance for the cell.	77
5.15 The frequency dependent impedance measurements for the cell.	78
5.16 The impedance measurements for a 200 nm Li-Mn-O film on gold-aluminum alloy substrate.	79
5.17 The charge:discharge capacity of a 200 nm Li-Mn-O film deposited on the gold-aluminum alloy substrate.	80
5.18 The specific charge capacity of a 200 nm Li-Mn-O film deposited on a gold-aluminum alloy substrate.	81

List of Tables

3.1	Frequencies and band assignments of the FTIR spectra of EuPc_2 .	27
3.2	Raman spectral frequencies and band assignments of EuPc_2 .	30
3.3	List of the bands showing similar relative intensities under green and blue argon ion laser line excitations.	32
4.1	The activation energies of conduction for a variety of LnPc_2 complexes.	47
4.2	The EPR peak intensities for LuPc_2 and the $\text{LuPc}_2\text{-NO}_2$ adduct.	55
5.1	The list of Raman frequencies and relative intensities of the pure LiMn_2O_4 spinel powder and the Li-Mn-O film on silicon substrate.	69
5.2	Raman peaks for a variety of manganese oxide materials.	71

List of Abbreviations

EPR	electron paramagnetic resonance (see ESR)
ESR	electron spin resonance (see EPR)
EuPc ₂	europium bisphthalocyanine
FT-SERS	Fourier transform surface enhanced Raman scattering
FTIR	Fourier transform infrared
γ-MnO ₂	the γ phase of manganese dioxide
GdPc ₂	gadolinium bisphthalocyanine
H ₂ Pc	phthalocyanine or metal-free phthalocyanine
IDE	interdigitated electrode
λ-MnO ₂	the phase of manganese dioxide that results from the complete electrochemical extraction of lithium from LiMn ₂ O ₄
LB	Langmuir-Blodgett, refers to a monolayer on a solid substrate
Li-Mn-O	a lithium-manganese-oxygen film of mixed phase
LiMn ₂ O ₄	the spinel phase of the lithium-manganese-oxygen system
LnPc ₂	bisphthalocyanine of the lanthanide series
LuPc ₂	lutetium bisphthalocyanine
NIR	near infrared
NO ₂	nitrogen dioxide
Pc	phthalocyanine
PCs	phthalocyanines
ppm	parts per million
RF	radio frequency
RRS	resonant Raman scattering
RS	Raman scattering
SERRS	surface enhanced resonant Raman scattering
SERS	surface enhanced Raman scattering
UV	ultra-violet

Chapter 1: Introduction

“What would happen if we could arrange the atoms one by one the way we want them?” Richard Feynman,
December 29, 1959.

The speech presented by Richard Feynman [1] at the annual meeting of the American Physical Society nearly thirty-seven years ago has served as a principal inspiration for researchers involved in much of the work in the exciting and innovative field of nanotechnology [2-4]. Indeed, the term *nanotechnology* provokes images of tiny, interlocking molecular gears and axles diligently assembling products one atom at a time, an image taken directly from Feynman’s essay. However, nanotechnology need not refer only to molecular machines. And while Feynman was certainly the first to construct these images of machines at the nanometer scale, devices have long been manufactured at that scale – in one dimension at least!

1.1 History of Oriented Molecular Monolayer Preparation

It is argued that the preparation of films of monomolecular thickness dates back nearly four thousand years to ancient Babylonia [5], where the first records of the observation of the spreading of oil on water were written in cuneiform. Rayleigh [6] and Pockels [7] can be credited with deducing that such films were of a thickness scale of the order of a few nanometers or less. Rayleigh estimated that films of olive oil of one to two nanometer thickness could be carefully spread onto a water surface. Pockels devised an ingenious trough designed to measure the variation in the surface tension of a soap-contaminated water surface. With this clever trough (a predecessor to what is today known as the Langmuir trough) and working from her kitchen table, Ms. Pockels

could record surface tension versus area isotherms. The first of these diagrams appeared in 1891 [7]. She described her results in a letter to Lord Rayleigh who sent the letter on to *Nature* for publication. Realizing the significance of Pockels work, Rayleigh included a covering letter of recommendation; the editor published Pockels work in full along with Rayleigh's note. It was not until a few years later however, that Rayleigh came to the realization that these films of polar oils were in fact one molecule thick [8].

The trough designed by Pockels formed the basis for the Langmuir trough, named after Irving Langmuir. Langmuir's forte was his uncanny ability to compile several related theories and facts, and to then rework them into one simple and unifying hypothesis [9]. In addition to the improved theory of oriented molecular monolayers, Langmuir continually made improvements to his trough including the development of the Langmuir Filmbalance [9], a device used to directly measure the difference in the forces exerted by a clean water surface and a water surface covered by a molecular film. In honour of the profound contributions he has made to their study, floating monomolecular films at the air-water interface are now termed Langmuir monolayers.

The technique of the transfer of Langmuir monolayers from the liquid subphase to a solid substrate was first detailed by Katherine Blodgett [10]. These monolayer films are called Langmuir-Blodgett films, and they provide a technique for the preparation of oriented molecular films of uniform thickness of a few nanometers or less. The next step towards building a nanometer-thick gas sensor would involve the choice of molecule needed to form the LB monolayers.

1.2 Background of Phthalocyanines

Phthalocyanines (PCs) are intensely coloured synthetic molecules that resemble naturally occurring porphyrins, a sketch of the metal-free phthalocyanine (H_2Pc) is shown in Figure 1.1. The molecule has a planar structure and consists of a highly conjugated network of π -bonds between carbon and nitrogen atoms. The intense colour of these compounds arises from this conjugated π -system, giving strong $\pi - \pi^*$ type

absorptions in the visible. The first phthalocyanine was synthesized by Braun and Tcherniac in 1907 [11]. Since that time, phthalocyanines and their derivatives have played important roles in many applications such as dyes, photoconductors, and in nonlinear optical devices [12-14].

The first Langmuir monolayers of a phthalocyanine were prepared by Roberts *et al.* [15]. The monolayers were prepared from a solution of the

dilithium salt (Li_2Pc), and the limiting area per molecule was determined to be 100 \AA^2 (or 1 nm^2). It was concluded that the molecules were tilted slightly from the plane of the air-water interface. These monolayers however, could not be transferred by the LB technique. It was found that the addition of mesitylene to the solution prior to spreading on the water allowed the formation of transferrable monolayers. The mesitylene was said to *lubricate* the transfer of the mixed monolayer. The limiting area though, was calculated to be 40 \AA^2 (0.4 nm^2). Hence the phthalocyanine molecules were no longer in a slightly tilted orientation but were instead stacked on edge.

Lanthanide bisphthalocyanine complexes were first synthesized by Kirin and Moskalev in 1965 [16]. Since then, these rare earth sandwich compounds have drawn considerable attention, in particular due to their electrochromic properties; the stable green LnPc_2 complex is reduced to a blue form and oxidized to a red compound. Some groups have reported the synthesis and isolation of both blue and green forms [16-18], but the nature of these complexes has been the subject of much debate [19].

The high degree of thermal stability of these complexes has led to considerable work towards the preparation of evaporated films. The phthalocyanine sample can be heated in vacuum without decomposition, and the evaporated molecules condense on

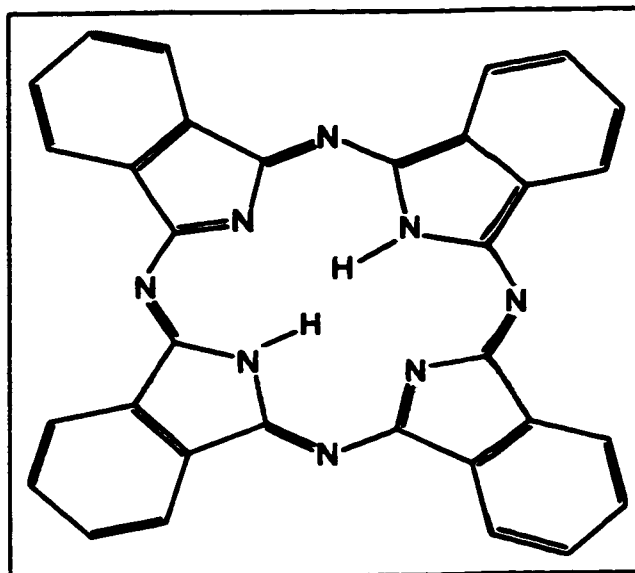


Figure 1.1: A sketch of metal-free phthalocyanine (H_2Pc).

the substrate to give a film constituted of intact LnPc_2 molecules. However, gas sensor devices built by the LB technique [20] have shown improved performance over those prepared from evaporated films [21,22]. This improvement was due in part to the more complete and uniform coverage afforded by the LB technique. The other deposition techniques give films that may have on average a monolayer coverage, but in fact have voids (areas of no coverage) neighbouring molecular aggregates of much greater than monolayer thickness. The voids act to inhibit conduction along the film while the contiguous LB films are not similarly affected.

The focus of microelectronic (or even nanoelectronic) NO_2 gas sensor research and development is therefore directed toward the application of the Langmuir-Blodgett method to form uniform monolayer films of LnPc_2 molecules.

1.3 Introduction to Thin Film Microbatteries

The manufacture of tiny sensors, computers, video displays, or other kinds of microelectronics has been proceeding at a breakneck pace for many years now. As these devices continue to shrink in size, it is becoming increasingly difficult to power them, and in fact, the power source is often external to the device. One of the motivations for reducing the size of these electronics gadgets however, is portability. Having an external source is contrary to the desire that these electronic tools be completely portable. In order to increase the portability of these tiny microelectronic devices, their internal power sources must be equally tiny. While making smaller batteries is a simple task, the total power storage must be sufficiently high to minimize the need for recharging, and consequently, the reduction in battery size must also be accompanied by an increase in power density.

There has been intense activity in the research of rechargeable lithium batteries due to their ability to store more than twice the energy per unit mass as other rechargeable batteries [23-25]. A number of cathode and anode arrangements have been and are being explored. Cathodes based upon LiCoO_2 and LiNiO_2 have shown

considerable progress; the first commercially successful rechargeable lithium battery utilized the LiCoO_2 intercalation complex as the cathode and a graphite based anode material [26]. LiCoO_2 forms a layered system, and so charge-discharge cycling involves the migration of lithium ions from between the cobalt oxide layers to the graphene layers and back again.

Much attention is now focussed on the preparation of thin film rechargeable lithium batteries for microelectronics applications. Additionally, analyses of *pristine* cathode films would help researchers elucidate some of the mechanisms of cathode failure that have plagued these systems. Currently, cathodes are being prepared from mixtures of the pure lithium metal oxide (eg. LiMn_2O_4 , LiCoO_2 , or LiNiO_2) powders and binder materials. By fabricating cathodes that do not require binder material, cell failures due particularly to the cathode material can be more easily traced. Particular interest has been placed on cathodes based upon the LiMn_2O_4 spinel complex [23,27], due to their comparatively low cost as compared to the cobalt and nickel complexes as well as their low toxicity.

Chapter 2: Thin Film Preparation Techniques

A wealth of techniques for the preparation of thin films has been devised since its inception over a century ago. Faraday is credited with the first reported metal film preparation in 1857 when he observed the deposition of a metal film after a wire was exploded by application of high current density [28]. This discovery spawned intense activity into thin film research due to the potential technical value and scientific curiosity in the properties of two dimensional solids.

Now, numerous systems for film deposition are at the disposal of scientists, engineers, and industry alike. The choice of technique is dependent upon the nature of the material(s) to be deposited and the desired properties of the film. Three very different film preparation methods were employed for the work presented in this thesis, namely thermal evaporation, magnetron sputtering, and the Langmuir-Blodgett technique. To understand the motivation for using one approach over another, one must comprehend the phenomena involved. Consequently, a brief overview of each technique is given and all are compared to demonstrate their particular strengths and weaknesses.

2.1 Thermal Evaporation in Vacuum

About thirty years following Faraday's seminal work in thin film deposition, Nahrwold reported the deposition of a thin film by thermal evaporation [29]. This technique failed to catch on, however, until the development of high vacuum systems. Such a high vacuum thermal evaporation system is illustrated in Figure 2.1. The essential components of such a system are a heater for the source material and a stage to hold the film substrate. The heaters can take many different forms, but often boats

made from highly refractory metals such as tungsten, tantalum or molybdenum are utilized. A high current density is passed through a boat containing the sample; the boat is heated, and the sample is thus vaporized. The vapour condenses on the substrate, and a film forms.

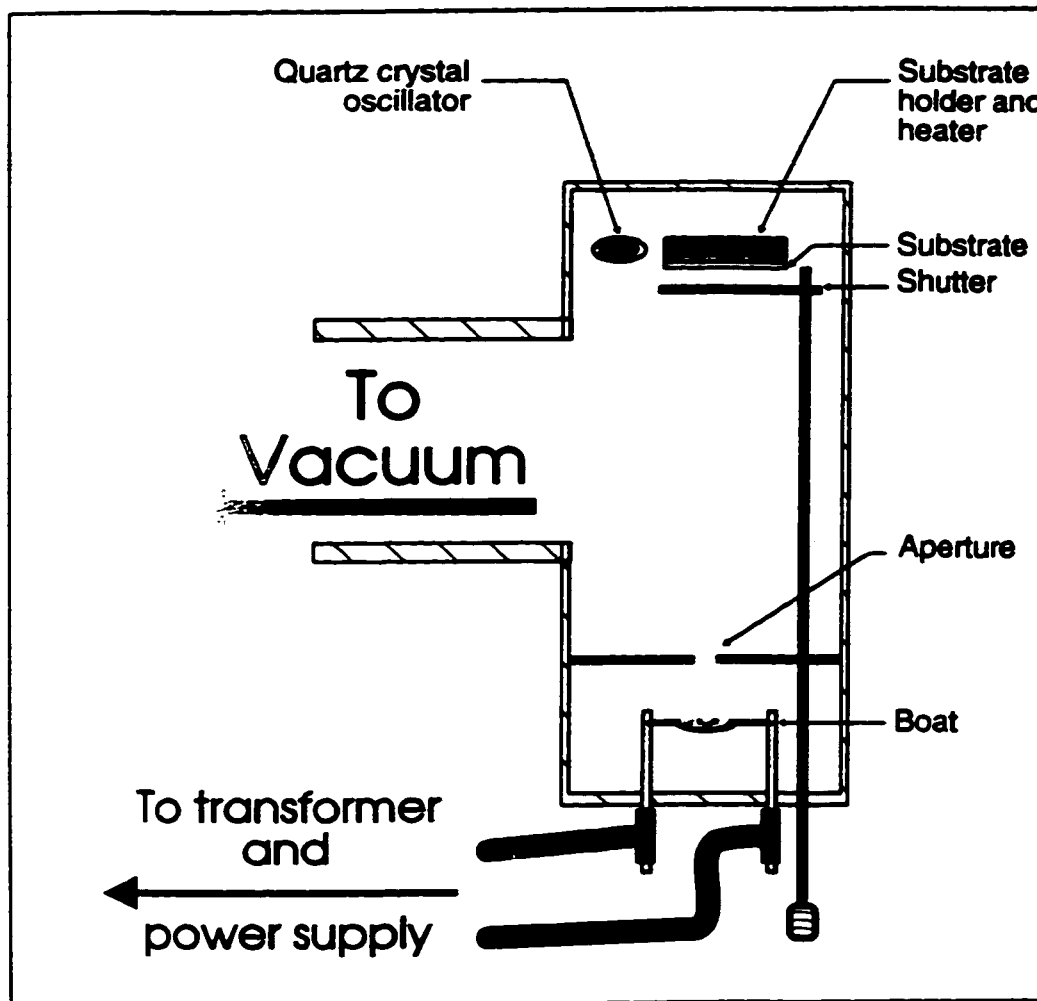


Figure 2.1: A schematic diagram of a thermal evaporation system.

Two evaporators similar to the illustration in Figure 2.1 were used to make metal island films, smooth silver mirrors, and thin organic films. To eliminate cross-contamination problems, one evaporator was dedicated to making metal films while the other was used for the organic thin films. The substrate holders were manufactured from brass and a resistive heater was inserted within the brass in such a way as to ensure good thermal contact between the brass and the heater. The leads from the heater and a

thermocouple that was attached to the brass were passed through a feedthrough out of the vacuum to a controller. The temperature of the substrate could thus be monitored and regulated. The boats were made of tantalum, and a metal plate having a one centimeter hole in the centre was located approximately two centimeters above the boat to act as an aperture to reduce the spray from the sample during heating. The aperture thus serves as a *pseudo* surface source of one centimeter diameter. The substrate was situated approximately 20 cm from the source.

One important aspect of the vacuum evaporation technique is that it is relatively clean. The films were deposited at pressures that made it unlikely that the evaporated atoms or molecules would have the occasion to interact with background gases such as water or oxygen prior to condensing on the substrate. Generally, the pressure in the chamber during deposition was kept below 5×10^{-6} torr ($\sim 7 \times 10^{-4}$ Pa). At such pressures, the mean free path of the atoms and molecules was approximately ten meters. Since the substrate was only about 20 cm away from the source, few collisions occur between the evaporated atoms or molecules and the background gas prior to deposition.

The thermal evaporation technique enables the formation of pure films of thermally stable materials that have comparatively low boiling points. It was an ideal technique for the preparation of thin metal island films of gold and silver for use in surface enhanced Raman scattering experiments. Thin films of materials having very low vapour pressures such as refractory metals like tungsten and platinum or metal oxides cannot be prepared by this method. Compounds that are susceptible to thermal decomposition are likewise poor candidates for the thermal evaporation technique. For these systems alternate approaches are necessary.

2.2 Magnetron Sputtering

Unlike thermal evaporation, the sputter deposition technique does not require high vacuum. Cathode sputtering was thus a popular approach in the early days of film deposition techniques.

The momentum transfer by the collision of gas phase ions with a solid produces a burst of atoms and molecules from the solid surface. Such collisions may be generated by an electrical discharge at low gas pressures between two electrodes as illustrated in Figure 2.2, an illustration of a planar cathode sputtering system. The discharge ionizes some of the gas molecules and the resultant ions accelerate toward the cathode. The kinetic energy carried by the ions (also known as *fast ions* or *fast atoms*) causes the disintegration of the cathode target.

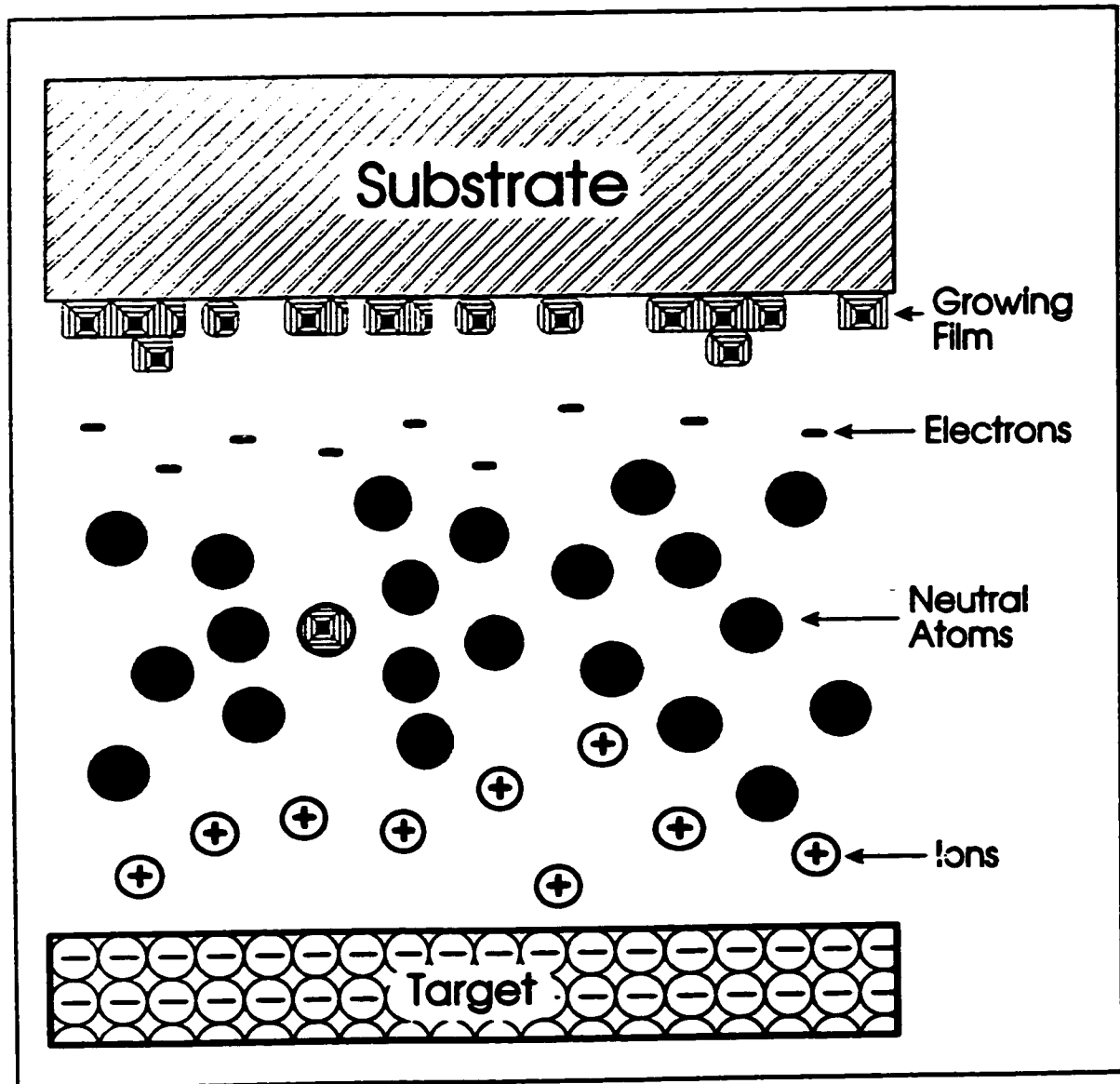


Figure 2.2: An illustration of the planar cathode sputtering technique.

The efficiency of the sputter rate is greatly enhanced by the introduction of a magnetic field situated in such a way that the electrons produced in the discharge become trapped close to the cathode surface. Such a system is illustrated in Figure 2.3. The captured electrons are highly concentrated within the magnetic field, and they begin to follow circular paths inside the trapping field.

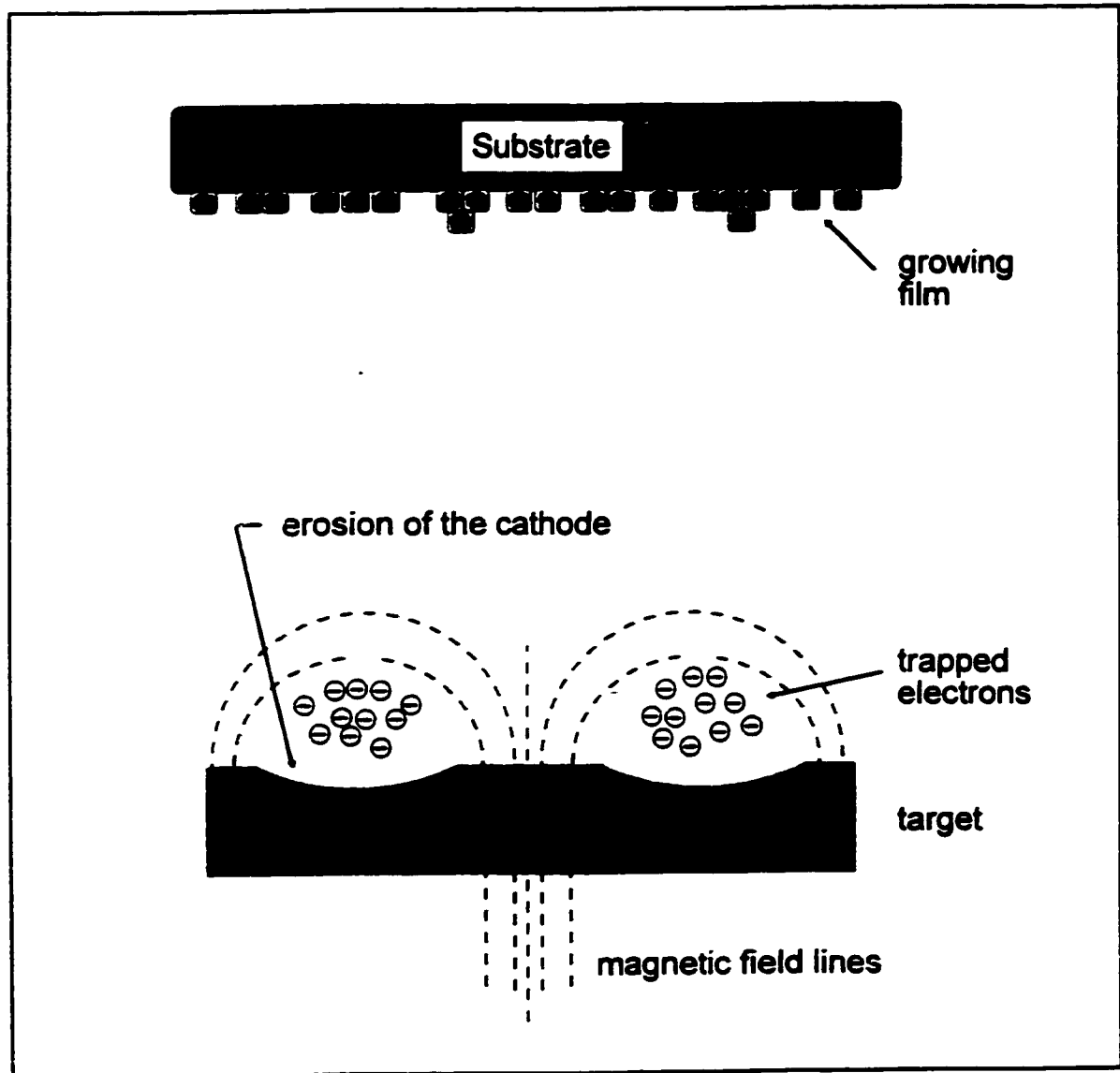


Figure 2.3: An illustration of magnetron sputter deposition.

Gas atoms entering the highly concentrated electron cloud have a much higher probability of becoming ionized than in the discharge without the magnetic field.

Lower pressures are therefore possible while maintaining the sputter process.

During DC sputtering, a charge can build up on the target due to the constant bombardment by positively charged ions. The charging does not pose a problem for conducting materials, but the sputter rate of insulators such as metal oxides drops off rapidly as the growing positive charge on the target begins to repel the bombarding ions. Employment of an alternating current source circumvents this problem, and so the technique of radio frequency (RF) sputtering was developed to deal with insulating or semiconducting target materials. The most commonly used alternating frequency is 13.56 MHz, which lies within the radio frequency region of the electromagnetic spectrum.

A commonly used sputtering gas is argon. There are many advantages to using argon, not the least of which is that it is comparatively inexpensive. It is also chemically inert, a factor that is quite important when the deposition of a pure film is desirable since the operating pressure for sputtering ranges from a few millitorr to a few tens of millitorr. The ejected material from the target will therefore undergo several collisions prior to condensation on the substrate. While the higher operating pressure facilitated the use of the sputtering technique prior to the advent of high vacuum systems, the possible reactions due to gas phase collisions has caused this method to be dubbed a "dirty" technique. However, by utilizing high vacuum technology, the potentially reactive gases such as oxygen or water vapour can be removed in favour of the inert argon gas that is introduced to the evacuated chamber.

Alternatively, should gas phase reactions be desirable, reactive gases could be introduced into the vacuum system by seeding the argon gas flow. By carefully regulating the amount of reactive gas, the stoichiometry of the reaction is controlled. Such a system was used for the deposition of Li-Mn-O films for the use as cathode materials for rechargeable lithium batteries, and is illustrated in Figure 2.4.

The sputter chamber consisted of an ultrahigh vacuum (UHV) chamber pumped by cryopump to provide a base background pressure below 1×10^{-9} torr. In that chamber were three magnetron sputter guns and a quartz crystal to monitor film deposition. Also

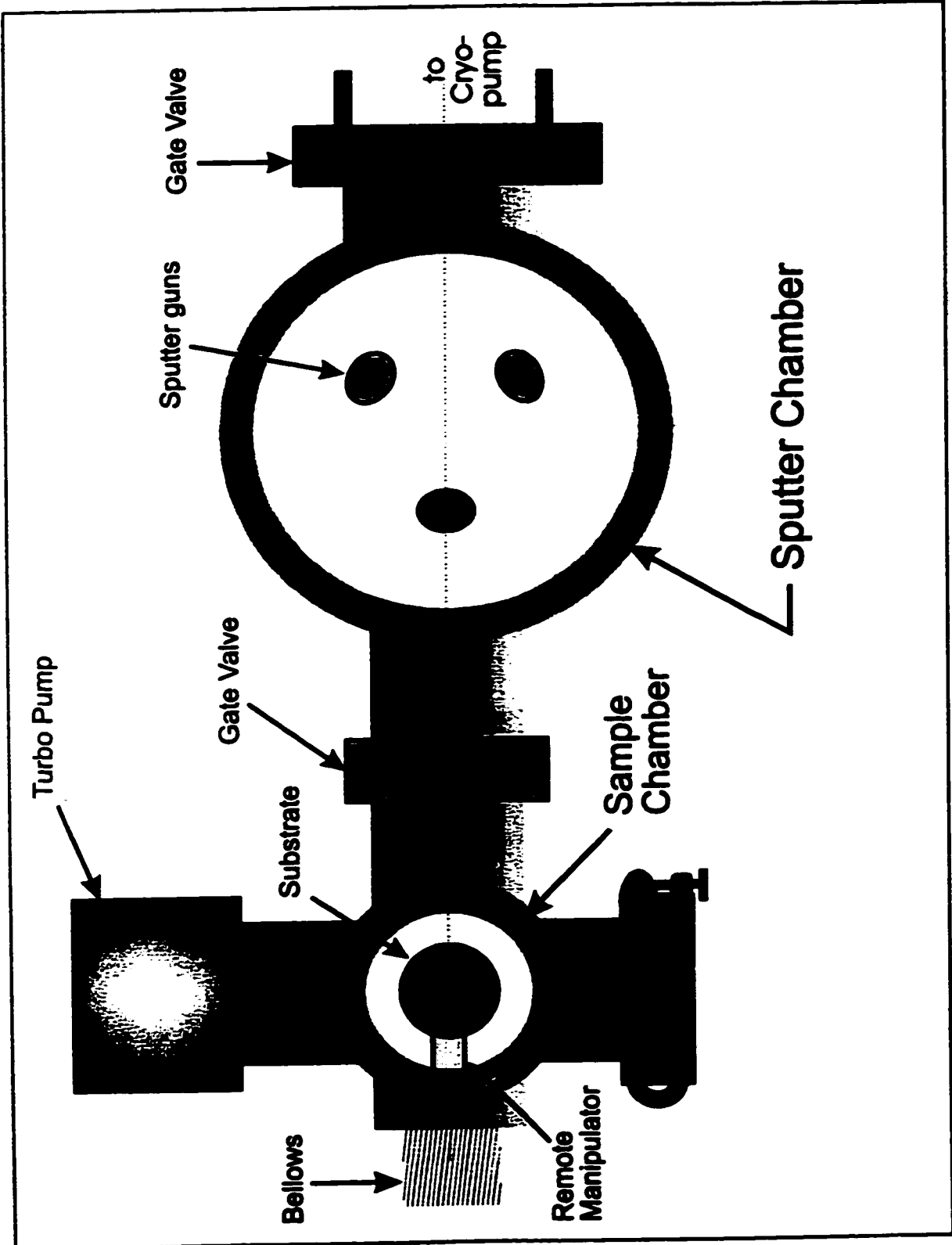


Figure 2.4 An illustration of the UHV magnetron sputter chamber used in the preparation of Li-Mn-O films.

on that chamber was a differentially pumped quadrupole mass spectrometer to monitor the gaseous species in the chamber. The substrates were introduced to the sputter chamber from a separate sample chamber via a remote manipulator. A gate valve separated the high vacuum sample chamber from the UHV sputter chamber. Argon and seed gases flows were controlled by flow controllers and entered the chamber through slow leak valves. A manual gate valve to the cryopump was partially closed in order to diminish the pumping speed of the pump. The operating pressure of 5-10 mtorr could thus be obtained.

This system permits the deposition of various films and not possible by the thermal evaporation technique such as metal oxides. Factors such as substrate temperature during and after the deposition may affect the degree or type of crystallinity of the film. The control of such processes are not in the hands of the scientist however, but instead relies to a large extent on the nature of the films themselves.

2.3 The Langmuir-Blodgett Technique

The first two techniques described here refer to methods that are well suited for the preparation of films up to several microns in thickness. And even if the deposition is halted very shortly after it was begun, the film would not likely display a uniform thickness of say 4 nm over the entire substrate surface. Instead, what one obtains is an ensemble of aggregates of various sizes and perhaps some voids on the substrate where no condensate can be found at all. So, when one speaks of monolayer coverage when referring to films deposited in such fashions, it is most likely an average coverage. Much of the theory to describe the kinetics of adsorption arises from the work of Irving Langmuir [30-32], work for which he earned the 1932 Nobel Prize in Chemistry. Interestingly, a technique that bears his name allows the formation of uniform monomolecular films.

The Langmuir trough consists of a vessel with a clean, hydrophobic coating (Teflon™), a movable barrier, and a fixed barrier. Pure liquid is poured into the trough

such that it is completely full. The fixed barrier acts as a very sensitive balance capable of measuring directly the difference in the surface pressure exerted on one side of the barrier versus the other. Thus, when molecules are placed on the liquid surface on one side of the barrier, the change in the force exerted on that side is detected. This energy per unit area is termed the surface pressure, and is usually denoted by the symbol " π " and has the units of mNm^{-1} . The surface pressure is the two dimensional analogue to pressure.

A variation of the Langmuir Filmbalance uses a device known as the Wilhelmy plate to measure changes in the surface tension of the liquid subphase when molecules are spread upon its surface. The Wilhelmy plate is wetted by the liquid and then remains partially immersed. The downward force exerted on the plate by the surface tension of the water is observed and any changes are related to the change in surface pressure.

Illustrated in Figure 2.5 is a diagram of the preparation of a Langmuir film on a trough known as a Langmuir Filmbalance. In the top frame is shown the trough in the completely expanded mode shortly after the solution has been spread. The solute in this case are represented by amphiphilic molecules having hydrophilic head groups and long hydrophobic tails, and the liquid subphase is water. After the solvent has evaporated, the amphiphilic molecules are free to move about on the water surface in a fashion analogous to the gas phase in three dimensions.

When the movable barrier compresses the film, the molecules begin to interact with each other. The surface pressure begins to increase, and the film enters a liquid-like phase. Further compression (Figure 2.5c) brings the film to the solid-like phase. By this method, a single monomolecular film is prepared. From the data obtained from a π -A isotherm, the surface area per molecule can be determined and the molecular orientation can thus be calculated.

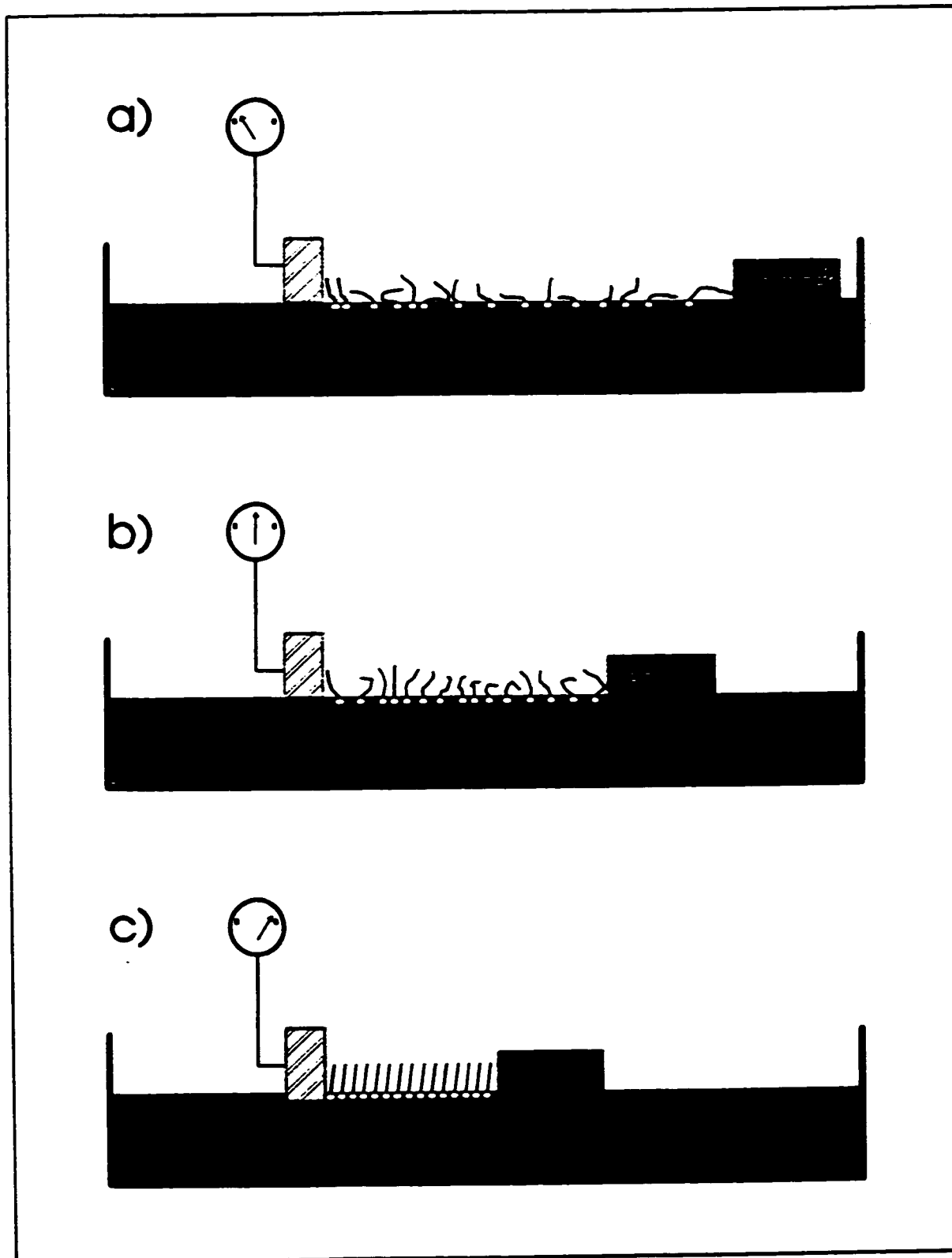


Figure 2.5: An illustration of the Langmuir Filmbalance showing: (a) the expanded phase, (b) the liquid condensed phase, and (c) the solid-like phase.

While Langmuir demonstrated that it was possible to prepare oriented monomolecular films, it was Katherine Blodgett who was the first to transfer a Langmuir monolayer from the liquid surface to a solid substrate. This was performed quite simply by dipping the support into the water, and carefully drawing it out. Such a film is known as a Langmuir-Blodgett (LB) monolayer. To determine the transfer ratio, one can set a feedback loop to cause the movable barrier to move so as to maintain a fixed pressure. As molecules are drawn off of the surface, the barrier must move to restore the pressure of the system. From the distance the barrier travelled and the width of the trough, the total area of the transferred film is calculated. The transfer ratio is defined as the ratio of the area of monolayer removed from the water surface to the area of the solid substrate coated by the monolayer.

Transfer of monolayers to the solid substrate may occur on downward strokes, upward strokes, or both. The designations given for the types of deposition are: X-type for deposition on downward strokes only, Y-type for deposition in both the upward and downward strokes, and Z-type for only the upward stroke.

The Langmuir-Blodgett technique enables the preparation of thin organic films. The films have a uniform thickness that can range from a few nanometers (one monolayer) to a few tenths of a micrometer. And perhaps more important than uniform thickness is the high degree of molecular orientation within the layers. The future of thin molecular solids is in the design of organized thin films for novel devices as well as improvements on existing applications [33]. Such organized films could find use as nonlinear optical devices [34], optical waveguides [35, 36], or protective layers for integrated circuit boards. LB films have also found application as gas sensors [20,37,38]. It is this last application that was pursued in this thesis. In particular, LB films of europium bisphthalocyanine were employed as NO₂ gas sensors.

Chapter 3: Preparation and Characterization of Europium Bisphthalocyanine Thin Films

Phthalocyanines (Pc) are a class of materials that have an extensive list of practical applications. Their extended π -system and molecular symmetry have prompted much attention towards their usefulness as dyes, and their high degree of planarity gives Pc complexes interesting packing characteristics in the solid state due to the weak intermolecular π -cloud interactions. In particular, lanthanide bisphthalocyanine complexes (LnPc_2) have received considerable attention in theoretical [39-41] and spectroscopic [12, 13, 42] investigations.

The study of these complexes in the visible and infrared regions of the spectrum and the fabrication of thin-solid films using the Langmuir-Blodgett (LB) approach [43] have been carried out in our laboratory. The spectroscopy of members of the LnPc_2 series such as YbPc_2 [44], DyPc_2 , HoPc_2 [45], and CePc_2 [46], has been reported. M'Sadak *et. al.* [47] have studied the electrochemical properties of a series of LnPc_2 , including the EuPc_2 complex. Moskalev and Alimova [48] reported the UV-vis absorption spectra of EuPc_2 in DMF and chloronaphthalene solutions with maxima at 468, 603 and 674 nm, and 463, 610 and 677 nm respectively. Synthesis of EuPc_2 has also been described by Sugimoto *et. al.* [49].

This chapter reports the results on the fabrication of LB films of EuPc_2 and the observed vibrational and electronic molecular spectra for the EPR active ($g=2.003$) green EuPc_2 material. The intense absorptions in the visible and the weak near-infrared electronic transitions are given. Infrared and Raman spectra of organized solid films on several substrates were also recorded and discussed. The comparison of normal Raman scattering (RS) and resonant Raman scattering (RRS) spectra is made in addition to a brief discussion and application of the surface enhanced Raman scattering (SERS)

technique. The near infrared Fourier transform SERS (FT-SERS) spectrum of a single LB monolayer on metal island films has been published [50]. Here, the FT-SERS spectrum of a monolayer of EuPc₂ on a gold island film was observed and is compared with the results of conventional SERS using visible laser lines on silver island films.

3.1 Experimental

The EuPc₂ material was provided by Dr L.G. Tomilova from the Intermediates and Dyes Institute in Moscow, Russia. The compound was purified first by sublimation to remove some low molecular weight starting materials (phthalonitrile) and by-products (phthalic anhydride and phthalimide). The residue was then further purified by column chromatography to separate other by-products such as H₂Pc, the mono-phthalocyanine europium

complex, and trace amounts of the blue form of EuPc₂. Ultimately, a sample of the green form of EuPc₂ was isolated and used for this work. An illustration of the structure of the EuPc₂ complex showing the sandwich-like structure is given in Figure 3.1. Note that the two macrocycle rings are in a staggered orientation with respect to each other.

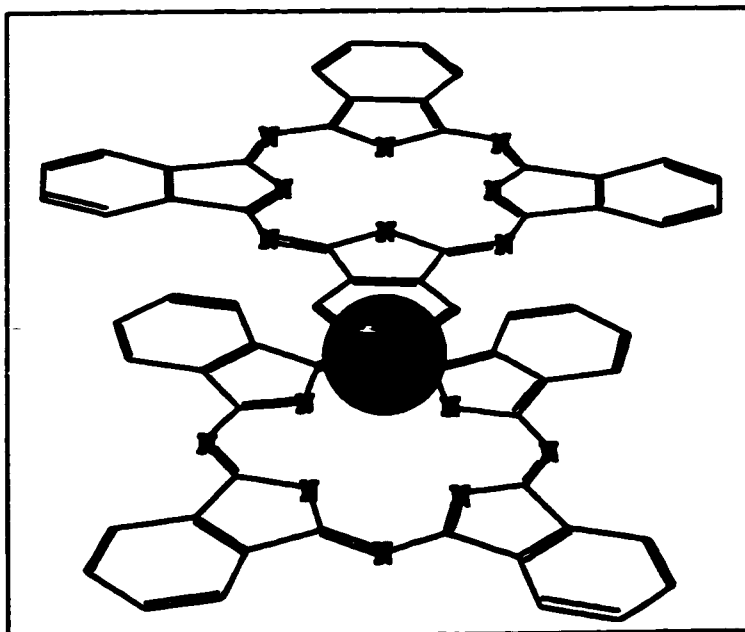


Figure 3.1: An illustration of the europium bisphthalocyanine molecule.

The electronic transitions of EuPc₂ in solution and as LBs on glass were recorded by a Perkin-Elmer Lambda 9 UV-VIS-NIR dual beam spectrometer interfaced to a Perkin-Elmer PE 7700 series computer. FT-Raman scattering spectra were recorded using a Bomem Ramspec 150 spectrophotometer, equipped with a Nd:YAG

laser emitting at 1064.1 nm and an InGaAs detector. An optical filter was used to remove all light within 200 cm⁻¹ of the laser line collected in a back-scattering geometry. All other Raman spectra were recorded using a 90° scattering geometry with a Spex 1403 double monochromator. The light source used for the RRS experiments was a Spectra Physics Model 2020 Kr⁺ laser emitting at 647.1 nm. The blue (488 nm) and green (514.5 nm) laser lines emitted from a Spectra Physics Series 2000 Ar⁺ laser were also used to produce inelastic scattering.

Gold and silver island films for SERS experiments were prepared by vacuum evaporation onto glass slides (Corning 7059 glass) held at 200 °C. The rates of deposition were monitored by an XTC Inficon crystal oscillator and were held constant at approximately 0.5 Å s⁻¹. The gold island films were grown to a thickness of 20 nm for the FT-SERS experiments while 6 nm thick silver island films were grown for the SERS experiments where visible laser lines were used.

Two different Langmuir troughs were used. A KSV 5000 Langmuir trough was used to record isotherms and to transfer Langmuir monolayers. This trough monitors the film pressure directly by the Wilhelmy plate method; the electrobalance used was calibrated daily. The other trough was a Lauda Langmuir Filmbalance equipped with a Lauda Filmlift F1-1 electronically controlled dipping device for the transfer of monolayer films onto solid substrates (Langmuir-Blodgett films). In both troughs, the subphase used was pure water obtained from a Milli-Q filter (resistivity 18.2 MΩ cm) and the temperature of the subphase was controlled with a Neslab TRE-110 circulating bath with temperature sensor. All Langmuir-Blodgett films were prepared from 5x10⁻⁵ mol L⁻¹ chloroform (Merck, 99%) solutions. A surface pressure of 20 mN m⁻¹ was maintained during film transfer, and the subphase temperature was held at 15 °C. Glass slide substrates were cleaned in chromic acid solutions and then rinsed thrice with distilled water followed by a Milli-Q water rinse. The ZnS substrates were treated by ultrasonic bath first in toluene and then in chloroform solvents.

A Bruker FTIR Model 98 (now known as the Model IFS 113v) spectrometer operating under vacuum at room temperature was used to record infrared spectra of KBr

pellets and LB films on ZnS using transmission geometry. The background and instrument response was taken into account by calculating the ratio of the raw sample spectrum versus the reference spectrum to give the sample spectrum in transmittance units. Polarization experiments were performed using a model PWG-U1R polarizing crystal from Harrick industries. All spectral files were imported into the SpectraCalc software package (Galactic Industries Corp.) for data manipulation.

3.2 Langmuir-Blodgett Film Preparation

The formation of a floating or Langmuir monolayer on the water surface is monitored by recording the surface pressure versus area (π -A) isotherm. The π -A isotherm at 15 °C for EuPc₂ spread from a chloroform solution that was recorded using the Wilhelmy plate technique (KSV 5000) is shown in Figure 3.2. This isotherm shows the phase transition from the gas phase to the liquid condensed phase with an ill defined intermediate liquid expanded phase. The limiting area determined by extrapolation from the linear, solid-phase like portion of the isotherm back to zero surface pressure was 1.0 nm² molecule⁻¹. If these molecules were oriented exactly edge-on, then an area closer to 0.7 nm² molecule⁻¹ would have been expected, while a flat-on orientation

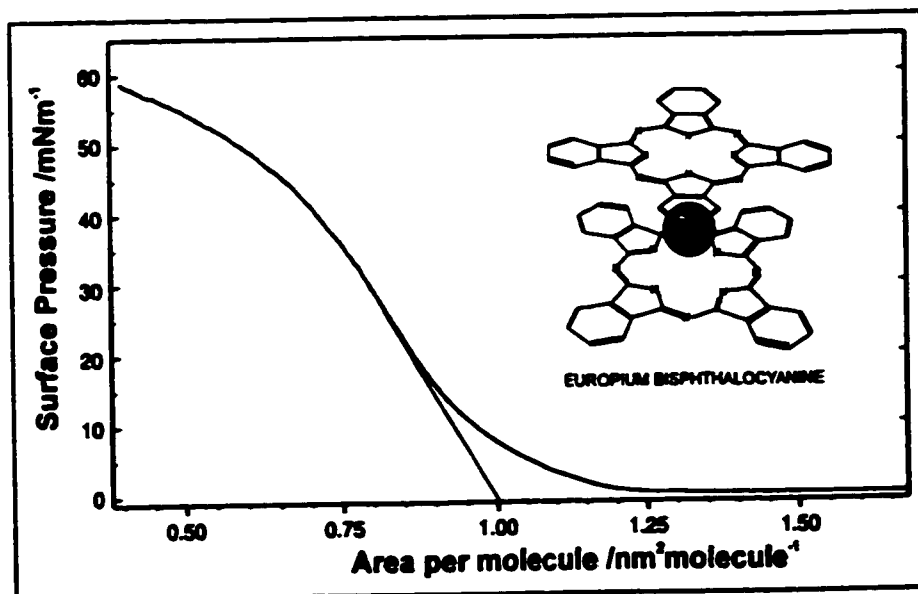


Figure 3.2: The π -A isotherm of EuPc₂ at 15 °C.

would have produced a limiting area closer to $1.5 \text{ nm}^2 \text{ molecule}^{-1}$, the area of a single Pc ring. This value for the limiting area indicates the molecules of EuPc₂ order themselves with a tilted orientation of the planar ring with respect to the subphase.

The LB films were made by transferring the floating layer at a constant surface pressure of 20 mN m^{-1} and a subphase temperature of $15 \text{ }^\circ\text{C}$. This pressure was chosen because it is within the solid-phase or liquid condensed phase of the monolayer. Several different temperatures were attempted but the transfer ratio for Z-deposition proved optimal at this temperature and pressure; films whose transfer ratios are lower than 0.9 were discarded and the experiment was repeated..

3.3 UV-Visible and Near-Infrared Absorption Spectra

One of the important uses for phthalocyanine complexes is as a dye. The very intense colour characteristic of this class of molecules arises from the extensive conjugated π -system. Numerous theoretical studies have attempted to characterize these systems to varying degrees of success [39, 40]. The complexity of the phthalocyanine systems and the comparative strengths and weaknesses of the different theoretical models used have made it prohibitively difficult to resolve the details of the electronic levels of LnPc₂ molecules. A composite of the energy level predictions from Orti *et. al.* [39] and Kaizu *et. al.* [40] is illustrated in Figure 3.3. This diagram

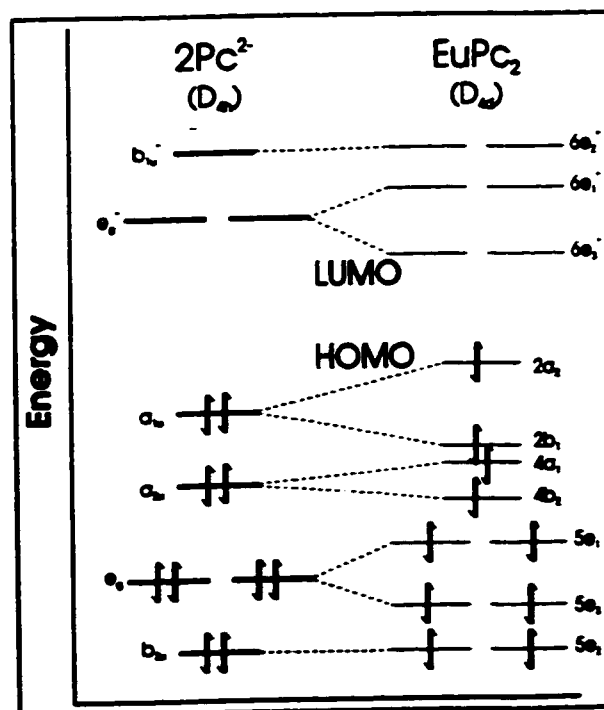


Figure 3.3: The energy level diagrams for two Pc²⁻ ligands (left) having D_{4h} point group and the orbital levels for the EuPc₂ sandwich molecule (right) having D_{4d} symmetry.

demonstrates how the energy levels of the hypothetical Pc^{2-} dianion (on the left) were affected by the formation of the D_{4d} EuPc_2 complex. One very important facet of the energy level diagram of the lanthanide complex is the unpaired electron in the HOMO. Transitions from lower levels to this half-filled orbital cause transitions that are otherwise absent from the phthalocyanine spectrum.

The literature assignments of level labels describing these transitions appear somewhat ambiguous. The interpretations can

generally be grouped into two basic strategies. Some groups [51-53] have chosen to describe the energy levels of each of the two Pc rings separately. Thus, the observed spectrum is described by a superposition of the spectrum of the dianion ligand, the spectrum from the radical anion, and the intramolecular charge transfer band. The other method of level assignment involves the consideration of both ligands within a single molecule [39, 40, 54]. The latter convention was used in Figure 3.4 where the electronic transitions illustrated involving the half-filled HOMO were depicted. These transitions, and more particularly the levels involved in these transitions will be discussed further in the context of the observed resonance Raman spectra.

The UV-VIS-NIR absorption spectra of EuPc_2 are shown in Figure 3.5. The chloroform solution spectrum shows the strong absorptions from the B- and Q-bands typical of the phthalocyanine macrocycle at 322 and 672 nm respectively. By the symmetry orbital assignments for the Pc^{2-} in Figure 3.3, the Q-band represents the $a_{1u} - e_g^*$ phthalocyanine transition while the B-band corresponds to the $b_{2u} - e_g^*$

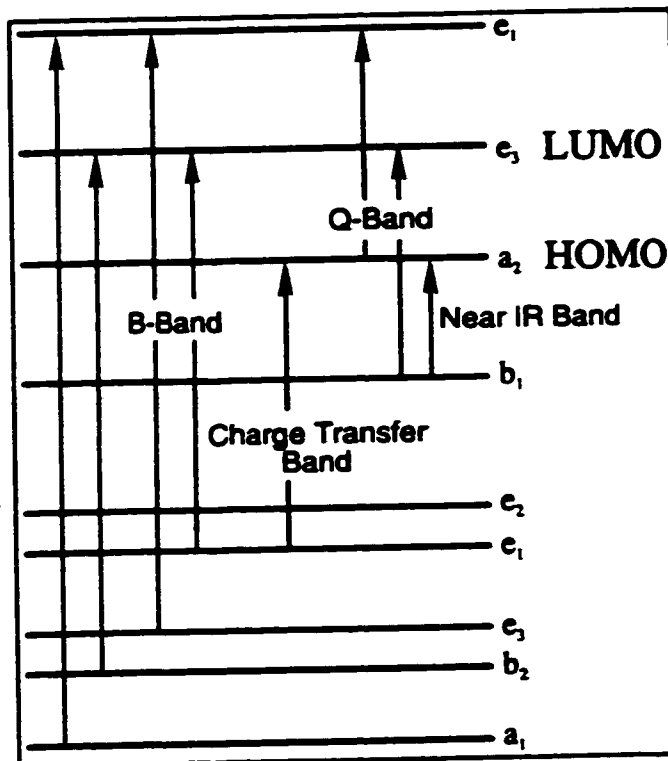


Figure 3.4: The characteristic electronic transitions of EuPc_2 .

transition. Also characteristic of the phthalocyanine dianion are some vibronic transitions to the blue of the Q-band at 603 nm as well as the N-band at 278 nm.

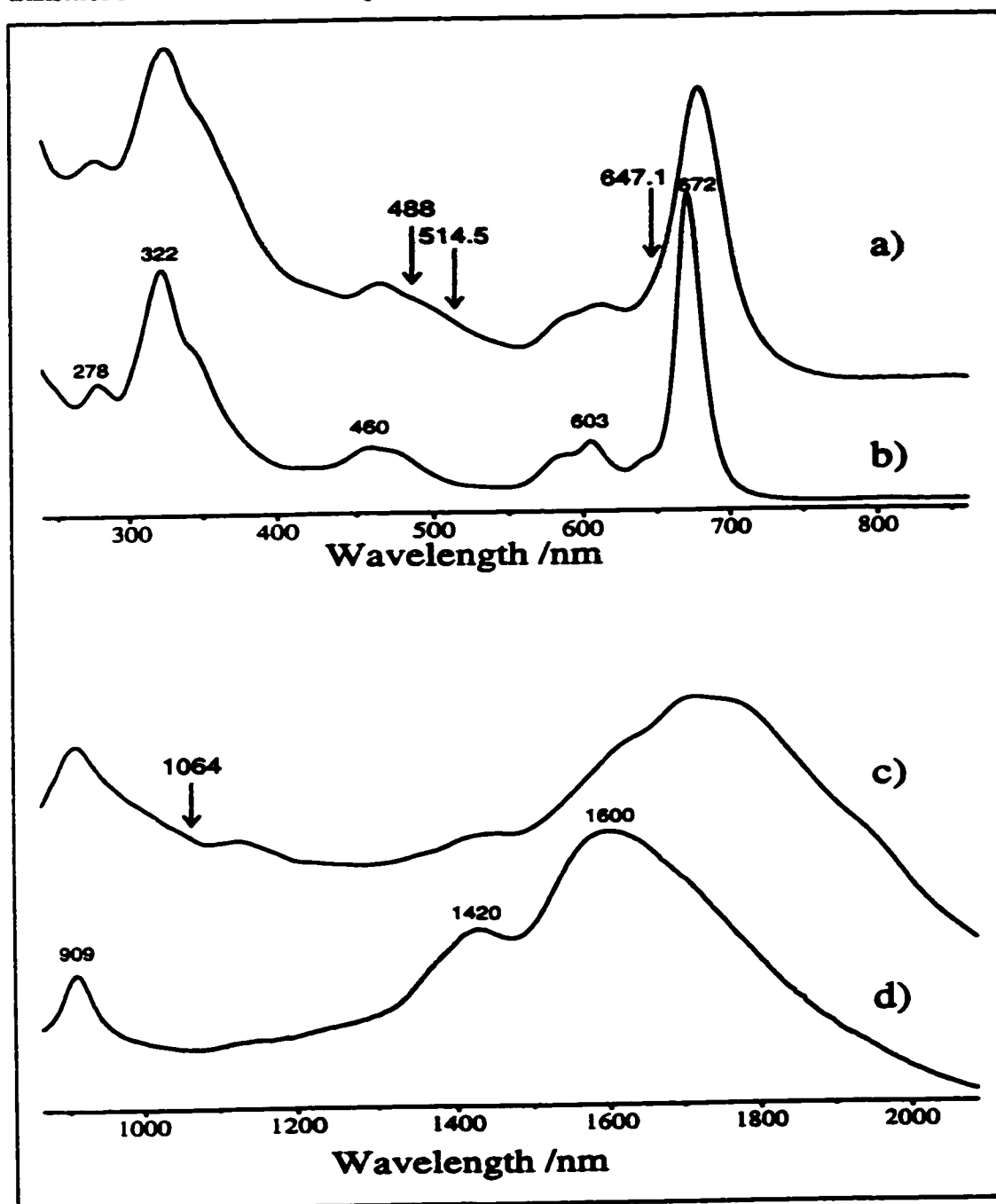


Figure 3.5: The UV-visible spectra of EuPc₂ as: (a) an LB film on glass, and (b) in chloroform solution; and the near-IR spectra: (c) of an LB film on glass, and (d) in chloroform solution.

Atypical of the phthalocyanine dianion, but typical of the radical anion [51], are the bands found at 460 nm and the bands found in the near-IR region. The bands at 460 nm and at 909 nm represent excitations of the radical anion. For instance, the 460 nm transition is analogous to the $4e_g(\pi) \rightarrow 2a_{1u}(\pi)$ and $5e_g(\pi) \rightarrow 2a_{1u}(\pi)$ of LiPc [39, 51]. The transitions centred at 1420 and 1600 nm have been assigned to the intramolecular charge transfer band. This is illustrated in Figure 3.4 as the transition from the second HOMO to the half-filled HOMO.

3.4 Infrared Spectra

Although EuPc₂ has a large number of normal modes, the molecular symmetry greatly simplifies the analysis of the infrared spectrum. While a D_{4d} point group has often been suggested as an appropriate symmetry for bisphthalocyanine lanthanides, the distortion of one of the Pc rings suggests that a C_{4v} point group would more accurately describe the system [42]. This distortion was observed directly in x-ray crystallographic studies of LuPc₂ [55] and NdPc₂ [56] and was attributed to the existence of an unpaired electron on the distorted ring.

Assuming the C_{4v} symmetry, the irreducible representation for the normal modes is given by

$$\Gamma = \underline{44a_1} + 39a_2 + 42b_1 + 42b_2 + \underline{83e}. \quad 3.1$$

The underlined representations are IR active while all are Raman active with the exception of the a_2 modes.

The planarity of the Pc rings of the molecule permits simplification of band assignments to those bands which are in-plane or out-of-plane. Once ordered monolayers of a compound are prepared using the Langmuir-Blodgett (LB) technique, a measure of the orientation is of significant importance in order to understand the

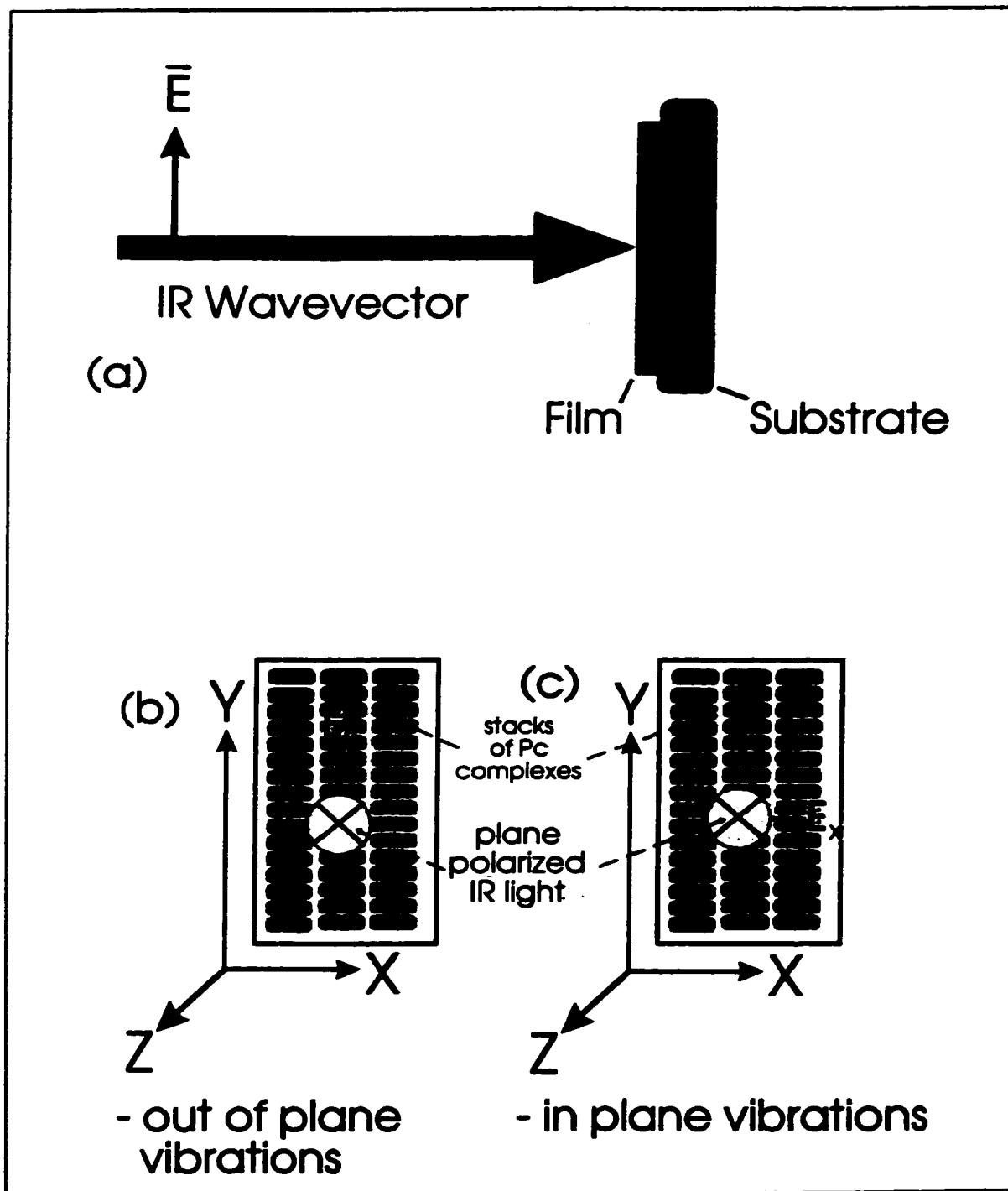


Figure 3.6: The thin film transmission infrared experiment showing the effects of (a) the molecular orientation with respect to the substrate, and (b, c) film anisotropy using plane polarized light.

molecular packing and growth in two-dimensional structures. When the infrared light impinges onto the sample with a wave vector normal to the sample as shown in

Figure 3.6(a), then only those modes resulting in dipole changes parallel to the substrate will be seen. Similarly, polarization experiments would determine the degree of anisotropy cause by the packing of the molecules as demonstrated in Figure 3.6(b, c). In the polarization experiment shown in Figure 3.6(b), only the out-of-plane vibrations would be seen. Conversely, the in-plane vibrations would be seen for the experiment shown in Figure 3.6(c).

Illustrated in Figure 3.7 are the infrared spectra of the bulk sample dispersed in KBr and six LB monolayers on ZnS (the poor throughput of ZnS at frequencies lower than 720 cm^{-1} accounts for the sharp cut-off). The frequencies and band assignments for the FTIR spectra of EuPc_2 were listed in Table 3.1. Even though the low energy

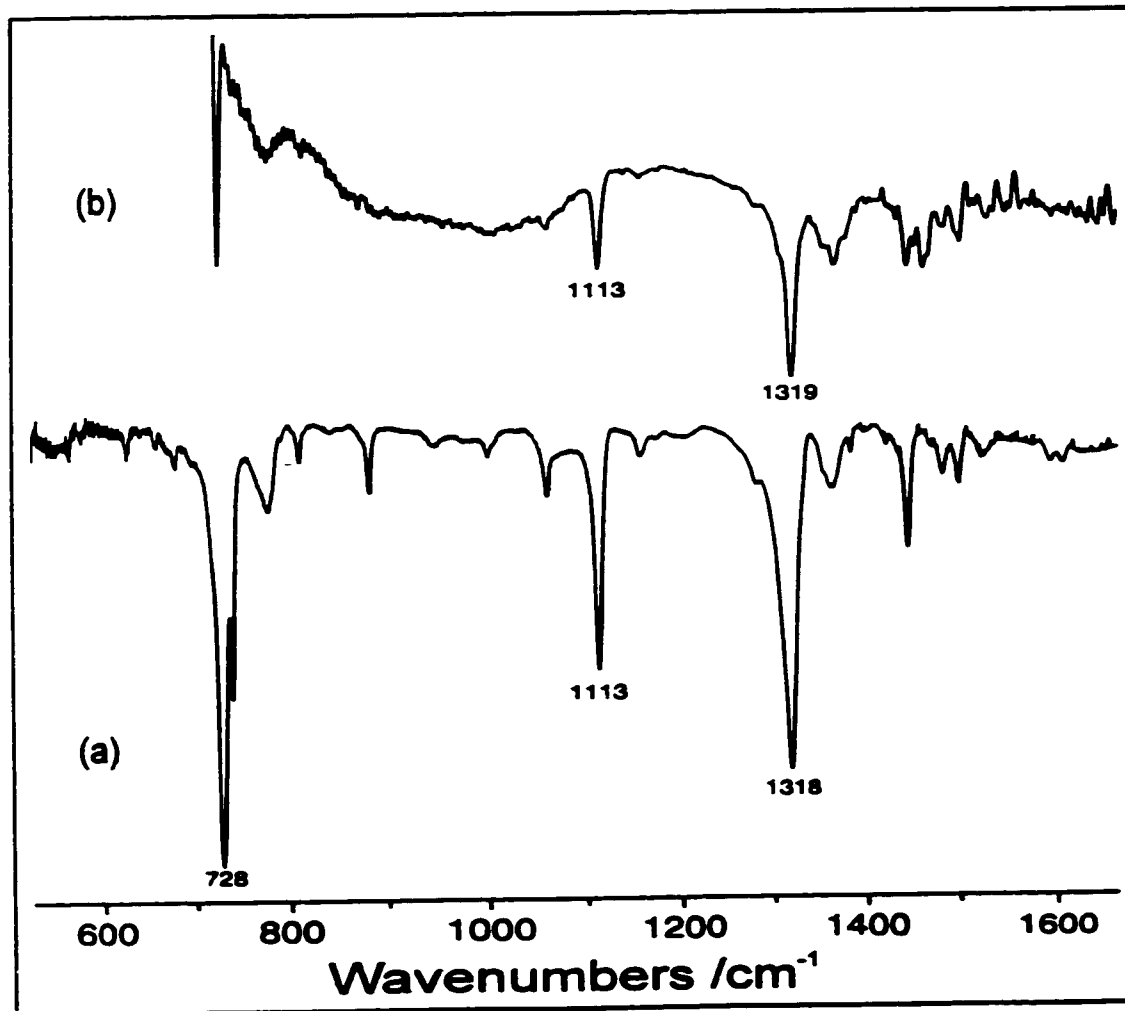


Figure 3.7: The FTIR spectra of EuPc_2 : (a) powder dispersed in KBr, and (b) six LB monolayers on ZnS.

vibrations in the monolayers spectrum were not observed, the window provided by the ZnS substrate may be sufficient to prove the predominant orientation of the molecules on the substrate. The strong bands observed in the FTIR spectrum of LBs were assigned to vibrations having *e* symmetry [44]. Conversely, the 741 cm⁻¹ band (also observed in

Table 3.1: Frequencies and band assignments of the FTIR spectra of EuPc₂.

FTIR of EuPc ₂ in KBr pellet (cm ⁻¹)	FTIR of EuPc ₂ , six LBs on ZnS (cm ⁻¹)	Assignments
1606 w ¹		C=C str benzene v _g
1594 w		C=C str benzene v _g
1524 w	1524 vw	C=N Aza stretch
1500 m	1501 w	pyrrole stretch
1483 w		C=C benzene str v _{10g}
1446 m	1446 w	isoindole str e
1422 vw		isoindole str a _g
1401 vw		isoindole str a _g
1384 w		isoindole str
1364 b	1366 m	isoindole str
1318 s	1319 s	C-C-C str v ₁₄
1281 sh	1281 vw	C-H in-plane deformation
1156 w	1156 vw	C-H bend
1113 s	1113 m	C-H bend e
1060 m	1060 w	C-H bend e
1000 w		C-H bend a _g
945 vw		C-C-C bend v ₁₂
882 m		e
	872 vw	
841 vw		C-H out-of-plane bend
811 w	813 w	e
778 b	777 b	benzene breathing a _g , v _g
740 s	741 vw	C-H wag a _g
729 vs	724 s	C-H wag e
678 w		macrocycle breathing a _g
625 vw		e
562 vw		C-C-C in-plane bend v _{10g}
497 w		

¹ The intensities of the vibrations are given as: vs - very strong; s - strong; br - broad; m - medium; w - weak; and vw - very weak.

the Raman spectrum), probably a a_1 vibration, was quite strong in the bulk spectrum, but barely comes out of the noise in the spectrum of LBs. Therefore, the FTIR spectra indicate that the molecules were oriented such that the plane of the Pc rings were nearly co-planar to the surface, and at the same time, there was no evidence of lateral anisotropy. Polarization FTIR experiments revealed no differences in the spectra of the LB film when the infrared radiation was polarized parallel or perpendicular to the dipping direction, i.e., there was no observed anisotropy.

3.5 Raman and Resonance Raman

The arrows shown in Figure 3.5 illustrate the wavelengths of the laser lines that were used to excite Raman scattering. The coherent resonance Raman scattering (RRS) process occurs when an exciting laser line is close to or in resonance with an allowed electronic transition. Scanning the excitation frequency from off resonance to on resonance results in sharp changes in intensity and other spectral properties. The intensity changes are clearly seen in Figure 3.8 where the Raman spectra recorded from three different laser lines are illustrated. The frequencies and assignments of the observed fundamentals are given in Table 3.2. A general theoretical treatment is applicable independent of incident radiation. The general vibronic representation of the Raman intensities gives each polarizability tensor component as a sum of the three Albrecht terms [57]:

$$\alpha_{\rho\sigma,ij} = A+B+C \quad 3.2$$

where A is also referred to as Franck-Condon scattering and B is known as the Herzberg-Teller term. Contributions from the C term are quite small and so will not be considered in any further discussions. For large molecular systems, such as phthalocyanines, the most important contribution comes from the B term which takes

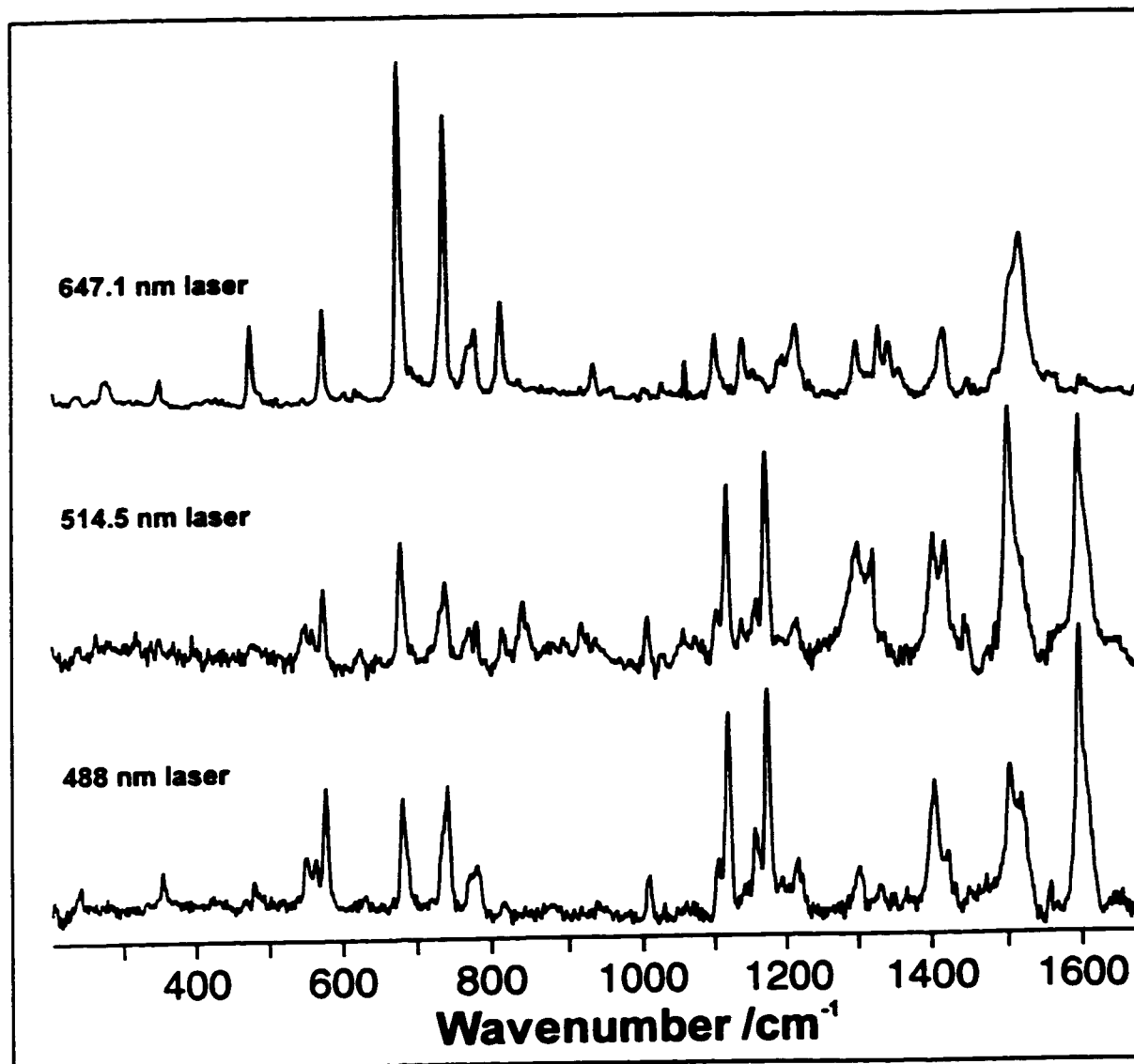


Figure 3.8: The Raman spectra of EuPc_2 dispersed in KBr. The laser lines used to obtain the spectra are indicated about each spectrum.

into account the coupling of electronic states by the coordinate operator [58]. This is due to the fact that for large Pc molecules the excited and the ground state potential energy surfaces are very similar. Consequently, the spectra shown in Figure 3.8 do not display harmonic progressions, and a uniform enhancement of several fundamental vibrational frequencies is observed. The symmetry of the observed fundamentals is given by the direct product of the symmetries of the electronic states. For Pc or Pc_2 molecules the main two electronic states are $E_u (D_{4h})$ or $E (C_{4v})$ supplying

$A_{1g}+A_{2g}+B_{1g}+B_{2g}$ or $A_1+A_2+B_1+B_2$ symmetries for the coordinate operator, and a general enhancement of fundamentals belonging to all these symmetry types is expected.

Table 3.2: Raman spectral frequencies (in cm⁻¹) and band assignments of EuPc₂.

RS from 488 nm laser line	RS from 514.5 nm laser line	RRS from 647.1 nm laser line	FT-SERS (1 LB) on 20 nm Au	Assignments
1604 sh				C=C str benzene ν_{10a}
1595 s	1596 s	1598 vw	1590 vw	C=C str benzene ν_{10a}
1556 vw	1556 vw	1556 vw	1553 w	C=N aza group
1518 m	1520 sh	1519 m	1518 m	pyrrole stretch
1501 m	1502 s	1506 sh	1506 m	pyrrole stretch
	1484 vw	1486 vw	1484 w	C=C benzene str ν_{10a}
1421 w	1419 m	1419 w	1413 w	isoindole str a_1
1403 m	1404 m		1403 w	isoindole str a_1
		1360 vw	1364 w	isoindole str e
		1346 w	1346 w	
1330 vw	1326 m	1332 w	1331 m	C-C-C pyrrole str a_1
1301 w	1302 m	1301 w	1303 w	C-H in-plane deformation
1216 w	1217 w	1216 w	1218 w	C-H in-plane deformation
1173 s	1173 s	1170 vw	1174 w	a_1
1157 m	1161 w	1158 vw	1160 w	C-H bend
		1143 w	1146 w	pyrrole a_1
1118 s	1118 s		1118 w	C-H bend e
1104 w	1104 w	1104 w	1104 w	C-H bend
	1072 vw		1071 w	C-H bend e
	1058 vw	1062 w	1058 w	C-H bend e
1009 w	1008 w	1006 vw	1007 vw	C-H bend a_1
		937 w	936 vw	
	842 m	839 vw	843 vw	C-H out-of-plane ν_{10}
816 vw	816 w	816 m	817 w	C-C-C bend ν_{12}
780 w	782 w	782 w	780 s	benzene breathing a_1, ν_1
	773 w	774 w		
741 m	740 m	742 s	741 m	C-H wag a_1
	732 sh		734 s	C-C-C puckering ν_4
679 m	679 m	679 s	679 m	macrocycle breathing a_1
576 m	576 m	577 m	576 w	benzene radial
563 w	561 w		566 vw	C-C-C in-plane bend ν_{10a}
549 w	552 w		552 vw	C-C-C in-plane bend ν_{10a}
479 vw	481 b	478 m	481 w	pyrrole ring def.
354 w		354 w		
		279 w	277 vw	
241 vw		239 vw	240 vw	metal-N

The krypton ion laser emitting at 647.1 nm used as the incident light source for Raman experiments on phthalocyanines gives very significant enhanced signal due to resonance with the strong Q-band transition. The most intense band in the Raman spectrum of EuPc₂ occurs at 679 cm⁻¹, and mainly low frequency vibrations are enhanced as can be seen in Figure 3.8. This band has been assigned to the macrocycle breathing mode. Indirectly, the observed spectrum seems to support the assignment of the aforementioned transition, since the orbitals in the ground state that are involved with this transition have greatest contribution from AOs of the macrocycle.

Contrary to the Raman experiments using the 647.1 nm laser line, the 488 and 514.5 nm lines of the Ar⁺ laser give rise to quite different Raman spectra (fundamentals of higher frequency are enhanced) due to the fact that entirely different regions of the absorption profile were probed. More specifically, although these laser lines are near resonant to electronic transitions of EuPc₂, the electronic configurations involved in these transitions were quite different from those involved with the Q-band transition.

The transition around 460 nm predominantly consists of a transition similar to the $e_g - a_{1u}$ transition of LiPc [39], however, there are in fact many transitions involving the *hole* in the valence orbital that fall into this region [39, 55]. Hence, the spectra of the Raman scattered radiation from the blue line shares a number of common features with that resulting from the green line due to the probing of common excited states. Some differences, however, were observed, indicating that the laser lines were also probing slightly different vibronic coupling. A number of bands appear similarly enhanced in both the blue and the green laser line spectra, all of these bands invariably involved modes that have been assigned to benzene vibrations. Thus, while the red line probed the inner macrocycle ring of the phthalocyanine ligands, the blue and green lasers gave Raman spectra that emphasize the modes of the peripheral benzene rings. Some important trends were seen which could give an insight into the AOs which contribute to the transitions at 514.5 nm and 488 nm. For clarity, the bands showing the greatest similarity between the two spectra were tabulated in Table 3.3. These bands all seem to share similar relative intensities with respect to each other, an indication that a

common vibronic coupling has been probed.

Table 3.3: List of the bands showing similar relative intensities under green and blue argon ion laser line excitations (in cm⁻¹).

RS of EuPc ₂ , 488 nm laser line		RS of EuPc ₂ , 514.5 nm laser line		Assignments
1595	s	1596	s	C=C str benzene ν_1
1403	m	1404	m	isoindole str A_1
1173	s	1173	s	A_1
1118	s	1118	s	C-H bend E
1104	w	1104	w	C-H bend
1009	w	1008	w	C-H bend A_1
780	w	782	w	benzene breathing A_1
563	w	561	w	C-C-C in-plane bend
549	w	552	w	C-C-C in-plane bend

Important spectral differences are worth noting. The differences generally involved bands associated with the pyrrole ring. For example, the spectrum from the green line showed a much greater intensity for the band at 1502 cm⁻¹ than was observed in the blue line spectrum. This band corresponds to the C=C stretching vibration of pyrrole. Other bands that were preferentially enhanced in the green laser spectrum were found at 1420 cm⁻¹ and at 1326 cm⁻¹. These bands too were assigned to pyrrole normal modes. Notably, the band at 1302 cm⁻¹ has been assigned to a C-H in-plane deformation and a C-H out-of-plane bend was observed at 842 cm⁻¹. Both of these bands were greatly enhanced for the green laser line experiment.

A vital tool to aid in the unambiguous assignment of the enhanced versus the normal Raman scattering is the near-IR Raman technique. In practice, FT-Raman has been extremely useful for recording the spontaneous Raman spectrum of most compounds because the 1064 nm Nd:YAG laser source was generally quite far from resonance, and the signal averaging advantage afforded by the Fourier transform technique brings out even very weak signals. Unfortunately, attempts to record FT-Raman spectra of the bulk EuPc₂ were unsuccessful due to heating of the sample. Consequently, FT-SERS, a technique which has been used successfully to record spectra of LB monolayers [50] was used.

3.6 Surface Enhanced Raman Scattering

The impingement of photons onto metal particles induces electromagnetic fields that facilitate the enhancement of the very weak Raman signal typical of thin films. The enhancement arises from the dielectric properties of the metal and the particle shape such that the polarization is given by:

$$P = \frac{1}{4\pi} \frac{(\epsilon - 1)}{1 + (\epsilon - 1)A} E_0 \quad 3.3$$

where ϵ is the complex dielectric function of the metal, A is a shape factor for the particles, and E_0 is the electric field from the laser light. Assuming the particles are spherical, the shape factor becomes 1/3 and equation 3.3 becomes

$$P = \frac{3}{4\pi} \frac{\epsilon - 1}{\epsilon + 2} E_0 \quad 3.4$$

Clearly the polarization approaches infinity as the real part of the dielectric function approaches minus two. Since the dielectric has a wavelength dependence, the choice of metal and careful control of the particle size are important factors of consideration for the surface enhanced spectroscopy in general and surface enhanced Raman scattering (SERS) experiments in particular. The metal particle films must be *tuned* to the desired frequency of the electromagnetic radiation.

The choice of metal and film thickness that would give optimal enhancement for a given frequency of radiation was predicted using tabulated values of the dielectric functions [59]. Ultimately, the choice of metal and film deposition techniques were determined empirically from the determination of the surface plasmon frequencies by recording the transmission UV-visible-near infrared spectra of the metal island films as

deposited onto glass slides.

Examples of such spectra are shown in Figure 3.9 and Figure 3.10. The traces in Figure 3.9 shown the spectrum of a 6 nm silver island film on glass that gives high plasmon intensity in the region of the 488 nm and 514.5 nm lines of the Ar⁺ laser and the spectrum of a 4 nm gold island film that gives high enhancement for the 647.1 nm Kr⁺ laser line. Larger gold particles and hence a thicker film was necessary for the FT-SERS experiments where the near infrared Nd:YAG excitation source was used. The spectrum shown in Figure 3.10 represents a 20 nm gold island film.

The FT-SERS spectrum of a single monolayer of the EuPc₂ on a 20 nm thick gold island film is

shown in Figure 3.11 (top trace). This spectrum was the second reported FT-SERS spectrum of a single monolayer thin film [50], though many examples have followed [60-62]. Although FT-Raman has the important property that the laser line that is used for FT-Raman experiments generally lies far from any electronic resonances, this was not clearly the case with EuPc₂. Weiss and coworkers have reported the observation of pre-resonant Raman enhancement in GdPc₂ using FT-Raman [52]. Hence, the FT-SERS spectrum of EuPc₂ did not resolve the problem of resonance enhancement effects versus spontaneous scattering, though important information was obtained.

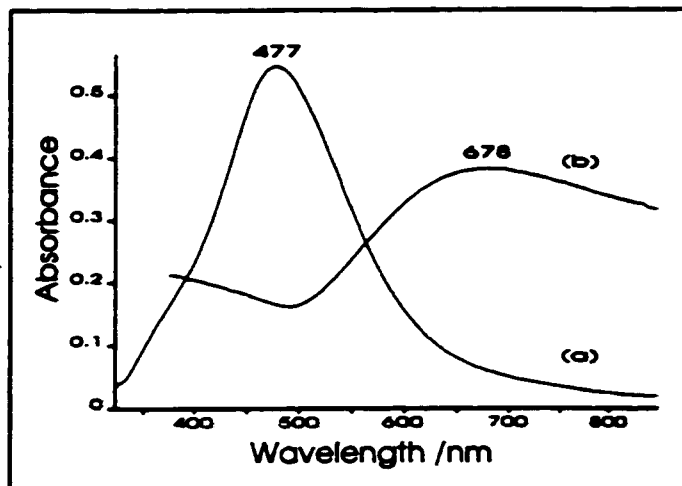


Figure 3.9: The plasmon absorptions of: (a) a 6 nm silver island film, and (b) a 4 nm gold island film on glass slides.

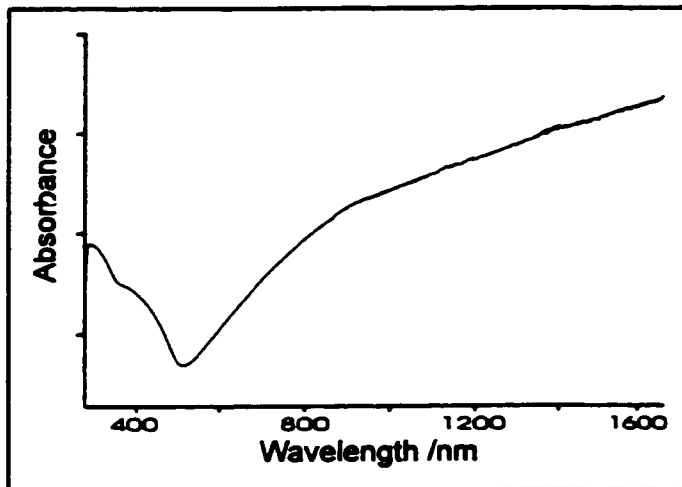


Figure 3.10: The plasmon absorption of a 20 nm gold island film on a glass slide.

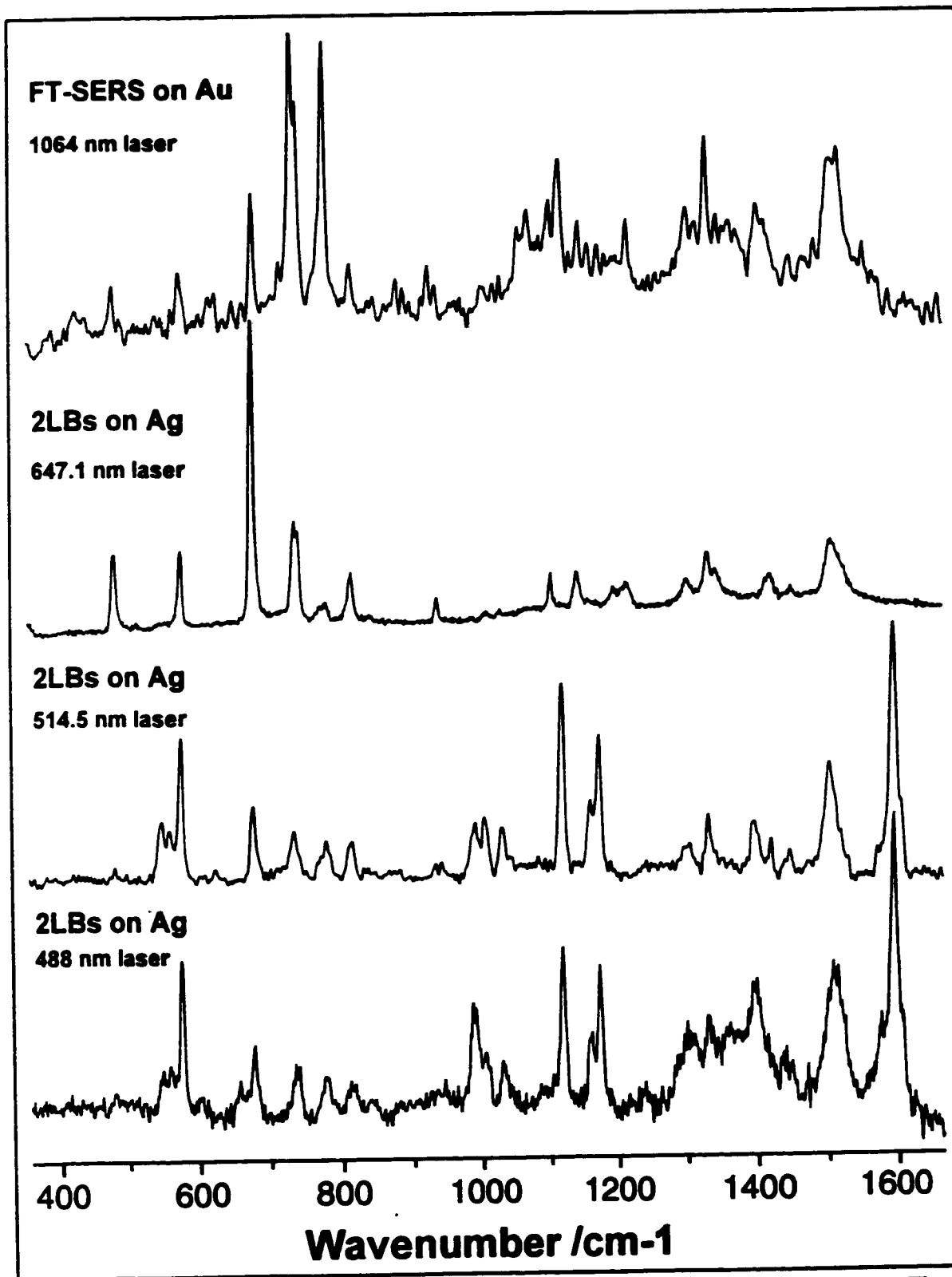


Figure 3.11: The surface enhanced Raman scattering spectra of LB monolayers. The laser lines and film characteristics are indicated for each spectrum

The bands which appear to show the greatest enhancement were found at 1331, 780, and 734 cm⁻¹. The latter two bands were clearly the most intense of the spectrum, and were assigned to a benzene breathing mode and a C-H wagging mode respectively. The 734 cm⁻¹ band was perhaps the most puzzling, since this band is nothing more than a shoulder in all of the other Raman spectra. It was possible that orientation effects may play an important role in the FT-SERS intensities, and they may not be directly comparable with the bulk spectra.

Since the FT-SERS observed with EuPc₂ was likely biased by orientation of the molecules on the metal island surface, a comparison with the SERS spectra of two LBs on silver island films is also shown in Figure 3.11. The decrease in relative intensity of the in-plane bands was typified by the striking decrease in the intensity of the C-H bending mode around 741 cm⁻¹, particularly in the SERRS spectrum recorded from the Kr⁺ laser line (647.1 nm). The effect of the orientation of the polarizability tensors for the normal modes is explained in terms of the propensity rules [63]. It is possible that the strong relative intensity of the out-of-plane C-H vibrations in the FT-SERS spectrum may be due to a nearly flat-on orientation of the molecules on the surface.

By comparison of the SERS spectra in Figure 3.11 with the bulk spectra of Figure 3.8, it can also be seen that there are subtle differences between the two sets of data. Since the vibrational frequencies are observed unshifted from those of the bulk (KBr pellets), chemisorption onto the metal surface is ruled out, and intensity changes should be associated with molecular orientation. For instance, the spectra where the green (514.5 nm) and blue (488 nm) lines of the Ar⁺ laser were used show an additional band at 986 cm⁻¹ which was not seen in any of the bulk spectra. This band was assigned to the C-H out-of-plane bending mode; nominally the ν_5 benzene vibration [64]. The significance of this band assignment is in the out-of-plane nature of this vibration, further evidence of the orientation of the molecules on the surface.

3.7 Conclusions

Floating monolayers of EuPc₂ with a limiting area of 1 nm² for the solid phase in π -A isotherm (tilted molecular orientation) were prepared. LB films probed using transmission infrared spectroscopy showed a nearly flat-on orientation of the molecules and no anisotropy in the dipping direction. Characteristic electronic transitions of EuPc₂ molecules were recorded in the UV-vis and near infrared spectral regions. Near infrared charge transfer transitions of an LB film, of a LnPc₂ compound, are reported here for the first time. The distinct Raman intensity patterns obtained in resonance with the Q-band (647.1 nm) and with the 488 and 514.5 nm laser lines are discussed in terms of the vibronic approach. The surface-enhanced Raman spectra of EuPc₂ LB films on metal island films including the FT-SERS of a single monolayer of EuPc₂ were also recorded. The conclusion from the SERS data was that the EuPc₂ molecules are physisorbed onto silver and gold. However, the relative intensity of several normal modes indicates the presence of a predominantly flat-on molecular orientation of the monolayer on the metal island film. The assignment of characteristic vibrational frequencies is given.

Chapter 4: Application of LB Films of EuPc₂ as an NO₂ Gas Sensor

In addition to the application of phthalocyanine complexes as dyes, scientists and engineers have uncovered considerable uses for these compounds due to their electrical and photoconductive properties [13, 65, 66]. Extensive studies of the electrical and photochemical properties of phthalocyanines, a p-type semiconductor, have been conducted on single crystals, compressed disks, evaporated films, and dispersions in polymer binders [65-68]. The electronic semiconductivity of Pc materials, particularly when exposed to small electron donating or accepting gaseous molecules, has helped foster much work towards the development of gas sensor devices utilizing these materials.

The fabrication and electrical characterization of Langmuir-Blodgett (LB) monolayer films of the bisphthalocyanine sandwich compounds having a central metal atom of the lanthanide series have drawn considerable attention. Previous work has concentrated on the electrical response to NO₂ (NO₂/N₂O₄) exposure on thin films of GdPc₂ [69], CePc₂ [46], TbPc₂ [37], and TmPc₂ [20]. In all cases an appreciable and reversible change in the conductivity of the films was noted upon exposure to the NO₂ dopant, however the magnitude of the response varied considerably. The central metal atom must therefore play a significant role in the conductivity of these films.

As well as the electrical measurements, many spectroscopic experiments have also been performed to study the changes of Pc thin films subjected to NO₂. In particular, UV-visible and surface enhanced Resonant Raman scattering (SERRS) spectroscopies were quite useful monitors of chemical changes of the Pc films due to the apparent reversible reactions with NO₂.

This work presents the electrical and spectroscopic behaviour of LB films of EuPc₂ when subjected to varying concentrations of NO₂. The adsorption-desorption process of NO₂ onto the LB film is discussed in context of the electrical response as

well as the UV-visible and SERRS spectroscopic changes. Additionally, electron spin resonance (ESR) spectroscopy was utilized to investigate the effect of NO_2 exposure on bulk samples of EuPc_2 , GdPc_2 , and LuPc_2 . These preliminary investigations gave further insight into the nature of the NO_2 chemisorption process.

4.1 Experimental

Several different experiments were performed to investigate the properties of LB films of EuPc_2 with particular emphasis placed on their applicability as an NO_2 gas sensor. The results of these experiments as well as ESR and FTIR experiments on bulk samples follow. A group of spectroscopic experiments were performed; the instrumental details of the UV-visible and SERRS experiments were given in Chapter 3. The particulars of the conditions used to record the spectra of LB films upon exposure to NO_2 are given within the context of the discussion of the spectra.

Thin film surface conductivity experiments were conducted using interdigitated gold electrodes [46]. An illustration of an interdigitated electrode is shown in Figure 4.1, the $25\ \mu\text{m}$ wide by $25\ \text{mm}$ long gold fingers were separated from each other by $25\ \mu\text{m}$ gaps. Deposition of an LB film onto the electrode closes the circuit and the electrical response of the thin films was recorded by a Keithley 617 programmable electrometer.

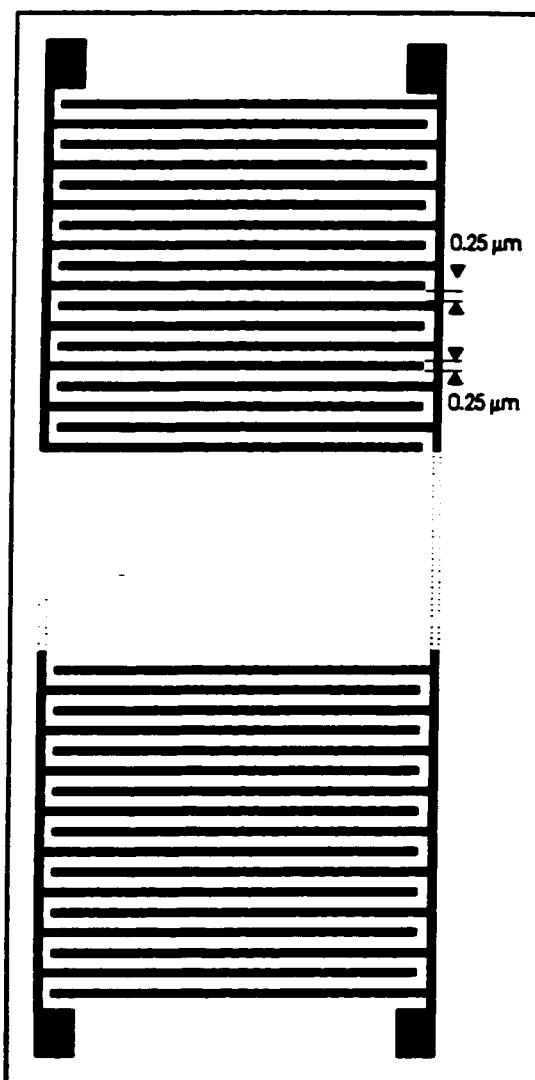


Figure 4.1: An interdigitated gold electrode used for surface conductivity experiments.

Analysed cylinders of 83 ppm and 1058 ppm NO_2 in nitrogen were purchased from Linde Specialty gases. Ultra pure (99.999%) nitrogen from Liquid Carbonic Inc. was used to dilute the NO_2 using the arrangement illustrated in Figure 4.2 to attain the desired concentrations of NO_2 . In all of the gas adsorption experiments, the total gas flow was held at $40 \text{ cm}^3\text{min}^{-1}$.

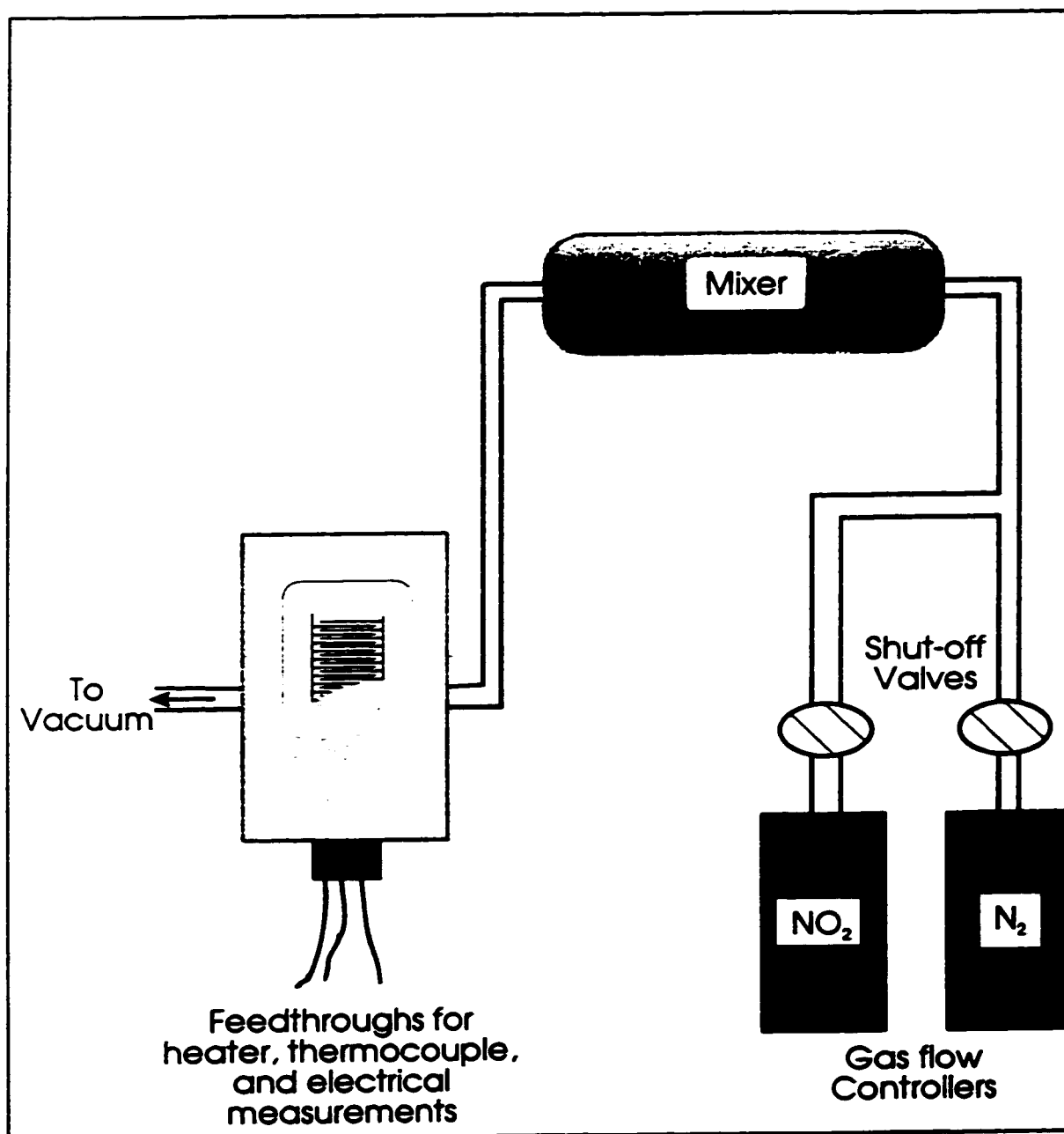


Figure 4.2: A schematic of the apparatus for mixing and flowing the NO_2/N_2 gas mixture over the EuPc_2 LB films on the interdigitated electrodes.

The EPR experiments were conducted on a Bruker ESP-300E spectrometer operating in the X-band microwave frequency (9.4 GHz) and the magnetic field was provided by 12 inch electromagnets capable of producing fields up to 1.5 Tesla. A variable temperature accessory to provide temperatures ranging from 500 K down to a lower limit of 100 K was utilized for the temperature dependant experiments.

4.2 UV-Visible and SERRS Spectroscopy

The UV-visible and near infrared absorption spectra of an LB film of EuPc₂ was reported [70] and discussed in Chapter 3. The predominant features of the electronic absorption spectrum of EuPc₂ consisted of very intense bands attributed to $\pi-\pi^*$ transitions of the conjugated macrocycle rings. These bands, nominally the Q-band (678 nm) and the B-band (323 nm), are typical of all phthalocyanines. Also visible were vibronic transitions of the Q-band at 604 nm. Bisphthalocyanine lanthanide compounds (LnPc₂) possess additional bands arising from transitions involving the half-filled HOMO level.

Langmuir-Blodgett films of EuPc₂ were prepared on glass slides. The films were exposed to NO₂ and the UV-visible absorption spectrum was recorded and compared to the spectrum of the newly deposited film. The marked changes in the electronic spectra of EuPc₂ LB films are illustrated in Figure 4.3. To the naked eye, the film changed from deep green to pale red. This phenomenon was indicative of the appreciable reduction of the intensities of the Q and B bands as well as the shifting of the wavelength of the band absorptions. For example, the Q-band shifts from 678 nm to 720 nm. The B-band was similarly affected. The charge transfer band has shifted from 468 nm to 516 nm, and it became relatively much more intense. All of these changes are indicative of an oxidation of the phthalocyanine ligand.

The UV-visible absorption spectrum of the NO₂ exposed film was recorded periodically. The film appeared to have completely recovered, indicating a completely reversible process. This can be seen in Figure 4.3 from the spectrum recorded two days

after NO₂ exposure. When the film was placed in vacuum, the film recovered much more rapidly, as would be expected.

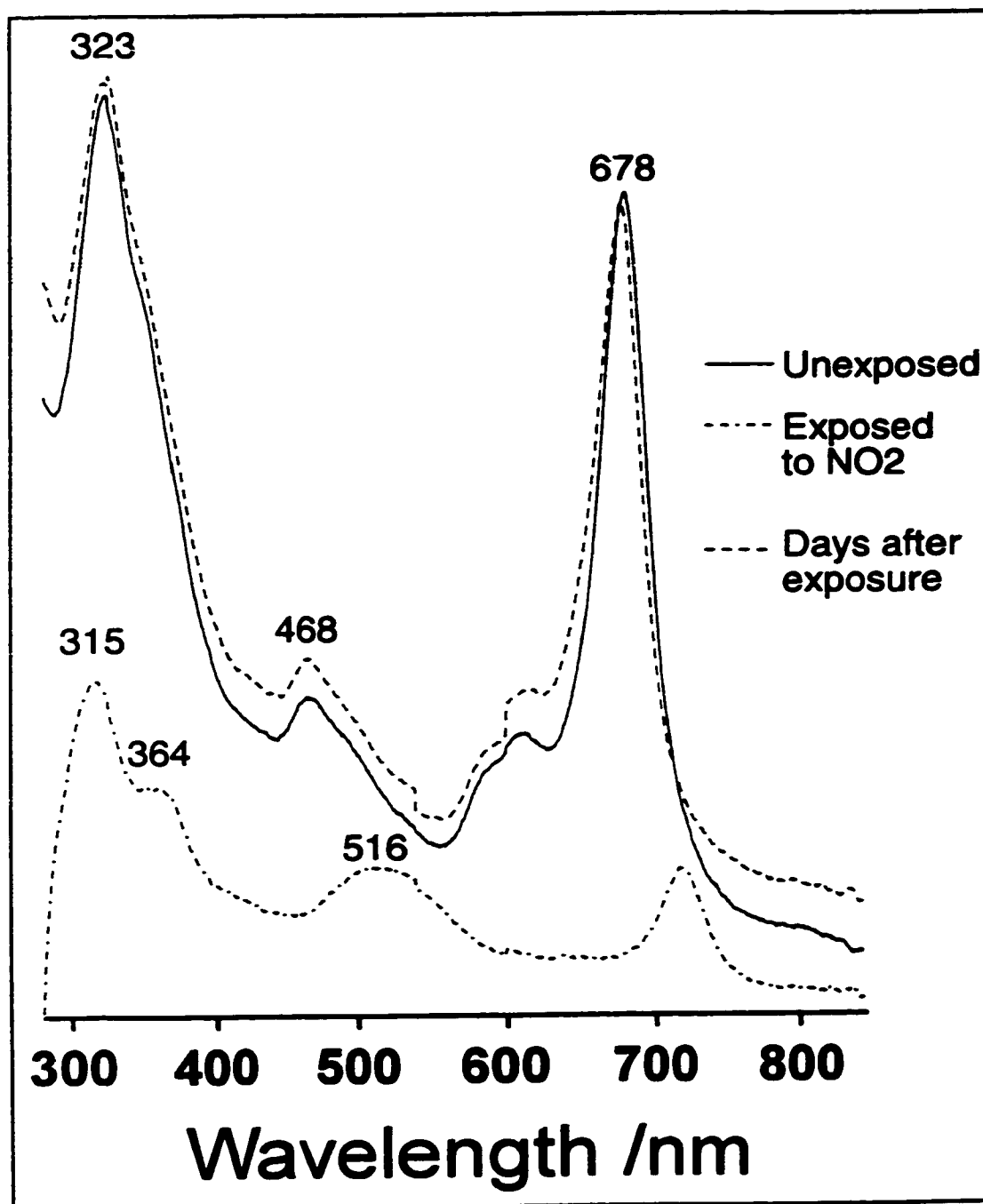


Figure 4.3: The UV-visible spectra of EuPc₂ LB monolayers on glass before and after exposure to NO₂. While the colour change in the film immediately following exposure was remarkable, the film seemed to recover with time.

Another LB film of EuPc₂ was prepared on a 4 nm thick gold island film. The surface enhanced resonance Raman scattering (SERRS) spectrum of the neat film was recorded. This film was exposed to NO₂ and the SERRS spectrum was once again recorded periodically to monitor film recovery.

The nature of resonance Raman scattering causes the greatest enhancement to be seen for those normal modes having a considerable degree of character associated to the absorbing chromophore. Since the 647.1 nm Kr⁺ laser line was used, this RRS experiment gives information of the macrocycle normal modes because this laser line was in resonance to the very intense $\pi\text{-}\pi^*$ transition.

The results of the SERRS experiments are illustrated in Figure 4.4. The top trace shows the clean LB film of EuPc₂. The next trace shows the same film immediately following exposure to NO₂. A considerable change in the SERRS spectra was clearly evident. Most notably, the macrocycle breathing mode at 680 cm⁻¹, having the highest intensity in the clean film spectrum, was quite weak in the exposed film spectrum. Also, an aromatic C-C, C-N vibration at 1550 cm⁻¹, barely coming out of the baseline in the clean film, was the most intense band in the exposed film spectrum.

The next trace shows the SERRS spectrum of the same exposed film two hours later. Already the film had begun to recover. The final trace gives spectroscopic evidence to the reversibility of the chemisorption process.

4.3 Electrical Measurements

The electrical measurements of LB films was facilitated through the use of interdigitated electrodes (IDE). The electrode consisted of 600 fingers of gold that were 25 μm wide by 25 mm long. The opposing digits were separated by 25 μm gaps. The experimental details were given elsewhere [46].

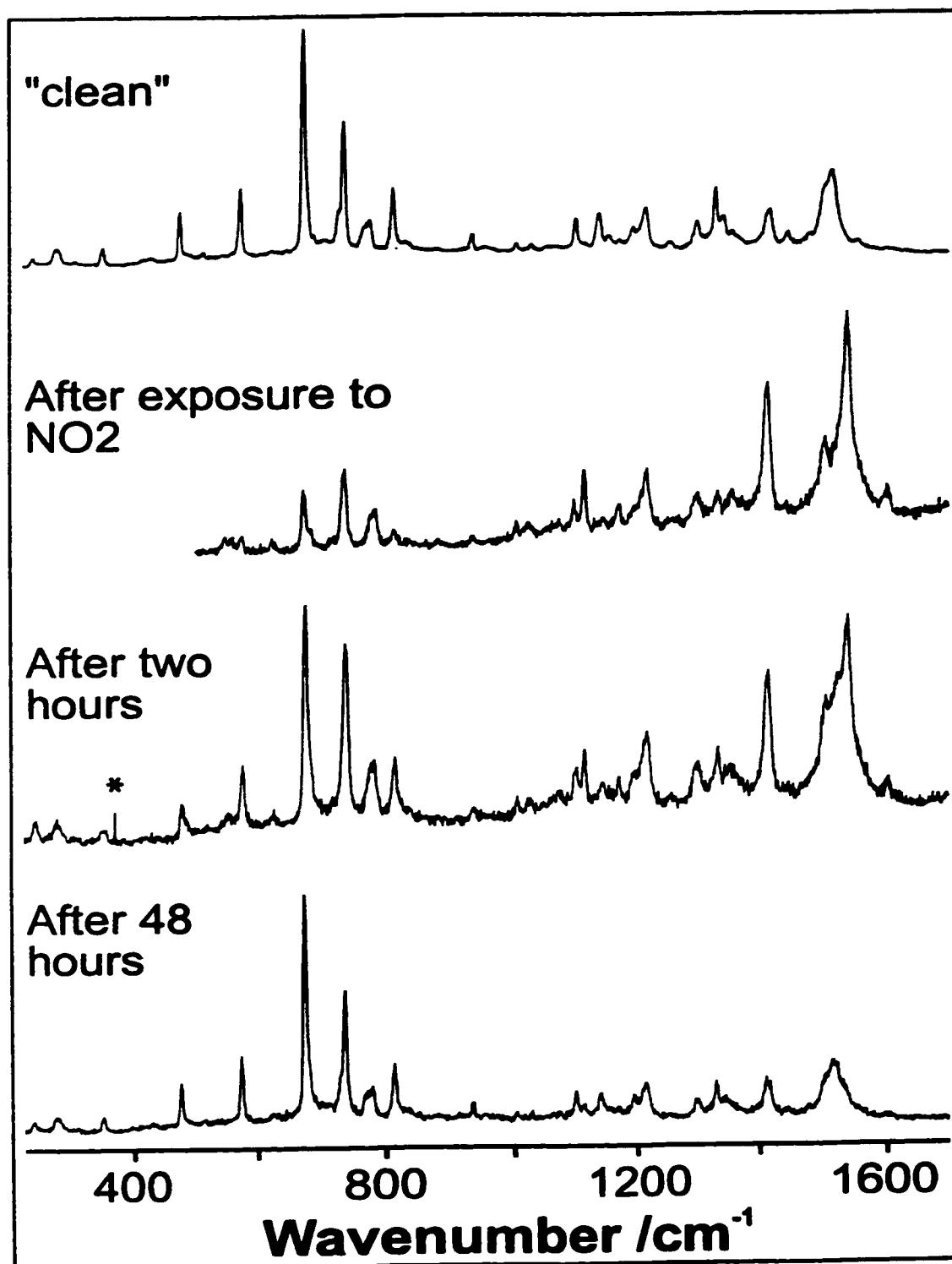


Figure 4.4: The SERRS spectra of EuPc_2 LB film on 4 nm gold island film using the 647.1 nm Kr^+ laser line. The spectra show the dramatic and reversible changes brought on by NO_2 gas exposure.

After LB films of EuPc₂ were transferred to the IDE, the electrode was tested to ensure good Ohmic contact was made between the LB film and the gold electrode. The results of such a test are shown in Figure 4.5. The current through the circuit was measured as the applied potential was varied.

Clearly from the results of Figure 4.5, Ohm's Law ($V = IR$) was obeyed for the potential range from -1.00 V to +1.00 V. Unless otherwise noted, the potential used in all of the electrical conductivity experiments used a potential

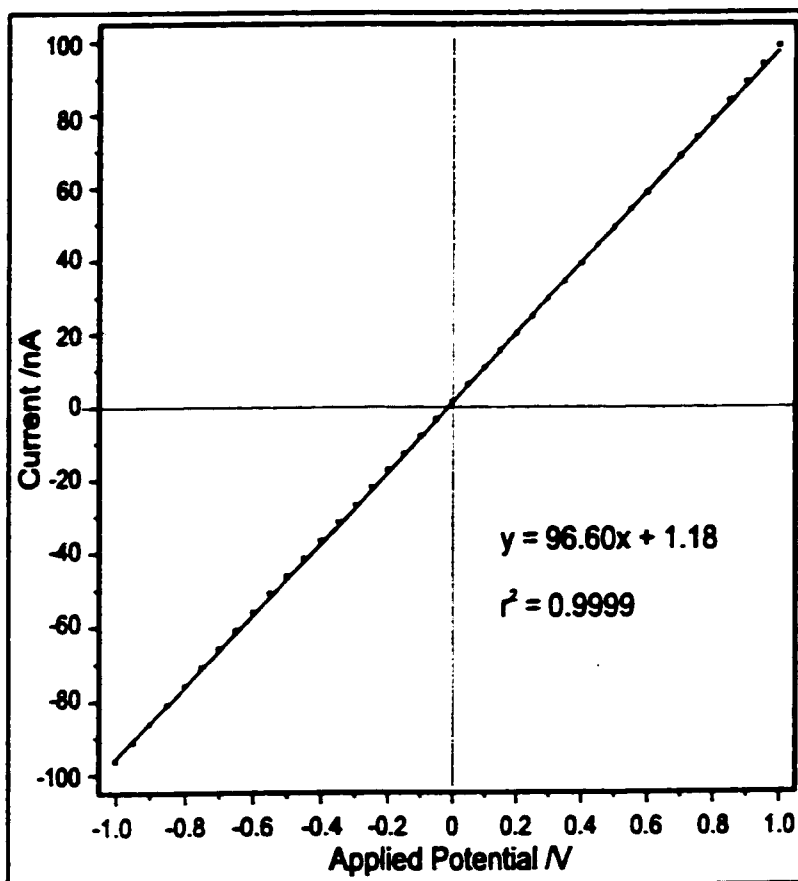


Figure 4.5: The results from the test of the junction between the LB film and the gold electrode. of 0.50 V.

4.3.1 Thermal Conductivity of EuPc₂ LB Films

The thermal conductivity of EuPc₂ LB films were measured from room temperature up to 200 °C (see Figure 4.6). During the first cycle, the conductivity shows a local maximum at about 140 °C. This corresponds to the desorption of trapped atmospheric gases, particularly oxygen. When the film was kept under vacuum, the second and subsequent cycles all follow the exponential increase in the conductivity as a function of temperature that is expected of a semiconductor material, as is shown in Figure 4.6(b).

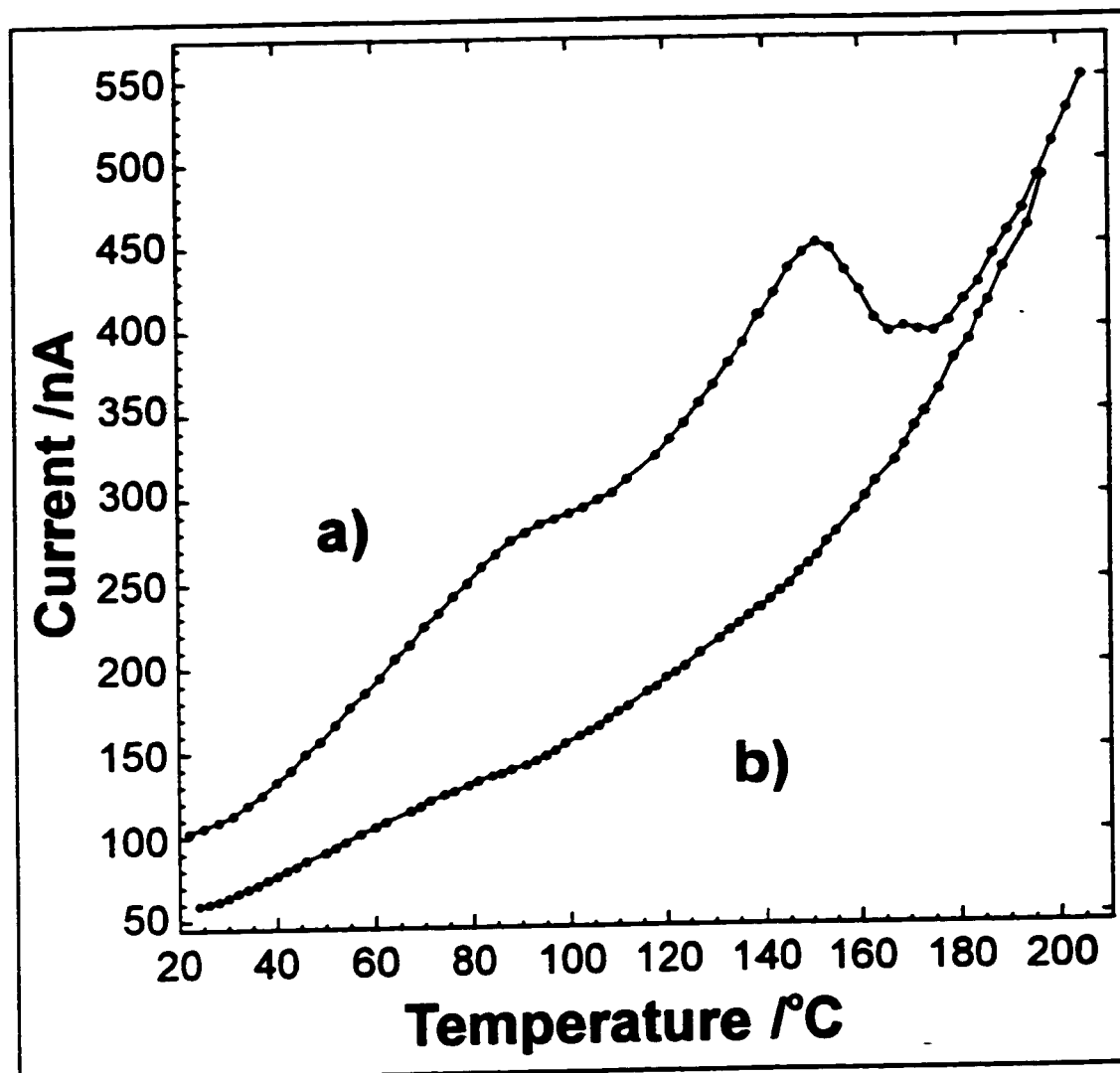


Figure 4.6: The thermal conductivity measurements of an LB film of EuPc₂: (a) represents the first cycle where trapped oxygen was released and (b) represents subsequent cycles.

The activation energy for conduction was determined using the common expression for conduction in semiconductors:

$$\sigma = \sigma_0 e^{-\frac{E_a}{2kT}} \quad (4.1)$$

where σ is the conductivity, k is the Boltzmann factor, T is the absolute temperature, and E_a is the activation energy. From the semilogarithmic plot of conductivity versus $1/T$ shown in Figure 4.7, the activation energy was found to have a value of 0.27 eV (from

the data, $\ln(\sigma) = -11.63 - 1569.5/T$; $r^2 = 0.993$). This was comparable to the values obtained for other LnPc_2 films as indicated by the table of activation energies for various LnPc_2 samples reported in Table 4.1. Note that the activation energies for LB films of TmPc_2 and TbPc_2 were higher than for EuPc_2 . The europium centred complex was therefore going to be more responsive to NO_2 gas since the barrier to conduction was lower.

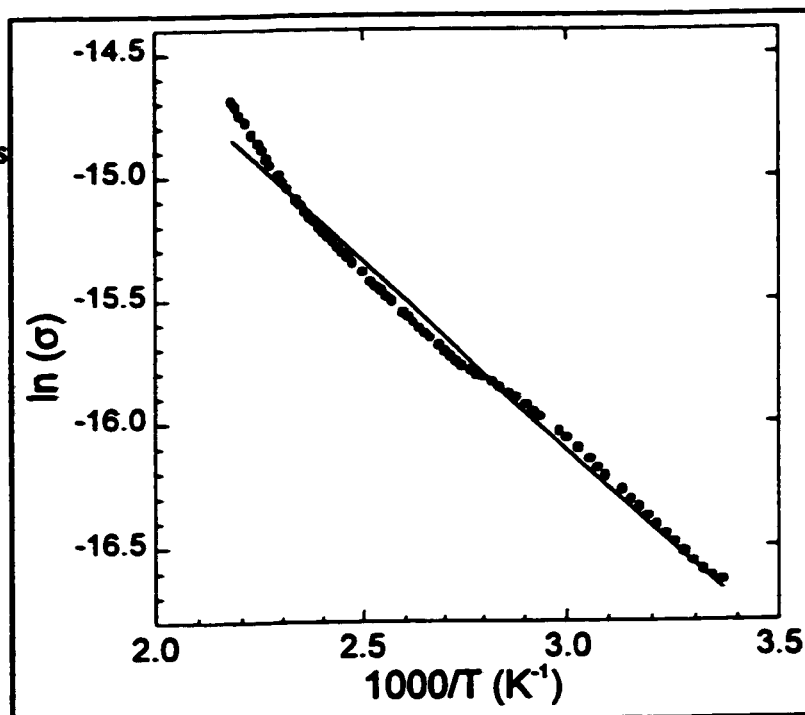


Figure 4.7: The semilogarithmic plot of conductivity versus reciprocal temperature.

Table 4.1: The activation energies of conduction for a variety of LnPc_2 complexes.

Complex	Form	E_a (eV)	Reference
LuPc_2	Single Crystal	0.64	71
LuPc_2	Evap. Film	0.2	72
YbPc_2	Evap. Film	0.4	72
TmPc_2	Evap. Film	0.28	22
TmPc_2	LB Film	0.36	20
DyPc_2	Evap. Film	0.2	72
TbPc_2	LB Film	0.38	37
YPc_2	Evap. Film	0.3	72

4.3.2 Electrical Response of EuPc₂ LB Films to NO₂

The response of the EuPc₂ chemiresistor was measured by applying a constant potential of 0.5 V to the film and monitoring the current as the NO₂ flowed over the sample. The electrical response to an NO₂ concentration of 2 ppm was monitored; the current (and hence conductivity) change was slight, but measurable. The NO₂ flow was stopped and the desorption process monitored once again by measuring the current change as a function of time under a constant potential. The cell was pumped out for several hours to remove the residual NO₂, and the experiment was repeated with several NO₂ gas concentrations. The results of such experiments are shown in Figure 4.8. Clearly the response increased for higher concentrations of NO₂, and the sensor began to approach saturation after 25 min. One other important observation was that the

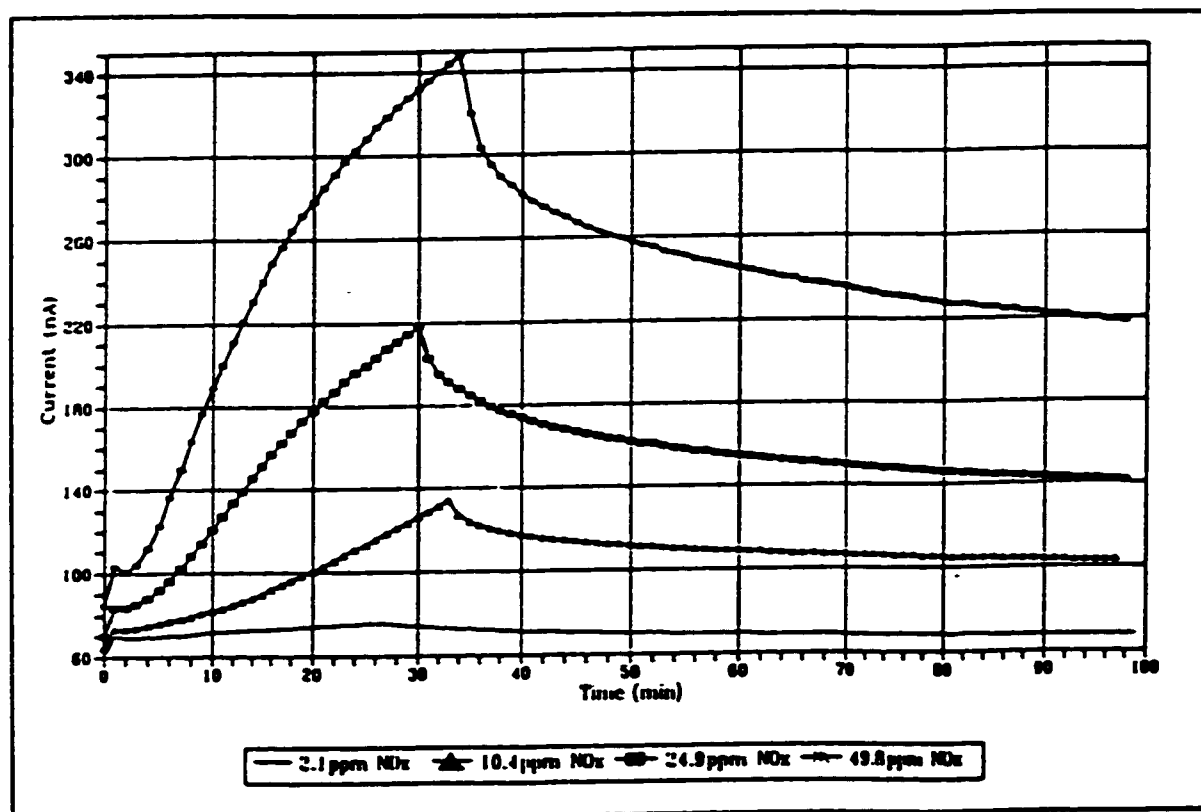


Figure 4.8: The electrical response of the LB film when exposed to various concentrations of NO₂ gas in N₂.

desorption rate was much slower than the adsorption rate.

The rate of NO₂ adsorption may be described in a first approximation by the Elovich equation:

$$\frac{d\theta}{dt} = A e^{-\frac{E_0 + \alpha\theta}{RT}} \quad (4.2)$$

where θ represents the fraction of surface covered, A is a constant at a given pressure, α is a constant for a given surface, and $(E_0 + \alpha\theta)$ is the activation energy of the adsorption process (E_a). An analogous expression gives the desorption rate:

$$-\frac{d\theta}{dt} = B e^{-\frac{E_0 + \beta\theta}{RT}} \quad (4.3)$$

Assuming that the change in the film conductivity is proportional to the surface coverage, then equations 4.2 and 4.3 may be rewritten in terms of the change in conductivity with respect to time. Solving equations 4.2 and 4.3 gives

$$\theta_{ads} = \frac{RT}{\alpha} \ln(t/t_0 + 1); \quad t_0 = \frac{RT}{\alpha A} e^{\frac{E_0}{RT}} \quad (4.4)$$

and

$$\theta_{des} = \theta_0 + \frac{RT}{\beta} \ln(1 - t/t'_0); \quad t'_0 = \frac{RT}{\beta B} e^{\frac{E_0 + \beta\theta_0}{RT}} \quad (4.5)$$

The current change as a function of the logarithm of elapsed time should therefore give linear relationship [37]. Such Elovich plots are given in Figure 4.9. The results indicate that the adsorption-desorption kinetics are well represented within the Elovich's approximation. However, the adsorption data showed a well defined incubation period, seen just before the linear part of the Elovich's plot in Figure 4.9.

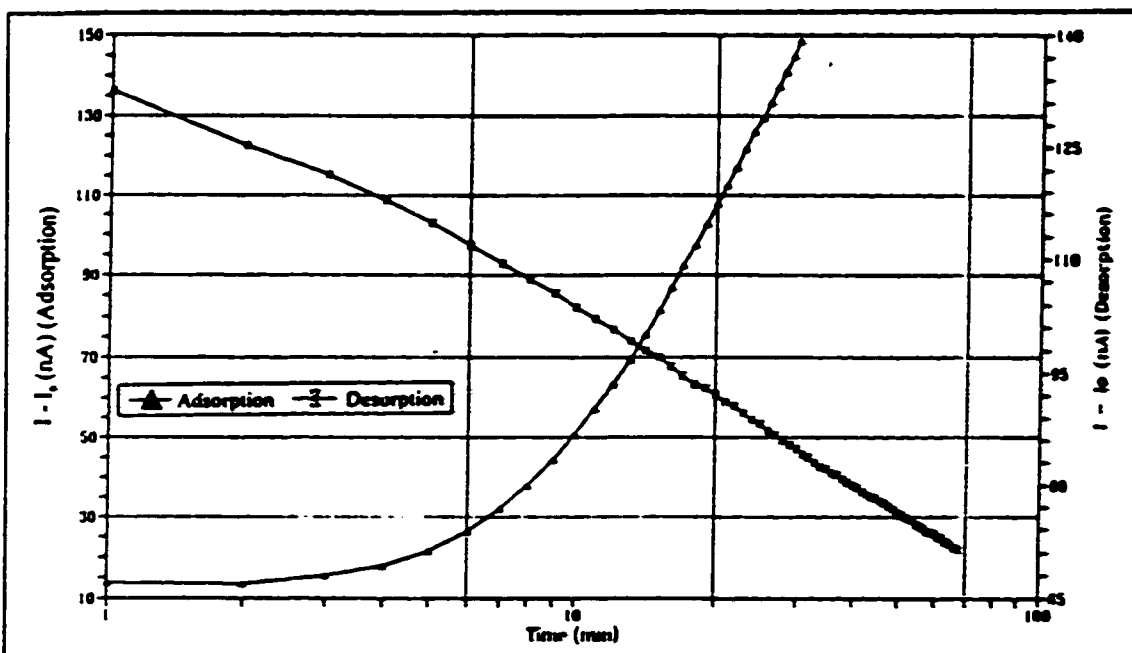


Figure 4.9: Elovich plots of adsorption (left axis) and desorption (right axis) of 24.9 ppm of NO₂.

The incubation period for adsorption was clearly seen in the raw data current versus time as shown in Figure 4.10. The trial 3 in this figure, correspond to NO₂ adsorption by the same film that had been previously annealed for six hours at 375 K. After heating, it was evident that the response was immediate and the delayed response time had disappeared. As was mentioned earlier, the desorption rate was quite slow. This data displays evidence that when the sensor was exposed to higher concentrations of NO₂ the film could not completely recover simply by pumping on the cell. Heat was needed to desorb the more strongly adhering NO₂ molecules in the same way the heat was used to initially remove the atmospheric oxygen from the films. This last point seems to contradict the spectroscopic findings which suggested that the films recovered completely. Consequently, the notion that the electrical conductivity experiments would be far more sensitive to NO₂ gas exposure than spectroscopic experiments has been reaffirmed.

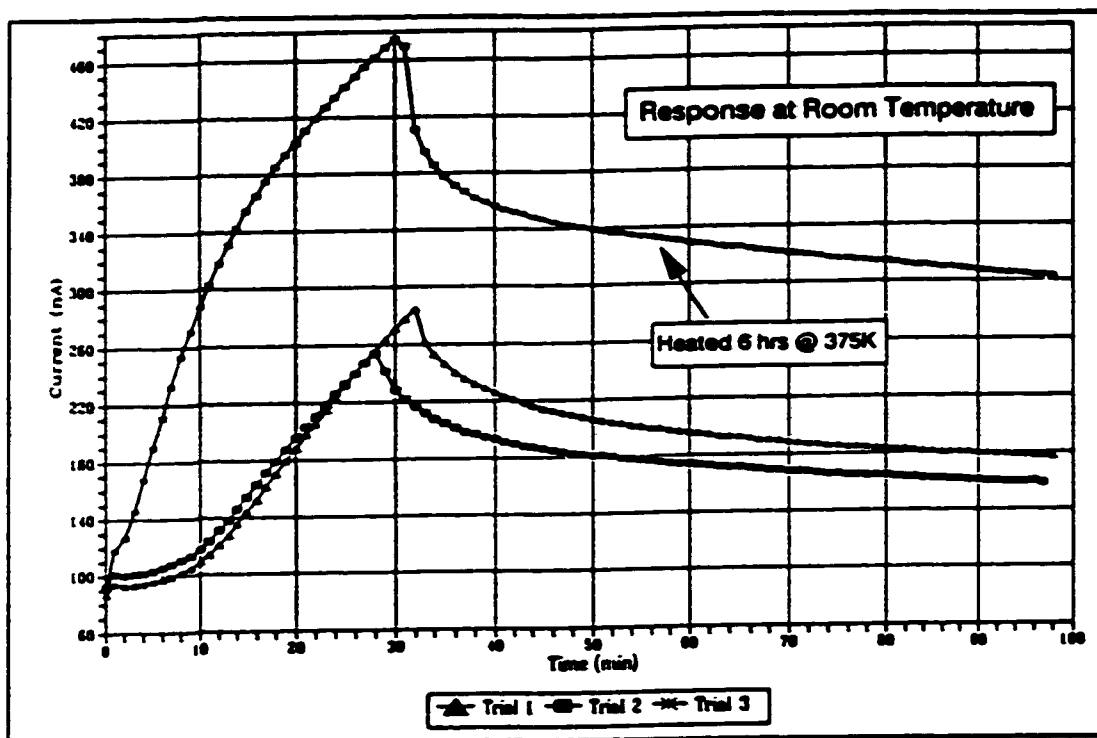


Figure 4.10: The response of the sensor to 105.8 ppm NO₂. The first two trials show significantly inhibited initial response. The third trial was conducted after the sensor was thermally treated for six hours; the film response was greatly enhanced.

The persistent presence of NO₂ in LB films of phthalocyanine compounds was also observed by Lando *et. al.* for the axially substituted amphiphilic dimer [(C₆H₁₂)₃SiOSiPcOGePcOH] [38]. It was hypothesized that two processes were involved to cause the conductivity changes in Pc films exposed to gases, namely a fast process due to surface adsorption and a slower process due to bulk diffusion [38, 73]. The NO₂ molecules that were absorbed into the bulk were more strongly bound within the solid than those adsorbed on the surface, and thus required additional energy from heating to effect their removal.

In addition to the kinetics of NO₂ adsorption, the thermodynamics was also examined in order to discern the sensor response as a function of the NO₂ concentration. While the Langmuir isotherm applies very well to systems where physisorption was the predominant adsorption process, the Temkin isotherm better describes the cases where the chemisorption process was important [74]. The Temkin isotherm modifies the

Langmuir isotherm by including a factor that imparts a linear dependence on the heat of adsorption with respect to surface coverage, *i.e.* $Q = Q_0(1 - \alpha\theta)$. The Temkin isotherm then takes the form

$$\theta = \frac{RT}{\gamma} \ln P + \text{constant} \quad (4.6)$$

where $\gamma = Q_0\alpha$ and P is the partial pressure of the adsorbate. This expression was used in the analysis of the sensor response when saturated with different concentrations (10.4, 24.9, 49.8, and 105.8 ppm) of NO₂ gas. The semilogarithmic plot of the current versus gas concentration at 300 K is given in Figure 4.11 and shows good agreement with Temkin's empirical model.

Since the sensors took more than twenty five minutes to reach saturation, it was instructive to investigate the film response at shorter exposure times. The conductivity data was analysed for four different exposure times, and the results are plotted in Figure 4.12. Interestingly, the sensor response after five minutes was very nearly linear.

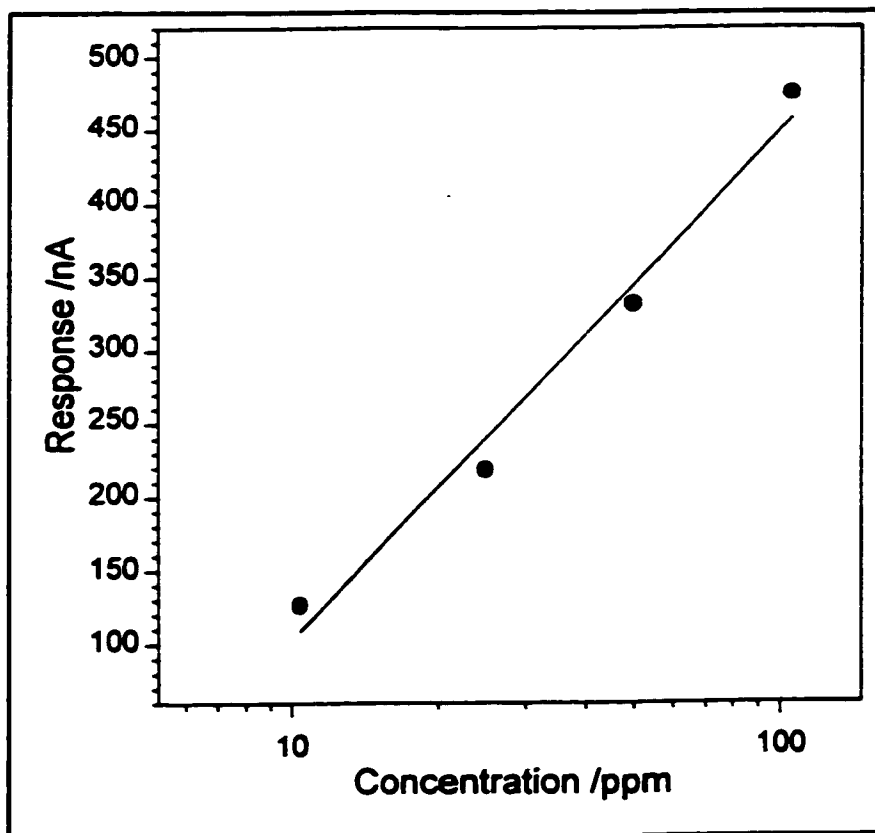


Figure 4.11: The response of the gas sensor to various concentrations of NO₂ gas at 300 K.

The results from the conductivity experiments after exposure to NO₂ and desorption by heating at 375 K posed some intriguing questions. Why do the

spectroscopic techniques fail to detect the residual NO₂? And does the exposure to NO₂ somehow alter the film structure? The technique of electron spin resonance (also known as electron paramagnetic resonance, and hence the dual acronyms ESR and EPR) spectroscopy was engaged to try to shed some light on these queries.

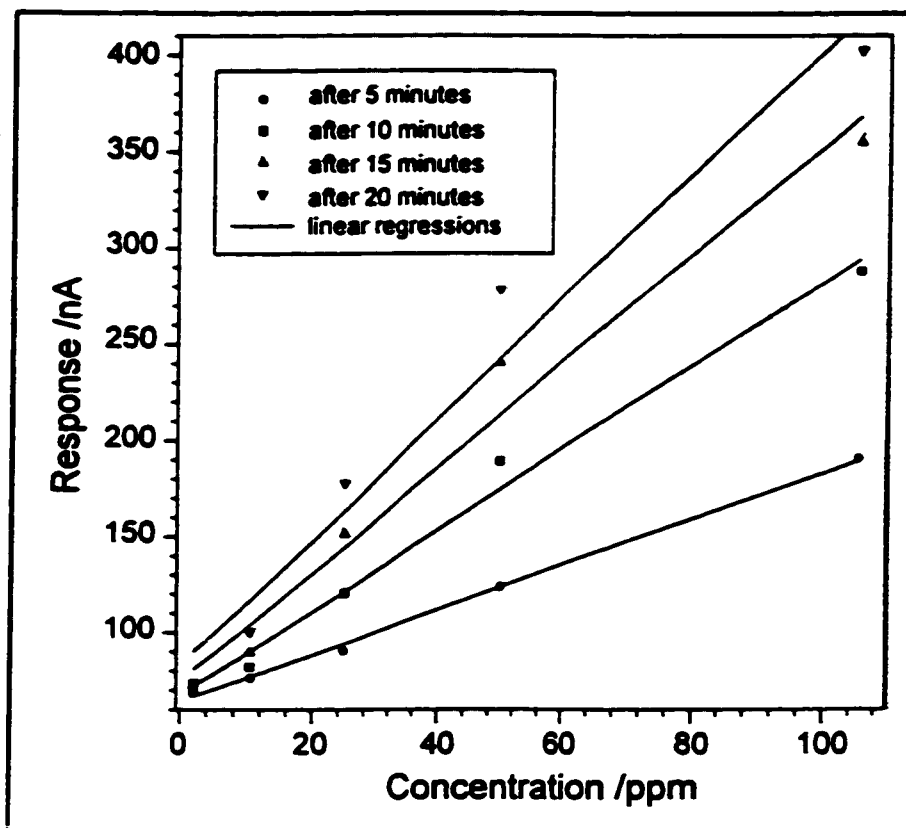


Figure 4.12: The sensor response to various gas concentrations at 5, 10, 15, and 20 minute intervals.

4.4 Discussion of EPR Experiments

It was assumed that the electrical measurements were indicative of a change in film structure resulting from the absorption of NO₂ molecules into the film. Such structural changes were not reflected in the UV-visible and SERRS experiments but the spectroscopy did show that the films recovered completely after exposure to NO₂ without change in the molecular energy states. In fact, the rate of recovery was quite fast even at ambient conditions. Consequently, new experiments were required to help interpret the electrical measurements. Since both the EuPc₂ and NO₂ molecules have unpaired electrons, EPR spectroscopy is a simple tool that is sensitive to any changes in the EuPc₂ due to NO₂ exposure. To that end, a series of preliminary EPR experiments

were performed on europium, gadolinium and lutetium bisphthalocyanine compounds.

First, the spectra of the bulk pure LnPc_2 ($\text{Ln}=\text{Eu}$, Gd , and Lu) compounds were recorded at various temperatures. In all cases, the intensities were inversely proportional to temperature, indicating that the materials obeyed the Boltzmann law. The spectra of EuPc_2 and GdPc_2 were more complicated than that of LuPc_2 due to the fact that the Eu^{3+} and Gd^{3+} ions have open valence shells, $4f^6$ and $4f^7$ respectively; whereas the Lu^{3+} is a closed shell $4f^4$. Therefore, the spectrum of the LuPc_2 compound results only from the unpaired electron on the Pc^- radical, while the EuPc_2 and GdPc_2 spectra were a convolution of the ligand and metal unpaired electrons.

The EPR spectrum of EuPc_2 in toluene at 77 K is shown in Figure 4.13 along with two spectra illustrating the effect of NO_2 exposure. Not only did the apparent intensity of the signal increase, but fine structure began to be resolved.

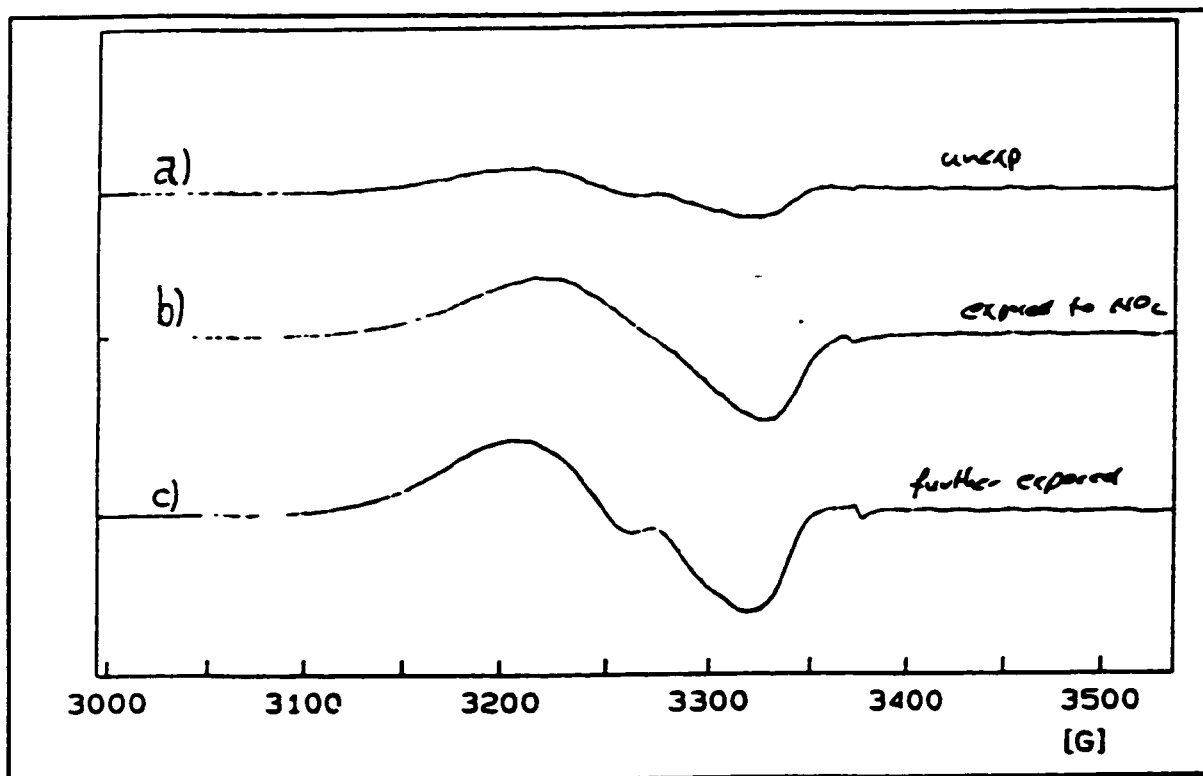


Figure 4.13: The EPR spectra recorded at 77 K of: (a) the pure EuPc_2 compound dissolved in toluene, and (b,c) the same sample exposed to increasing quantities of NO_2 .

Next, bulk quantities $\text{LuPc}_2\text{-NO}_2$ adducts were prepared in order to attempt to quantify the results. This was accomplished by first dissolving the pure compound in toluene or chloroform and then flowing a mixture of NO_2/N_2 (approx. 500 ppm NO_2) through the solution. The solutions turned red and then clear as a dark red precipitate was formed. The solution was filtered and the precipitate collected for EPR analysis.

The temperature dependent EPR experiments were done as follows: first the sample was cooled to 98K and the spectrum was recorded. A series of spectra were recorded at various intervals while the temperature of the sample was slowly increased to 500K. The samples were then cooled back to 98K. These cooling and heating cycles were repeated and the spectra were recorded.

The peak intensities of the from the EPR spectra of the lutetium complex are tabulated in Table 4.2. The peak intensities for the $\text{LuPc}_2\text{-NO}_2$ adduct proved to behave in a non-Boltzmann manner; *i.e.* the intensities increased with temperature. This was not the case for the neat compound which suggests some kind of transformation since after heating to 500 K, all of the NO_2 should have been desorbed. The spectrum of the pure LuPc_2 complex could never be recovered.

Table 4.2: The EPR peak intensities for LuPc_2 and the $\text{LuPc}_2\text{-NO}_2$ adduct.

Temperature /K	LuPc_2 (5 mg sample)		$\text{LuPc}_2\text{-NO}_2$ (2 mg sample)	
	Intensity	I x T	Intensity	I x T
500	46.7	23350	5.53	2765
400			5.04	2016
300	78.8	23640	3.83	1149
250			3.55	887
200	114	22800		
100			0.11	11

The EPR spectrum of GdPc_2 changed markedly upon exposure to NO_2 . The spectra of GdPc_2 at room temperature and at 100K are shown in Figure 4.14, and the

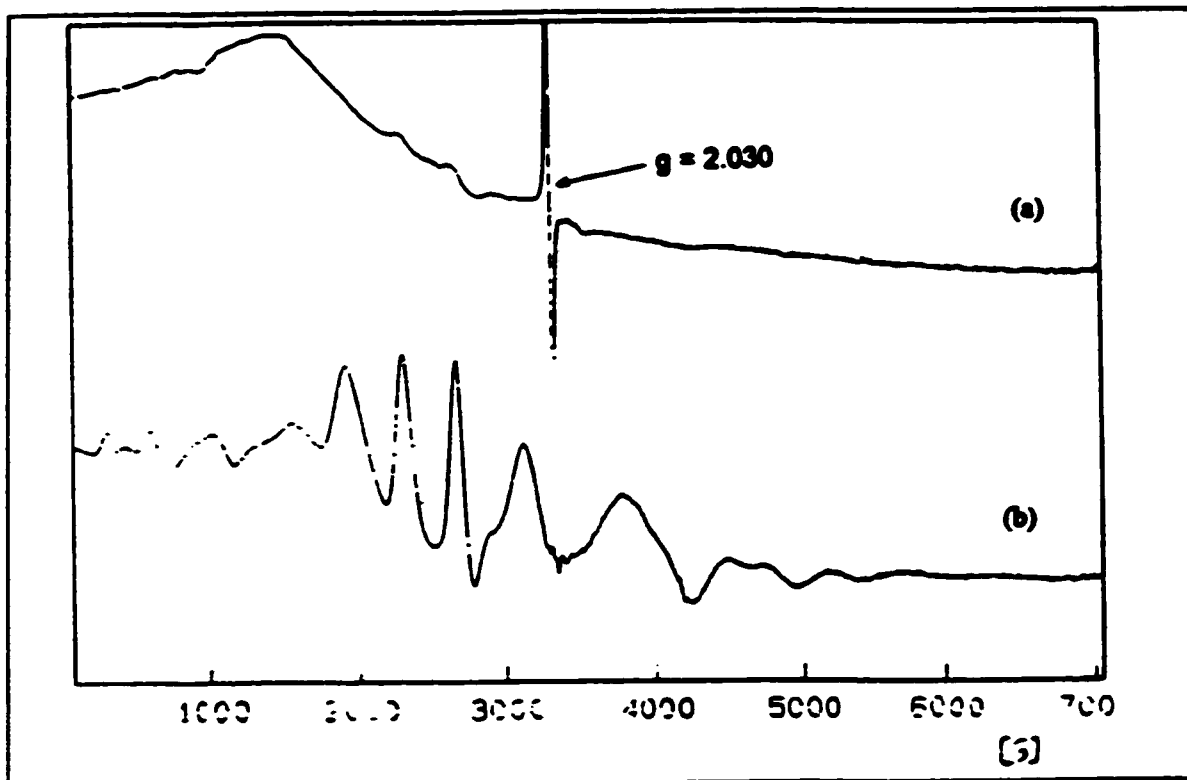


Figure 4.14: The EPR spectra of a sample of GdPc_2 at: (a) room temperature, and (b) at 100 K.

temperature dependent spectra of the $\text{GdPc}_2\text{-NO}_2$ adduct are shown in Figure 4.15. As with the lutetium complex, the temperature dependence of the peak intensities of the adduct complex did not follow Boltzmann statistics. It seems that the exposure to NO_2 causes the formation of a low spin state with a low lying high spin excited state nearby. This change persists even after the NO_2 has been desorbed. One possible explanation for this observation is that the NO_2 catalysed a phase transition in the material. Such phase transitions were seen for LB films after heating [75].

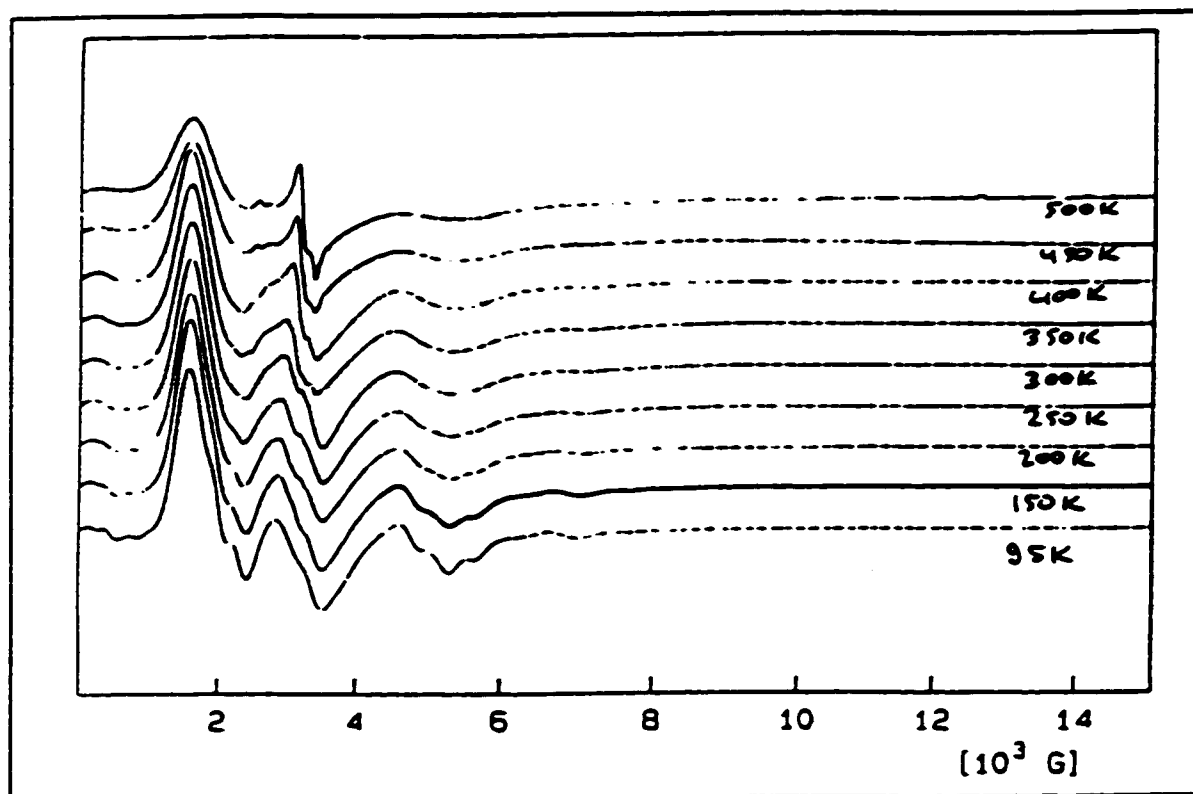


Figure 4.15: The temperature dependent EPR spectra of a sample of GdPc_2 after exposure to NO_2 gas.

4.5 Conclusions

Langmuir-Blodgett monolayer films of EuPc_2 were applied as NO_2 gas sensors. Their response was measured spectroscopically using UV-visible absorption and SERRS spectroscopies. From the spectroscopic data it was determined that the effects of gas exposure on the LB films were dramatic and reversible.

The effects on the electrical conductivity of the films due to gas exposure were also dramatic. They did not however prove to be reversible as it was necessary to heat the sensor under vacuum to completely recover the film. Preliminary EPR experiments to study the effects of NO_2 exposure on LnPc_2 complexes suggested a completely irreversible transformation had occurred.

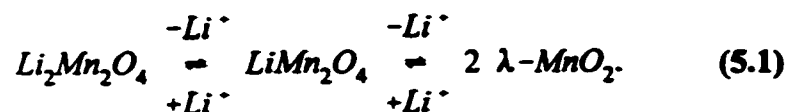
Chapter 5: Thin Film Lithium Microbattery

5.1 Introduction to Microbattery Research

Ever since the first transistor radios hit the market more than thirty years ago, the electronics industry has been driven to meet the insatiable demand for newer, smaller, and more technologically advanced electronic gadgets such as cellular phones, pagers, daily planners, and camcorders. Indeed, the extraordinary success the microelectronics industries have had in the miniaturization of the electronic components has made it possible for computers that as recently as twenty years ago would have filled a room, can now easily slip into an average brief case. To enhance the portability of these high-tech devices, the development of small secondary batteries possessing high energy density and capable of delivering reliable power over hundreds of cycles is of paramount importance. Secondary lithium batteries have demonstrated immense potential for such applications; as with the miniaturization of the electronics components, the miniaturization of their power sources is drawing considerable attention [76-78].

Secondary lithium batteries (and all batteries in general) consist of three main components: an anode, an ionic conductor, and a cathode. The early lithium batteries used metallic lithium as the anode material, but its high reactivity and explosive instability at higher temperatures has prompted the use of materials such as graphite that facilitate the safe storage of lithium atoms during the charge/discharge cycles by intercalation/deintercalation between the graphene layers. The ionic conductor consists of a lithium salt in solution. Truly solid state batteries utilize polymer electrolytes or ionically conductive glasses, but many lithium battery applications can use liquid electrolyte.

The nucleus of the work presented here involved the preparation of thin film cathodes; in particular, the focus has been on lithiated manganese oxide (LiMn_2O_4). The bulk material is known to extract and insert lithium reversibly by electrochemical means:



Some advantages that this material possesses over lithium intercalation transition metal oxides such as LiCoO_2 and LiNiO_2 include very low cost and a much lower level of toxicity.

Unlike the intercalation compounds such as LiCoO_2 and LiNiO_2 which form a layered structure, the LiMn_2O_4 forms a stable spinel phase. This spinel phase is analogous to the well known MgAl_2O_4 mineral and can be ascribed the general formula AB_2O_4 . The spinel phase consists of a cubic closest packed array of oxygen anions; in a *normal* spinel, the B cations occupy one half of the octahedral sites (denoted by $[\]^{\text{oct}}$) while the A cations occupy one eighth of the tetrahedral sites ($[\]^{\text{tet}}$). This is denoted by



The unit cell contains eight formula units ($Z=8$) corresponding to the formula " $\text{A}_8\text{B}_{16}\text{O}_{32}$ ". A diagram of the unit cell is shown in Figure 5.1 where two sides of the cubic cell lie in the plane of the page and the third is projected out of the page. The numbers beside each of the atoms indicate the distance above the page in units of cell parameter "a". To help illustrate the sites occupied by the cations, one eighth of a unit cell is shown in Figure 5.2.

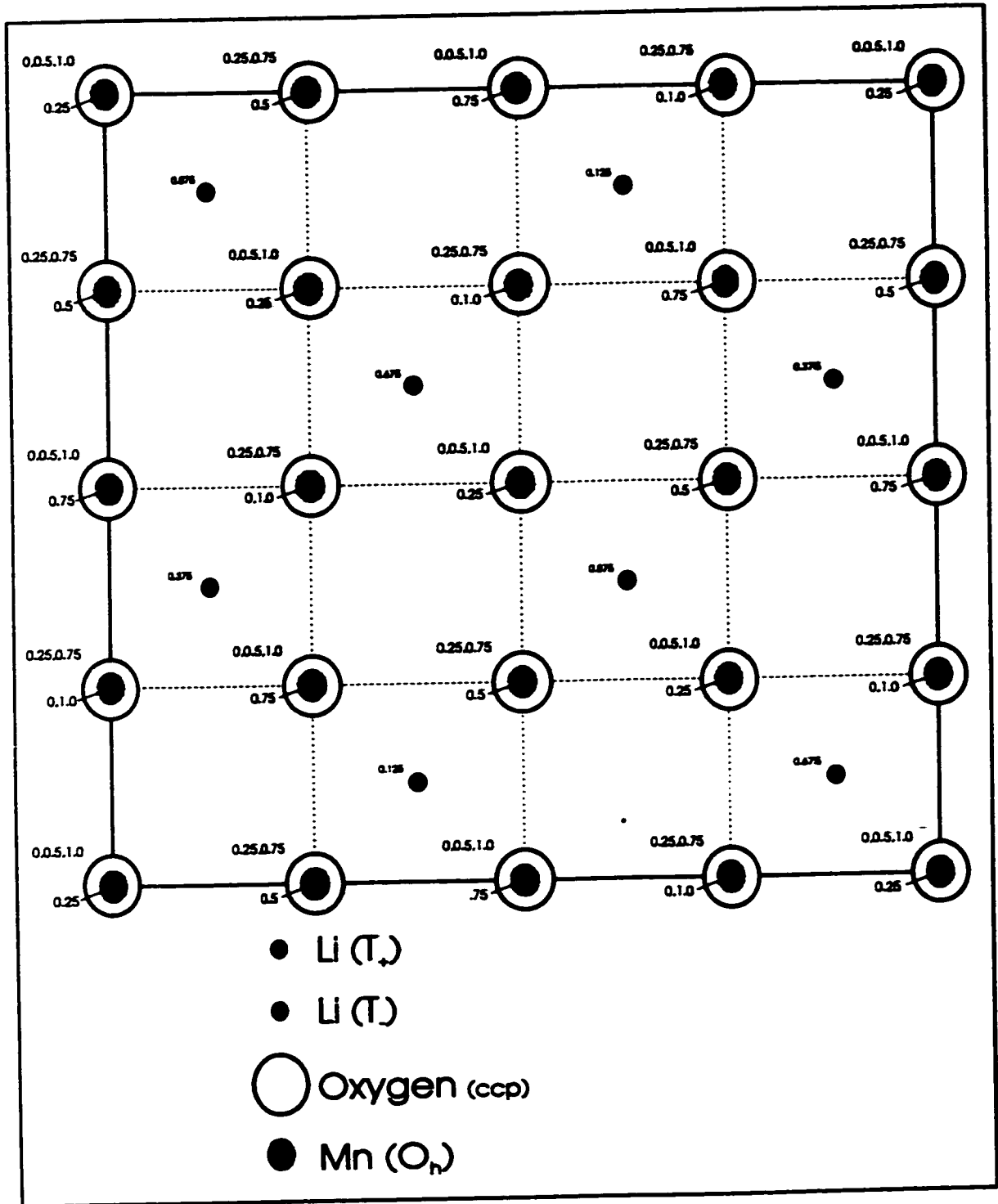


Figure 5.1: An illustration of the LiMn_2O_4 spinel unit cell. Two of the cell indices lie in the plane of the page while the third is projected out from the page. The numbers indicate the fraction of cell parameter "a" above the plane where the atoms are located.

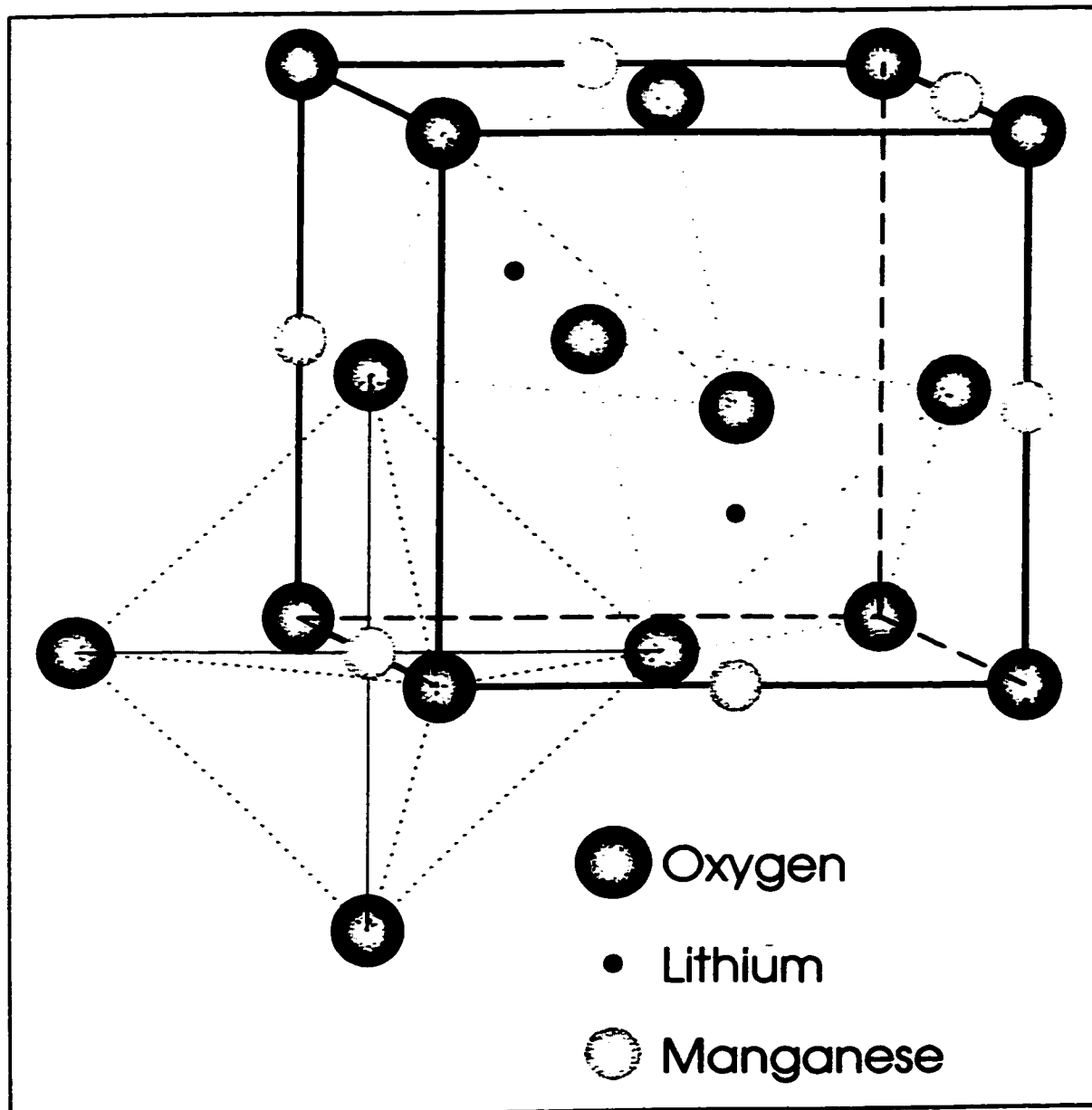
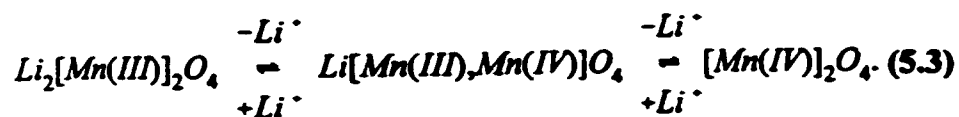
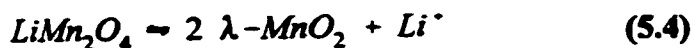


Figure 5.2: One eighth of a unit cell of the LiMn_2O_4 spinel. The manganese atoms are shown to occupy octahedral sites while the lithia occupy tetrahedral sites.

To maintain charge neutrality during lithium insertion/extraction, the manganese atoms must undergo reduction/oxidation. This is easily depicted by the following equilibrium expression:



The $[\text{Mn(IV)}]_2\text{O}_4$ represents the λ - MnO_2 phase which may also be given as $[\]^{\text{Mn}}\text{Mn}_2\text{O}_4$. This indicates that the material has maintained its predominantly spinel character though the tetrahedral sites are now vacant. Neutron diffraction studies by Thackeray *et. al.* of the process:



have confirmed the persistence of a perturbed spinel phase with a slightly reduced unit cell size corresponding to the extraction of lithium. The small degree of structural change of the material during lithium insertion/extraction has made it a strong candidate for rechargeable lithium batteries at 4V.

The insertion of a second lithium ion into the LiMn_2O_4 spinel occurs at about 2.8V and causes a Jahn-Teller distortion in the lattice structure [79]. This distortion leads to a change from the cubic lattice to a tetragonal lattice structure. The conversion to a tetragonal structure is not entirely reversible, and is thought to be a significant cause of failure in the cathode performance in lithium cells. Consequently, battery applications using the spinel form of manganese dioxide are best suited to use at the upper voltage plateau region, namely from about 4.2 volts to 3.5 volts.

5.2 Cathode Film Preparation

The thin film cathodes were prepared by the magnetron sputtering technique. The sputter sources used for cathode film deposition were the commercially available Mini MAK™ 1.3 inch diameter sputter guns from US Thin Film Products Inc. These sputter sources were compatible with both DC and RF power supplies, capable of 250 watts maximum DC power or 150 watts RF power. The RF power was particularly useful when depositing the lithiated manganese oxide material.

Many pure elemental targets as well as some alloys are readily available from suppliers, but the LiMn_2O_4 targets were fashioned from the pure spinel phase LiMn_2O_4 material prepared by a solid state reaction between LiOH and MnO_2 at 750°C under oxygen atmosphere for twelve hours. Approximately 45mg of poly-ethylene glycol (PEG) was added to 9g of the LiMn_2O_4 , and this was thoroughly ground by mortar and pestle to give an homogeneous mixture which was placed into a 1.25 inch diameter stainless steel die to be hot pressed to 25 tons at 200°C for two hours. The pressure was maintained during the slow cooling until room temperature was attained. The PEG acted as a binder for the target formation; the 0.5 wt% was determined to be the minimum amount that could be added that gave good results.

The newly produced targets were sintered in an oven at 750°C under oxygen atmosphere for 6 h. The PEG was believed to have entirely burned off after this stage leaving only the sintered target containing only the pure spinel LiMn_2O_4 material.

Initially, the 1cm diameter magnetic keeper used to hold the target in place on the sputter gun was affixed directly to the target by application of high vacuum epoxy (Duralco 4525). While the epoxy seemed to hold well enough under vacuum and during sputtering, but the targets were brittle and often broke during installation or removal. Later, a copper disc 1.3 inches in diameter was used to provide extra mechanical strength; there was also the added benefit of improved thermal contact to the cooling jacket. The copper disc was attached to the backside of the target by the same high vacuum epoxy. The epoxy proved not to bind the copper to the magnetic keeper well enough, so silver solder was used to affix the keeper to the copper disc.

Despite having the desired stoichiometric ratios of lithium, manganese, and oxygen in the target, it was determined that if only pure argon gas was used during sputtering, the films being deposited would be oxygen deficient. This was likely due to fractionation of the target material under the harsh conditions needed for sputter deposition. This fractionation of the target material was witnessed by the x-ray diffraction pattern shown in Figure 5.3 of the target after removal from the vacuum chamber. The diffraction pattern indicates that the material has become multi phasic, in

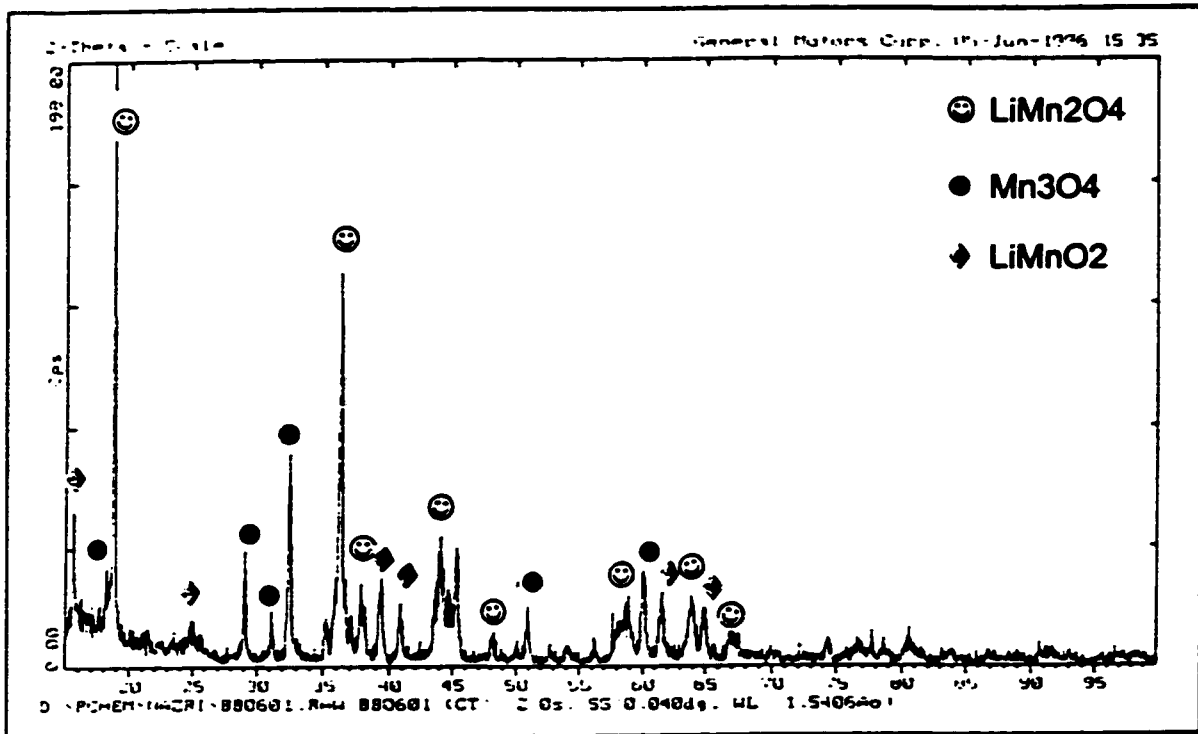


Figure 5.3: The x-ray diffraction pattern of the target material after sputter deposition.

particular the target now consists of a mixture of the LiMn_2O_4 spinel and manganese rich phases such as Mn_3O_4 and LiMnO_2 . Annealing of the residual target material at 750°C under oxygen returned the pure spinel starting material as seen in the diffraction pattern in Figure 5.4.

The oxygen deficiency of the films was confirmed by ESCA and sputter depth profile analyses. Ratios as low as 1:1 for manganese to oxygen were observed. Consequently, oxygen was seeded into the argon gas to a partial pressure of approximately 0.1 mTorr; the total pressure during deposition was typically around 6 mTorr. These conditions were similar to those used by Bates *et al.* [77] and increased the oxygen concentration in the films.

The RF-sputtering technique was used to eliminate the problem of charge buildup on the target surface that can occur during DC-sputtering. The power applied was typically 100 W resulting in a deposition rate of $8\text{-}10 \text{ \AA min}^{-1}$ as monitored by the quartz crystal oscillator.

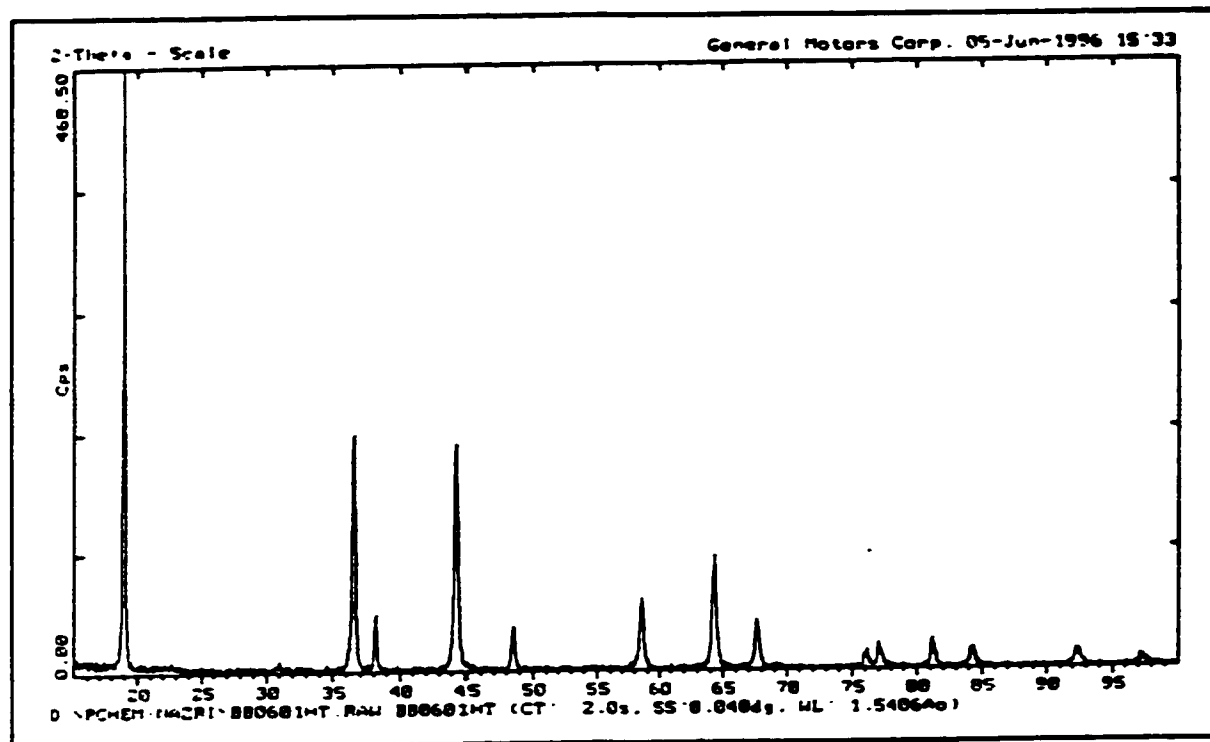


Figure 5.4: The x-ray diffraction pattern of the target material as shown in Figure 5.3 after reaction in oxygen atmosphere at 750 °C.

5.3 Characterization of the Cathode Thin Films

The techniques used to the lithiated manganese oxides films were: grazing angle x-ray diffraction, Fourier transform infrared spectroscopy, and Raman spectroscopy. The results from each of these techniques were compared with those of the bulk materials.

5.3.1 Grazing Angle X-ray Diffraction

In conventional x-ray diffraction experiments, both the source and detectors are swept through the θ degrees to give a 2θ diffraction pattern. For thin films samples, insufficient layers of atoms are present to give adequate diffraction patterns, and interference from the substrate diffraction pattern is an additional problem. The grazing

angle technique holds the source fixed at an acute angle to the sample, typically one degree, and the detector is swept through the 2θ degrees. Artifacts from this technique include slight shifting of peak positions and changes in the relative intensities of the peaks. The magnitude of the shift in d-spacing will decrease at smaller absolute d-spacing (larger values of 2θ), so the comparison to tabulated diffraction patterns is straightforward.

The grazing angle diffraction pattern of a 165 nm film deposited on a silicon wafer is given in Figure 5.5. The broadness of the peaks is indicative of a low degree of

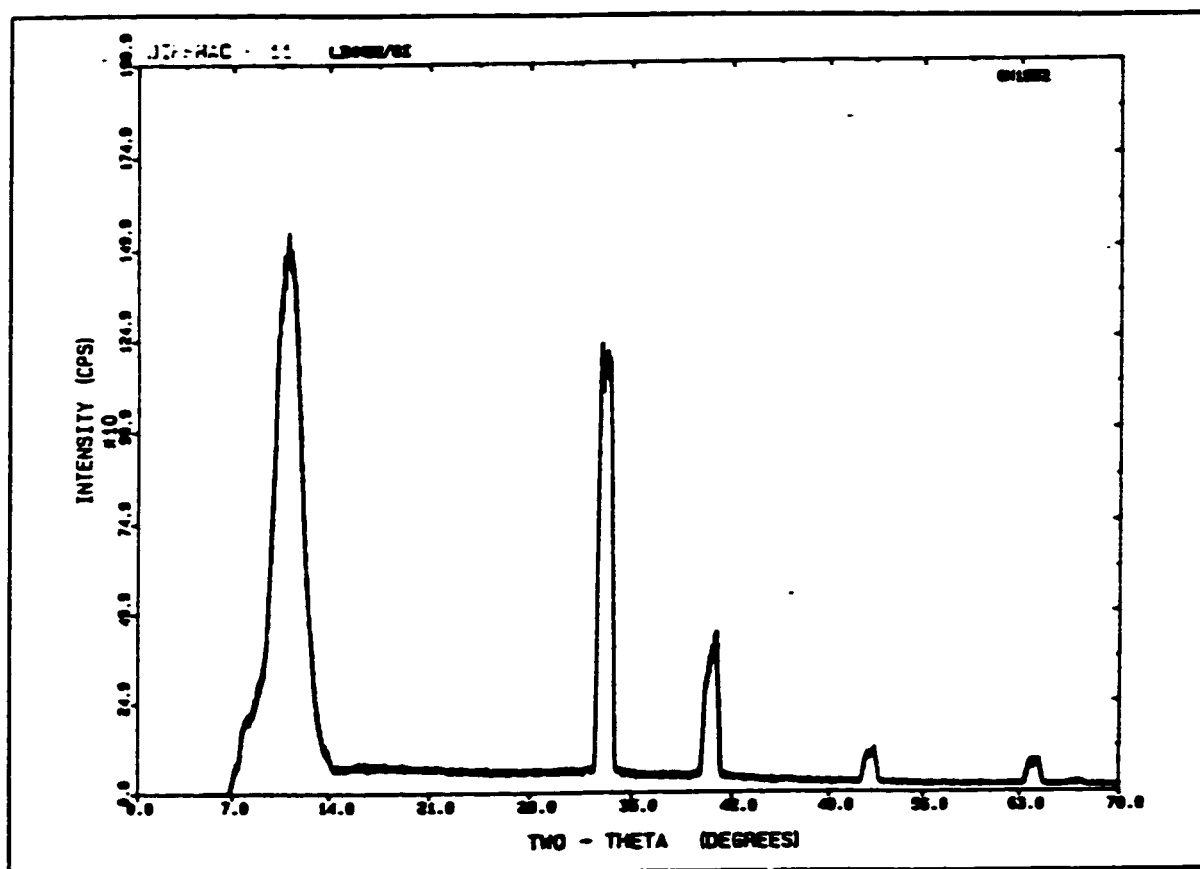


Figure 5.5: The grazing angle x-ray diffraction pattern for a 165 nm Li-Mn-O film deposited on a silicon wafer.

crystallinity and the peak positions suggest that the film was a polycrystalline mixture of multiple phases of lithiated manganese oxide. The pattern most closely resembles the Mn_3O_4 spinel phase [80]. Hausmannite is a manganese rich spinel as compared to

LiMn_2O_4 , and is likely to consist of $[\text{Mn}^{2+}]^{\text{tet}}[\text{Mn}_2^{3+}]^{\text{oct}}\text{O}_4$. The manganese:oxygen atom ratio of roughly 3:4 was verified by ESCA.

5.3.2 Infrared and Raman Spectroscopy

The complementary techniques of infrared and Raman spectroscopies were used as diagnostic tools for the characterization of the Li-Mn-O films. The film spectra were compared to those of the pure LiMn_2O_4 spinel material as well as several other pure manganese oxide samples. Much work has been done in the mode analyses of spinel-type materials [81-85]; these compounds have the space group $Fd3m(O_h^7)$ and the irreducible representation of the vibrational modes is given by:

$$\Gamma = A_{1g} + E_g + T_{1g} + 3T_{2g} + 2A_{2u} + 2E_u + 5T_{1u} + 2T_{2u}. \quad (5.5)$$

By group theory, one of the T_{1u} modes represents the translational modes while the other four are infrared active. The A_{1g} , E_g , and T_{2g} modes are all Raman active.

The FTIR spectrum of the film deposited on silicon is shown in Figure 5.6. The signal intensity proved to be quite weak, only the highest frequency mode was observed before the silicon cut-off was encountered. The peak correlates well with the highest frequency infrared active mode of the pure LiMn_2O_4 spinel [85], the mid-IR spectrum of the dispersed powder in KBr is shown for comparison.

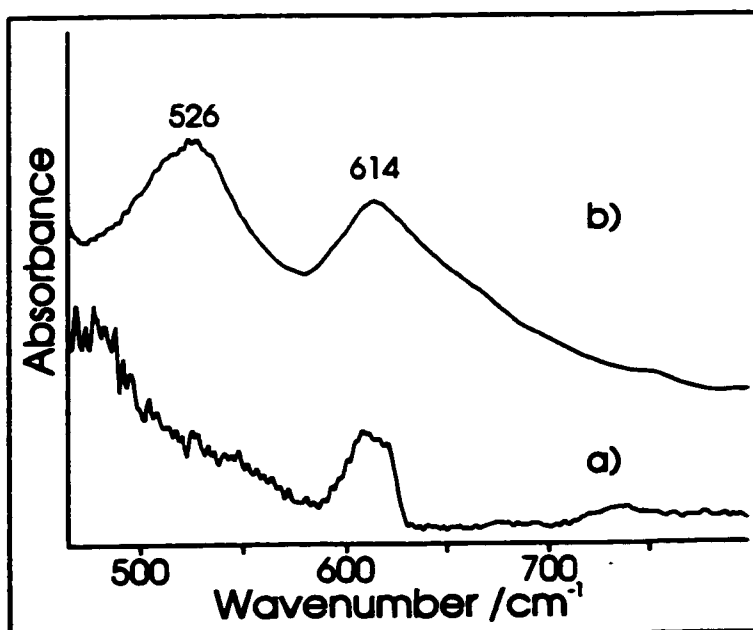


Figure 5.6: The FTIR spectra of: (a) a 165 nm film of Li-Mn-O on silicon, and (b) the pure powder of LiMn_2O_4 spinel phase.

The Raman spectrum of the pure spinel material is shown in Figure 5.7. The broad blended peaks were resolved by deconvolution using the curve fitting subroutines provided with SpectraCalc software. The results of the fitting are overlaid onto the spectrum and are tabulated in Table 5.1.

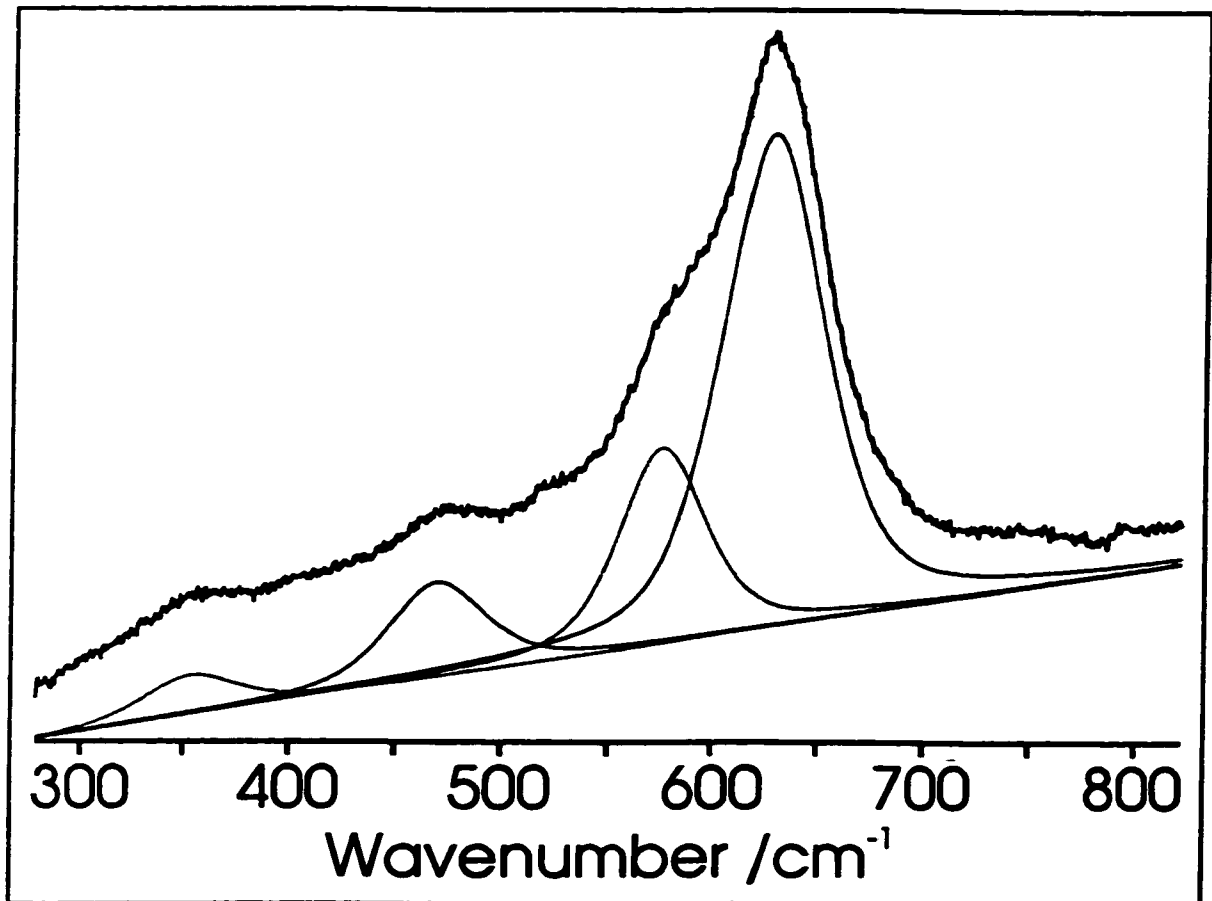


Figure 5.7: The Raman spectrum of LiMn₂O₄ powder. Superimposed on the spectrum are the results from a curve-fitting routine.

The Raman spectra of a Li-Mn-O film on a silicon wafer were dominated by the extremely intense silicon peak at 520 cm⁻¹. Spectra were recorded away from the silicon peak to bring out the details of the film peaks. These spectra are shown in Figure 5.8, a number of peaks were clearly evident.

Table 5.1: The list of Raman frequencies and relative intensities of the pure LiMn_2O_4 spinel powder and the Li-Mn-O film on silicon substrate as determined by curve fitting. The symmetry assignments are for the pure spinel [82-84].

Li-Mn-O Film on Si		LiMn ₂ O ₄ powder		Symmetry Assignment
Raman Shift /cm ⁻¹	Relative Intensity	Raman Shift /cm ⁻¹	Relative Intensity	
302	46.6			
338	19.0			
–		353	7.2	e _g
434	15.5			
–		470	18.3	t _{2g}
582	8.7	576	34.3	t _{2g}
625	90.9	628	100.	a _{1g}
667	29.3	–		–
699	100.	–		–

Application of a curve fitting routine to frequencies lower than the silicon line resolved four peaks as illustrated in Figure 5.8(a). The region to higher frequency was similarly analysed and is illustrated in Figure 5.8(b). The results of the curve fitting routines were also tabulated in Table 5.1. Two of the peaks of the Li-Mn-O film correlate with those of the pure spinel, which suggests that the material was either related to the LiMn_2O_4 compound or that the film was polycrystalline and one of the phases present was indeed the LiMn_2O_4 spinel phase. The very intense peak at 699 cm⁻¹ could not be attributed to the spinel. Raman peaks for a series of different manganese oxide powders are given in Table 5.2. A comparison of the Raman spectra of this MnO_x series with the Li-Mn-O film spectrum (Table 5.1) indicates that none of the stable forms of MnO_x were present in the Li-Mn-O film. Either a new phase or a mixture of phases of Li-Mn-O has been formed.

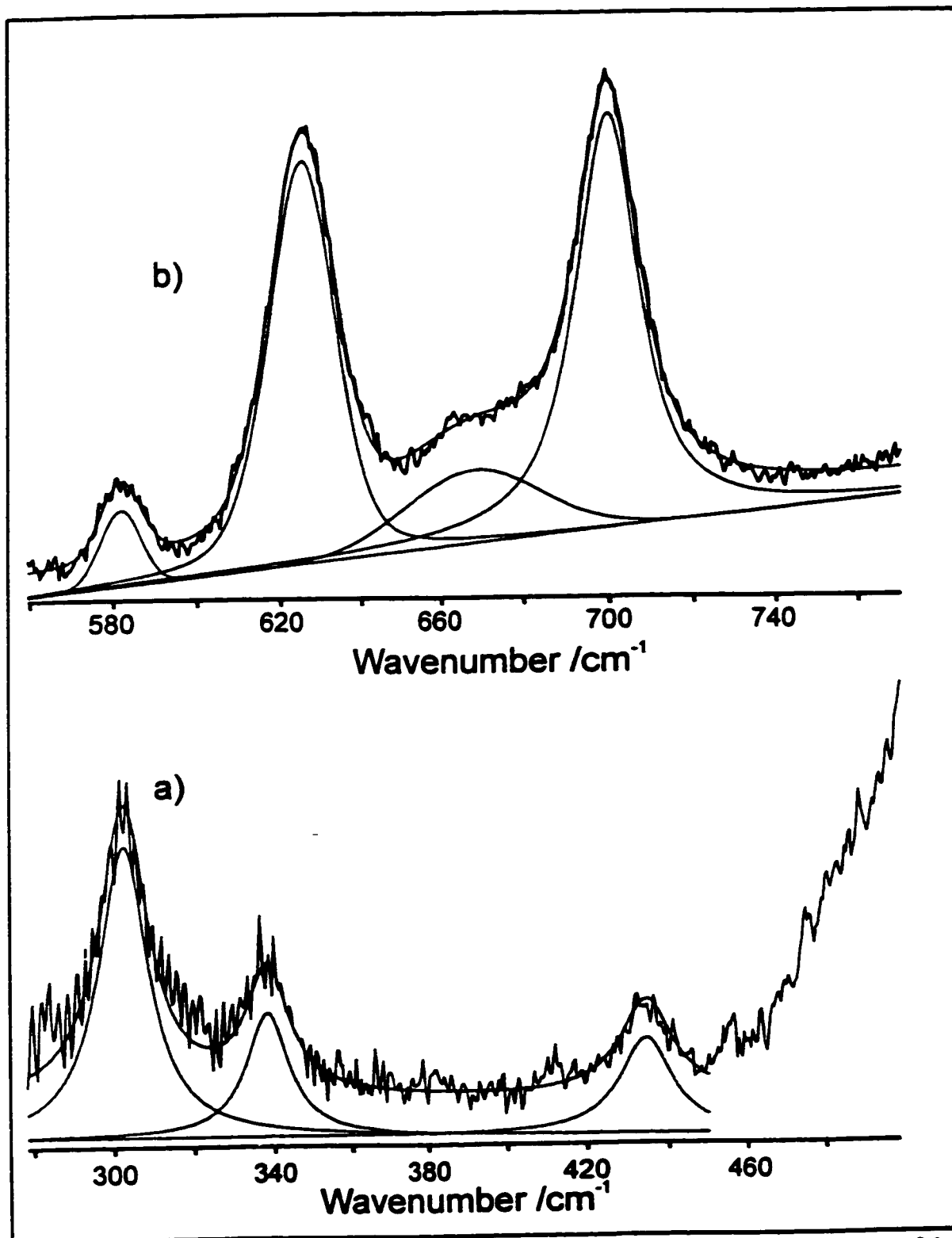


Figure 5.8: The Raman spectra of an Li-Mn-O film: (a) to the low frequency side of the silicon line, and (b) to the high frequency side. The results of curve-fitting are superimposed on the spectra.

Table 5.2: Tabulated Raman peaks for a variety of manganese oxide materials.

$\text{MnO}_2^{\&}/\text{cm}^{-1}$	$\text{MnO}_2^{\circ}/\text{cm}^{-1}$	$\text{MnO}_2^{\textcircled{R}}/\text{cm}^{-1}$	$\gamma\text{-Mn}_2\text{O}_3/\text{cm}^{-1}$	$\text{LiMn}_2\text{O}_8/\text{cm}^{-1}$
-	-	-	-	288.
-	-	-	311.	317.
-	-	-	347.	373.
517.	525.	505.	488.	477.
539.	574.	557.	590.	565.
-	627.	637.	-	-
669.	646.	-	644.	658.
-	-	-	695.	-
-	749.	750.	751.	761.

[°] - chemically prepared sample

[Ⓜ] - electrochemically prepared sample from France.

[&] - electrochemically prepared sample, pH 1, 20 °C

5.4 Electrochemical Analyses of the Li-Mn-O Film

The fabricated films were used for charge/discharge capacitance studies. Films were deposited onto aluminum foil substrates that had been pretreated by plasma cleaning to remove the aluminum oxide layer; the aluminum foil would act as a current collector and was much easier to cut to fit the cycling cell than silicon wafer substrates.

5.4.1 The Electrochemical Cell

A sketch of the electrochemical cell is shown in Figure 5.9, the same cell design used by Verbrugge and Koch [87]. Due to the highly reactive nature of the anode and electrolyte solution when exposed to water or oxygen, the cell was assembled under an inert atmosphere in a dry box containing less than 1 ppm oxygen and moisture. The cell

consisted of nickel current collectors for the anode and cathode, lithium foil as the anode, a non-aqueous electrolyte, a lithium-aluminum alloy wire as the reference electrode, and the Li-Mn-O film on aluminum foil as the cathode. Clamps were used to apply even pressure over the cell from each end to ensure a good seal between each of the components. The area of the electrodes that were exposed to the electrolyte solution was approximately 0.601 square inches (3.88 cm²), corresponding to a 0.875" diameter disk.

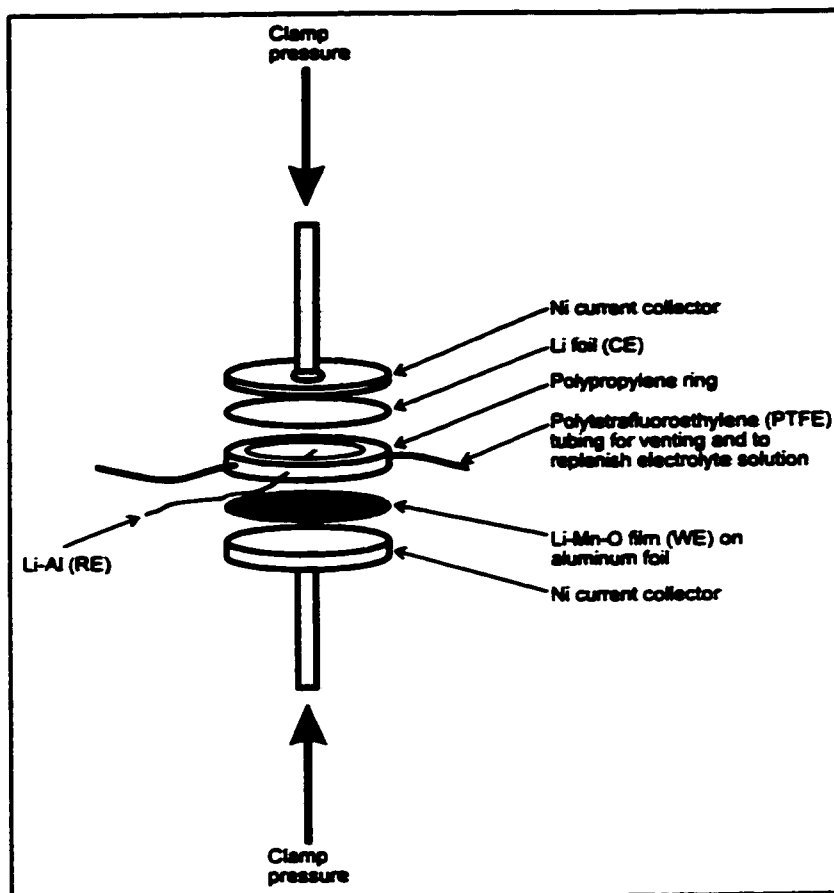


Figure 5.9: A sketch of the electrochemical cell, after Verbrugge and Koch [87].

The electrolyte solution was 0.8 M LiPF₆ in a 50v% mixture of ethylene carbonate and diethyl carbonate (EC:DEC). This solvent mixture was stable under the voltage range used for these experiments and was capable of providing sufficient lithium ion conduction. The solution was introduced by syringe through a polytetrafluoroethylene (PTFE) tube; the tubing permitted the solution to be replenished as well as a vent for gasses produced during the cycling experiments. The surface of the lithium foil was scrapped by a clean plastic utensil to remove any oxide layer that may have formed.

5.4.2 Charge-Discharge Cycling

The mass of active cathode material was determined from a calculation based upon the film thickness and the cross-sectional area of the electrode surface. It was estimated that the density of the film material would equal approximately $4.19 \text{ g}\cdot\text{cm}^{-3}$, the bulk density of LiMn_2O_4 . Thus, for a film of 200 nm thickness, the mass would represent 325 μg of material. This value has been found to be low [77], but serves as a reasonable estimate. Unless otherwise noted, all cycling experiments were conducted under a constant current of $9.7 \mu\text{A}\cdot\text{cm}^{-2}$.

A measure of battery performance involves the determination of the total capacity of the cell. This capacity is often reported in terms of the charge per unit mass of material and often take the units of $\text{mA}\cdot\text{h}\cdot\text{g}^{-1}$.

The cells were cycled initially over a voltage range from 3.50V to an upper limit of 4.20V over ten cycles. The voltage range was then expanded to 3.00V as the lower limit and ten more charge-discharge cycles were performed. These steps were repeated until ultimately of potential range from 1.80V to 5.00V was utilized for the charge/discharge cycling experiments. An illustration of the cell capacity as a function of the voltage range is shown in Figure 5.10. Clearly, the capacity of the cell increased markedly when the wider

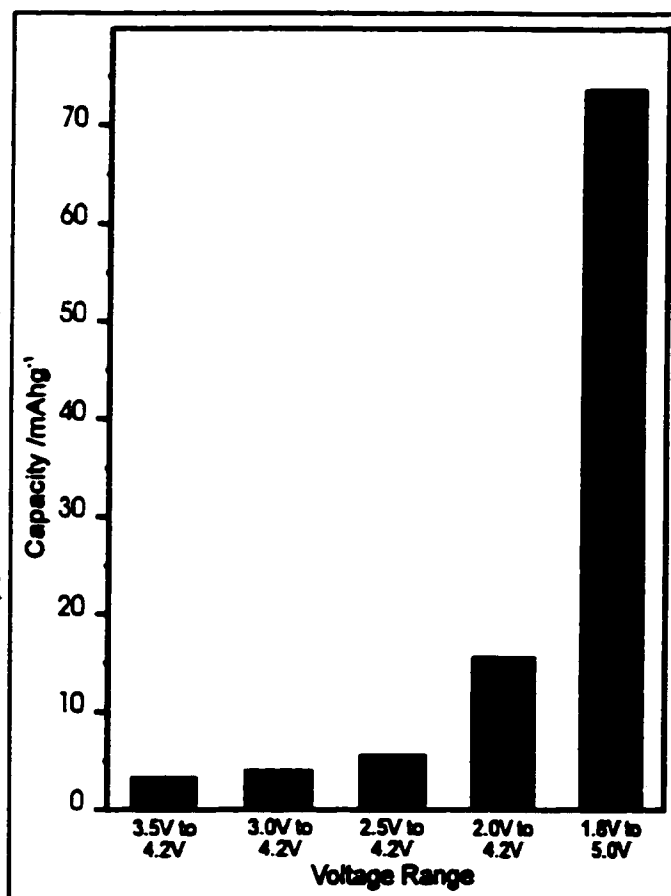


Figure 5.10: A graph showing the charge capacity variation over a number of charge-discharge voltage ranges.

voltage limits were utilized. In all cases, large internal resistance (IR) drops of the order of 0.5V was typical. Such obtrusive impedances would account for the greatly reduced capacities in the films over each of the voltage ranges, and in particular for the narrower ranges.

For the final voltage range of 1.80 to 5.00 V, the electrochemical cell was continuously cycled for up to 66 cycles. The results of several of the charge/discharge cycles are plotted in Figure 5.11. Over this range, the initial capacity of the cell was determined to be 78.9 mA h g^{-1} , approximately one half of the theoretical value of 154 mA h g^{-1} for the LiMn_2O_4 system over the same range [86]. The capacity dropped off fairly quickly, but after about twenty cycles stabilized around 61 mA h g^{-1} as indicated in Figure 5.12. Part of the capacity decline was due to the apparent increased impedance in the cell. The IR drop increased to approximately 1.0V at higher cycles.

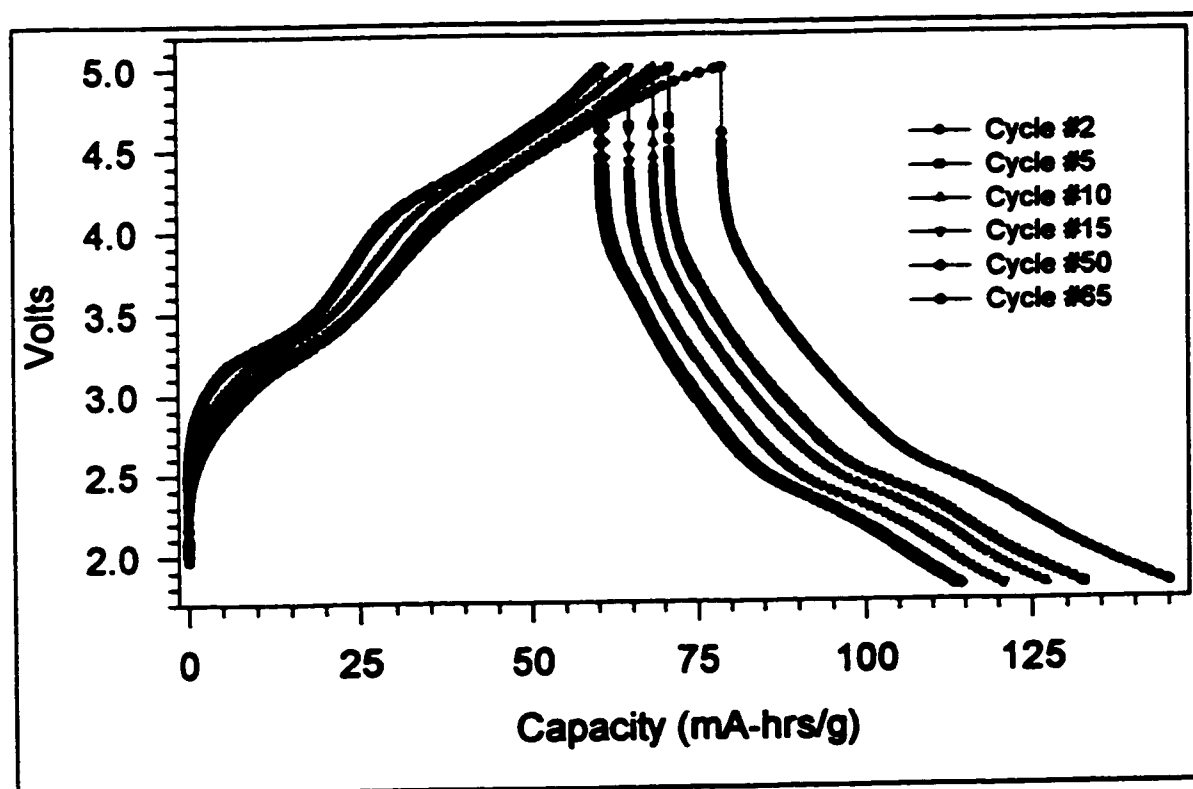


Figure 5.11: The charge:discharge capacity of a 200 nm Li-Mn-O film over a number of cycles.

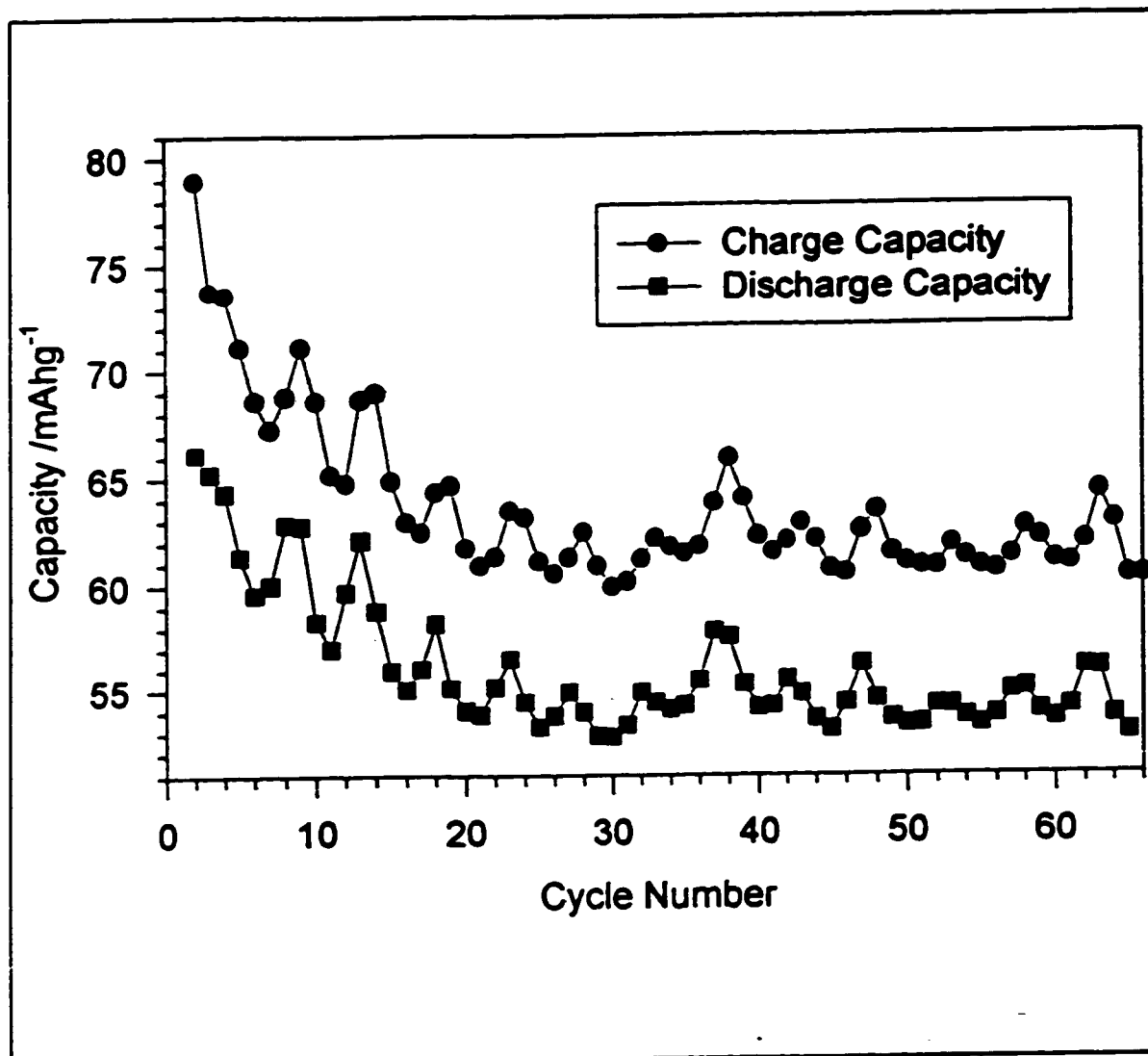


Figure 5.12: Plot of the specific charge capacity of the 200 nm Li-Mn-O film during charge and discharge cycles as a function of cycle number.

An encouraging sign from the cycling experiments with this cell was the onset of better defined plateaus at around 3.3V and 4.2V during charging. The repeated insertion and removal of the lithium in the mixed phase film caused the conversion of some of the film material into a spinel.

5.4.3 The Ratio of Charge:Discharge Capacity

The ratio of the charge:discharge capacity as a function of cycle number (Figure 5.13) demonstrates the ability of these Li-Mn-O film cathodes to retain charge and deliver the stored energy efficiently and completely. Under ideal conditions, one would hope to attain a steady ratio of one, meaning that all of the energy put into the cell can be removed from the cell. After the initial cycle, this cell shows clearly an ability to

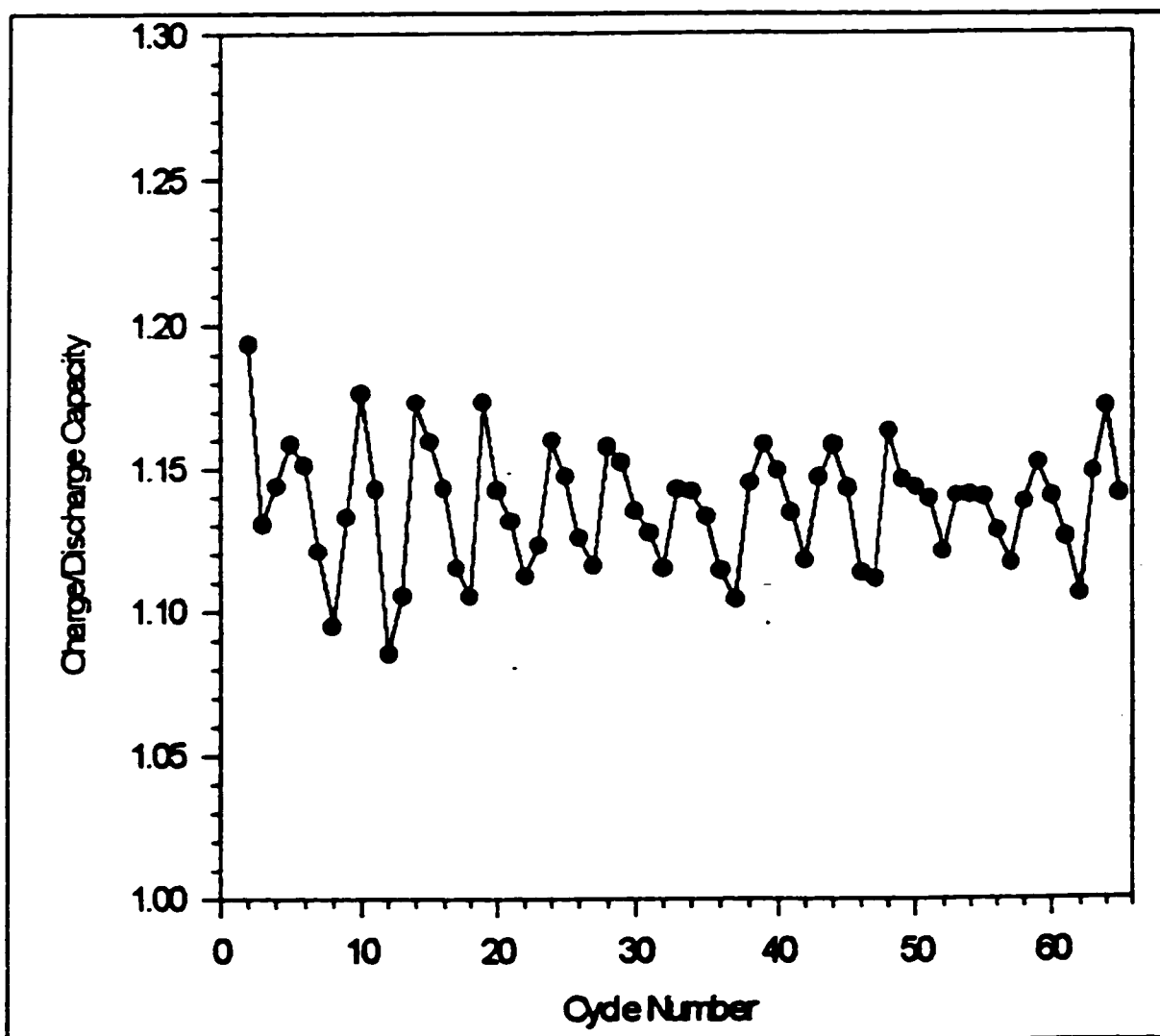


Figure 5.13: The charge:discharge capacity ratio as a function of cycle number for the film shown in Figures 5.11 and 5.12.

obtain ratios close to 1.16. The deviation for unity as well as the fluctuations in the data were likely due to solvent decomposition.

5.4.4 Impedance Analysis of the Cell

As indicated, these cells exhibited voltage drops between 0.5 volts and 1.0 volts. These drops were likely due to a high degree of polarization at the interface between the Li-Mn-O films and the aluminum substrates. Impedance measurements were made for one of these cells when the cell was partially charged ($E=3.05$ V vs Li/Li⁺). The results for a film deposited onto aluminum foil substrate at 400 °C are shown in Figure 5.14

and Figure 5.15; the plot of the real ($Z'(\Omega)$) versus the imaginary ($Z''(\Omega)$) impedance (Figure 5.14) very clearly shows the onset of a high degree of polarization very early on. This effect was not overcome until the real impedance approached 15000 Ω .

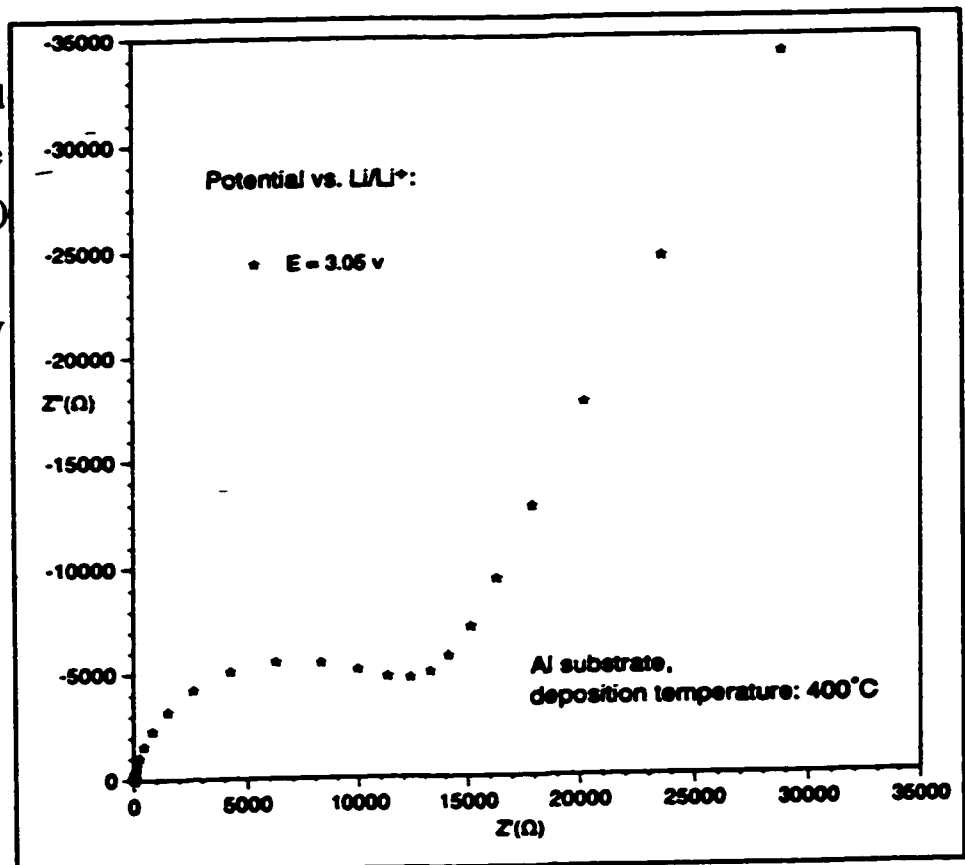


Figure 5.14: Plot of the impedance measurements for a 200 nm Li-Mn-O film on aluminum.

While a noble metal substrate such as gold would have likely alleviated this difficulty, the cost was prohibitive. Instead of a pure metal substrate, it was proposed that a thin film of gold deposited upon the plasma cleaned aluminum foil may reduce the impedance problems at the interface without increasing the cost too greatly. Hence, 200 nm films of gold were

deposited onto both sides of aluminum foil substrates.

When the substrates were heated in preparation for Li-Mn-O film deposition, however, it was clearly evident from a viewport on the sputter deposition chamber that something unexpected was happening to the gold film as it was turning an odd shade of purple. The gold was rapidly diffusing into the aluminum, a phenomenon that had been well characterized [88, 89]. Despite the formation of Al-Au alloys, it was not expected

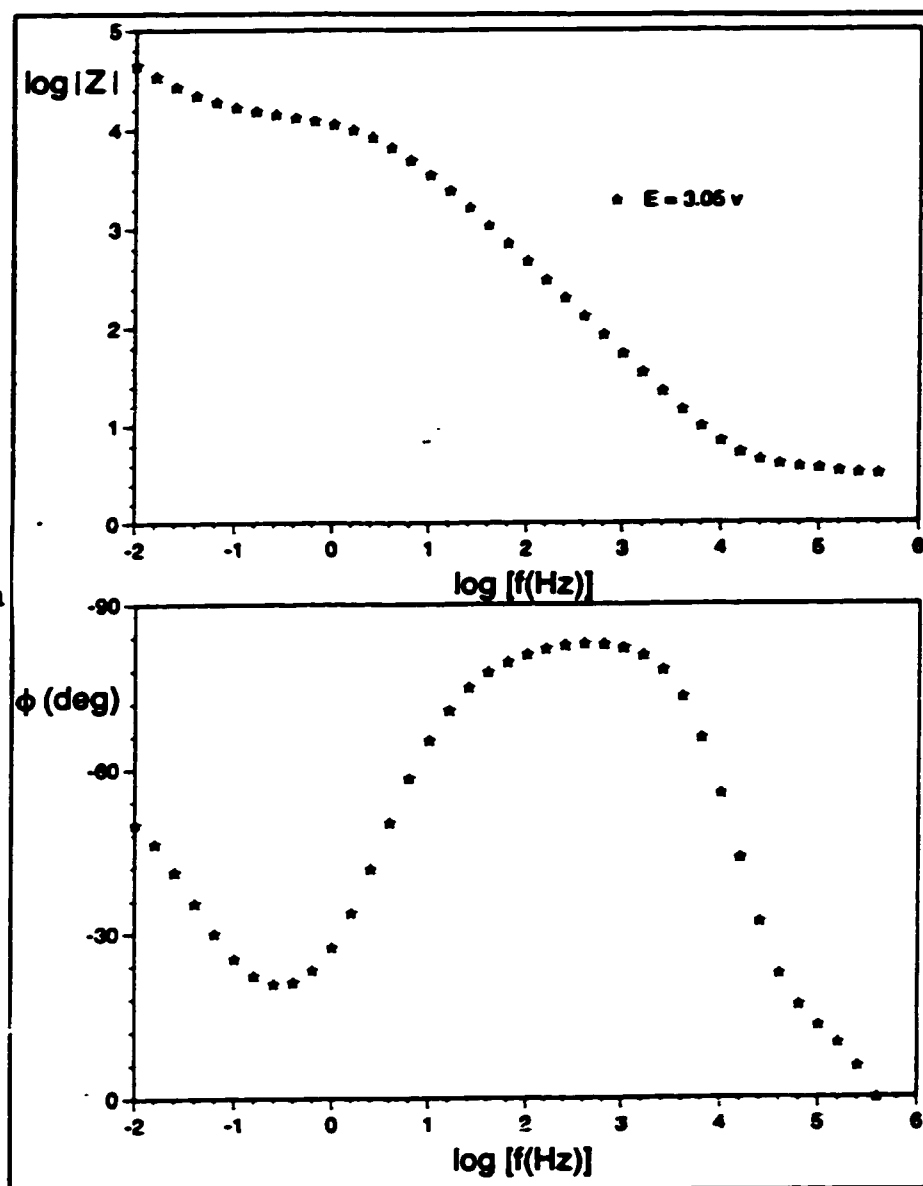


Figure 5.15: Plot of the frequency dependent impedance measurements for a 200 nm Li-Mn-O film on aluminum.

that the alloys would pose a problem for the cells. The alloys themselves were metallic, and the gold should inhibit the formation of the aluminum oxide layer that was likely the major source of polarization in the cell during the charge/discharge cycles.

The impedance results for a 200 nm Li-Mn-O film deposited onto the Al-Au alloy film are given in Figure 5.16 for two different cell potentials. This cell clearly shows a much reduced level of polarization than was observed for the films deposited onto pure aluminum. The performance for films deposited onto this substrate would therefore be expected to give higher capacity than otherwise similar films deposited onto the pure aluminum foils.

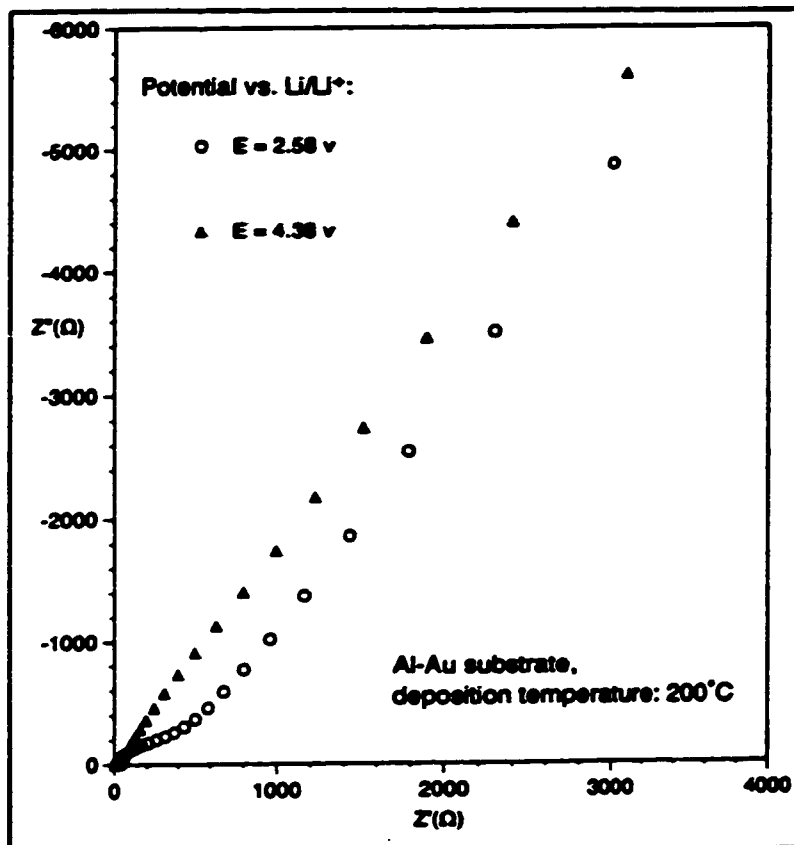


Figure 5.16: The impedance measurements for a 200 nm Li-Mn-O film on gold-aluminum alloy.

The capacity of the Li-Mn-O films deposited onto the Au-Al alloy has indeed increased markedly as compared to the films deposited on pure aluminum. This fact is clearly seen in Figure 5.17 where the charge capacity was 211 mAhg⁻¹. While a higher than normal capacity was expected due to the estimation of the mass of the film [77], this level of current capacity was quite astounding. Even after ten cycles (see Figure 5.18), the current capacity was still greater than the theoretical value of 154 mAhg⁻¹ for the LiMn₂O₄ spinel.

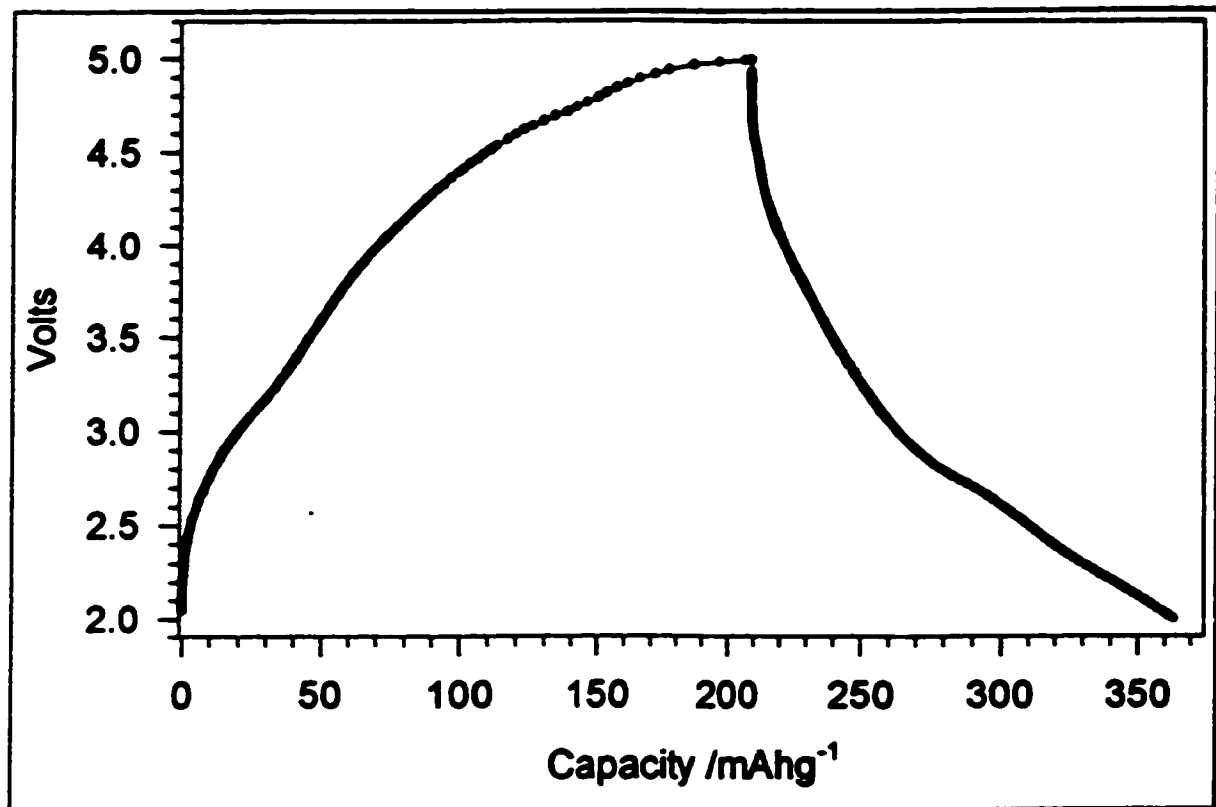


Figure 5.17: The charge:discharge capacity of a 200nm Li-Mn-O film deposited on the gold-aluminum alloy substrate.

5.5 Conclusions

Thin films of Li-Mn-O were prepared by the radio frequency magnetron sputter deposition technique on sintered targets of the pure LiMn_2O_4 spinel material. The infrared and Raman spectroscopy of the films on silicon determined that the films consisted of a mixture of multiple phases of Li-Mn-O. The grazing angle x-ray diffraction pattern suggested a structure similar to the Mn_3O_4 , in agreement with ESCA analyses that indicated the Mn:O ratio in the films was 3:4.

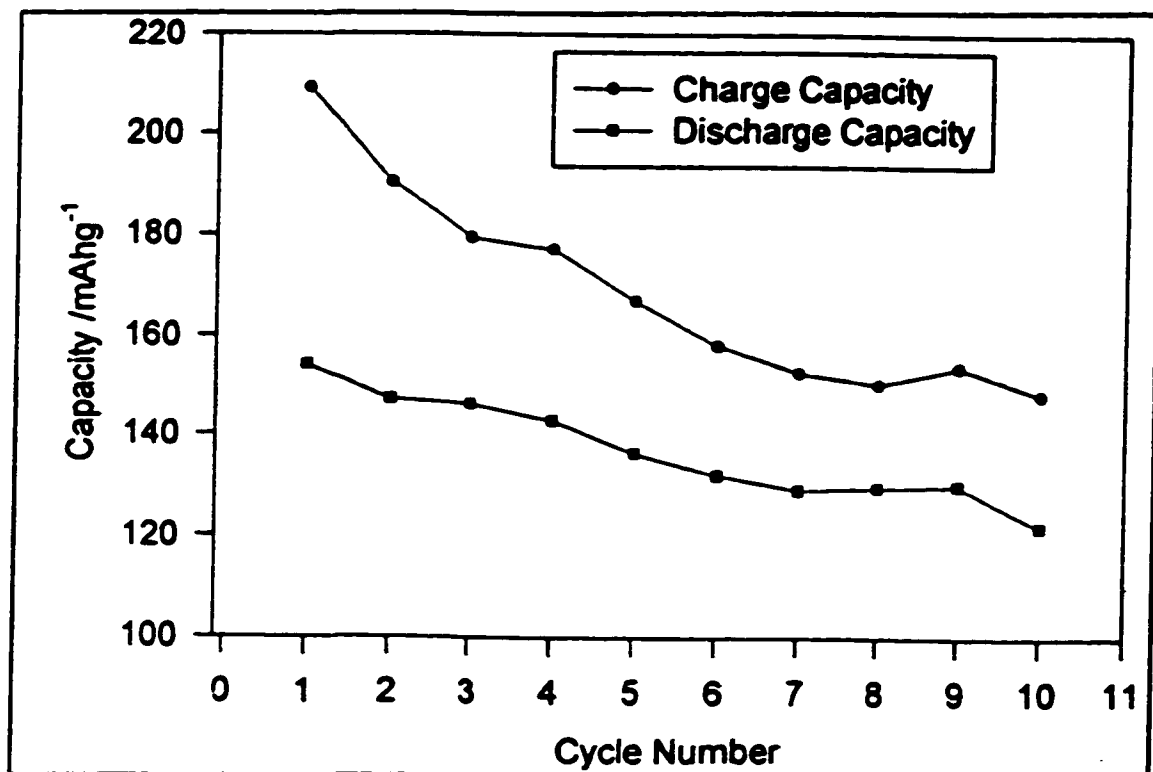


Figure 5.18: Plot of the specific charge capacity of a 200 nm Li-Mn-O film on a gold-aluminum alloy substrate.

Charge-discharge cycling experiments were performed on the Li-Mn-O films deposited on aluminum foils as well as gold-aluminum alloys. The capacity of the films on aluminum was initially 78.9 mAhg⁻¹ over the voltage range of 1.8V to 5.0V, dropping to 61 mAhg⁻¹ after about twenty cycles. The capacity was limited by the very large impedance between the Li-Mn-O cathode film and the aluminum substrate. The capacity of the films deposited onto the gold-aluminum alloy was greatly improved over that of the films on aluminum. The improved performance of the alloy was due to the much lower impedance in the cell.

Chapter 6: Summary

*“... and I swear it happened just like this:
a sigh, a cry, a hungry kiss...
it's CLOSING TIME”*

From *Closing Time*, by Leonard Cohen.

This thesis has served to describe the preparation, characterization, and application of two distinct devices. One device consisted of Langmuir-Blodgett monolayers of europium bisphthalocyanine (EuPc_2) that were utilized in an NO_2 gas sensor. A thin film lithium microbattery was the second device. Films of Li-Mn-O prepared by reactive magnetron sputter deposition constituted the cathode of the microbattery.

Floating monolayers of EuPc_2 were prepared on a Langmuir trough, and LB films were transferred onto glass slides, ZnS crystals, and interdigitated electrodes. The LB films were probed using transmission infrared spectroscopy showed a nearly flat-on orientation of the molecules and no anisotropy in the dipping direction.

Near infrared charge transfer transitions of an LB film, of a LnPc_2 compound, are reported here for the first time. The distinct Raman intensity patterns obtained in resonance with the Q-band (647.1 nm) and with the 488 and 514.5 nm laser lines are discussed in terms of the vibronic approach. The surface-enhanced Raman spectra of EuPc_2 LB films on metal island films including the FT-SERS of a single monolayer of EuPc_2 were also recorded. The conclusion from the SERS data was that the EuPc_2 molecules are physisorbed onto silver and gold. However, the relative intensity of several normal modes indicates the presence of a predominantly flat-on molecular orientation of the monolayer on the metal island film. The assignment of characteristic vibrational frequencies are given.

In experiments where Langmuir-Blodgett monolayer films of EuPc_2 were applied as NO_2 gas sensors, their response was first measured spectroscopically using UV-visible absorption and SERRS spectroscopies. From the spectroscopic data it was determined that the effects of gas exposure on the LB films were dramatic and reversible.

The effects on the electrical conductivity of the films due to gas exposure were also dramatic. The change in the electric conductivity of the films due to NO_2 exposure was easily detectable for concentrations as low as 2.1 ppm NO_2 in nitrogen. The electrical did not however prove to be reversible as it was necessary to heat the sensor under vacuum to completely recover the film. Preliminary EPR experiments to study the effects of NO_2 exposure on LnPc_2 complexes suggested a completely irreversible transformation had occurred.

One avenue that should obviously be explored by future researchers would involve a more complete analysis using EPR to probe the interactions between these two paramagnetic complexes. Another interesting set of experiments would involve testing the response of these LB films to other gases such as carbon monoxide (CO), nitrogen monoxide (NO), oxygen (O_2), and ozone (O_3).

For the lithium based microbattery project, thin films of Li-Mn-O were prepared by the radio frequency magnetron sputter deposition technique of sintered targets of the pure LiMn_2O_4 spinel material. The infrared and Raman spectroscopy of the films on silicon determined that the films consisted of a mixture of multiple phases of Li-Mn-O. The grazing angle x-ray diffraction pattern suggested a structure similar to the Mn_3O_4 , in agreement with XPS analyses that indicated the Mn:O ratio in the films was 3:4.

Charge-discharge cycling experiments were performed on the Li-Mn-O films deposited on aluminum foils as well as gold-aluminum alloys. The capacity of the films on aluminum was initially 78.9 mA h g^{-1} over the voltage range of 1.8 to 5.0 V, dropping to 61 mA h g^{-1} after about twenty cycles. The capacity was limited by the very large impedance between the Li-Mn-O cathode film and the aluminum substrate. The capacity of the films deposited onto the gold-aluminum alloy was greatly improved over

that of the films on aluminum. The improved performance of the alloy was due to the much lower impedance in the cell.

Clearly, there is much work that could be done involving the substrate preparation. The greatly enhanced performance of the film deposited on the gold-aluminum alloy shows great promise for inexpensive electrical storage devices. Also, more work should be done in the various deposition conditions to improve the crystallinity and homogeneity of the Li-Mn-O films.

References

1. R.P. Feynman, *Eng. And Sci.*, **23**, 22 (1960).
2. K.E. Drexler, *Nanosystems: Molecular Machinery, Manufacturing, and Computation*, John Wiley and Sons, Inc., New York (1992).
3. K.E. Drexler, *Science*, **255**, 268 (1992).
4. E. Regis, *Nano!*, Little,Brown, Boston (1995).
5. D. Tabor, *J. Colloid Interface Sci.*, **75**, 240 (1980).
6. L. Rayleigh, *Proc. R. Soc. London*, **47**, 364 (1890).
7. A. Pockels, *Nature*, **43**, 437 (1891).
8. L. Rayleigh, *Philos. Mag.*, **48**, 321 (1899).
9. I. Langmuir, *J. Am. Chem. Soc.*, **39**, 1848 (1917).
10. K.B. Blodgett, *J. Am. Chem. Soc.*, **57**, 1007 (1935).
11. A. Braun and J. Tcherniac, *Ber. Deut. Chem. Ges.*, **40**, 2709 (1907).
12. *Phthalocyanines: Properties and Applications*, vol. 1-3, C.C. Leznoff and A.B.P. Lever, Eds; VCH Publishers, Inc., New York (1989-1993).
13. *The Phthalocyanines*, A.L. Moser, Ed; CRC Press Inc., Boca Raton, FL (1990).
14. J.S. Shirk, J.R. Lindle, F.J. Bartoli, and M.E. Boyle, *J. Phys. Chem.*, **96**, 5847 (1992).
15. S. Baker, M.C. Petty, G.G. Roberts, and M.V. Twigg, *Thin Solid Films*, **99**, 53 (1983).
16. I.S. Kirin, P.N. Moskalev, and Yu. A. Makashev, *Russ. J. Inorg. Chem. (Engl. Transl.)*, **10**, 1065 (1965).
17. A.G. MacKay, J.F. Boas, and G.J. Troup, *Aust. J. Chem.*, **27**, 955 (1974).
18. G.A. Corker, B. Grant, and N.J. Clecak, *J. Electrochem. Soc.*, **126**, 1339 (1979).
19. K. Kasuga and M. Tsutsui, *Coord. Chem. Rev.*, **32**, 67 (1980).
20. W.C. Moreira and R. Aroca, *Spectrochim. Acta.*, **51A**, 2325 (1995).
21. Y. Liu, K. Shigehara, M. Hara, and A. Yamada, *Thin Solid Films*, **179**, 387 (1989).

22. M. Bouvet and J. Simon, *Chem. Phys. Lett.*, **172**, 299 (1990).
23. M.M Thackeray, W.I.F. David, P.G. Bruce, and J.B. Goodenough, *Mater. Res. Bull.*, **18**, 461 (1983).
24. B. Scrosati, *Nature*, **373**, 557 (1995).
25. N. Oyama, T. Tatsuma, and T. Sotomura, *Nature*, **373**, 598 (1995).
26. T. Nagaura, M. Yokokawa, T. Hashimoto, *US Pat. No. 4,828,834* (1989).
27. J-M. Tarascon and D. Guyomard, *Electrochimica Acta*, **38**, 1221 (1993).
28. M. Faraday, *Phil. Trans. Roy. Soc. London*, **147**, 145 (1857).
29. R. Nahrwold, *Wied. Ann.*, **31**, 467 (1887).
30. I. Langmuir, *J. Am. Chem. Soc.*, **37**, 1139 (1915).
31. I. Langmuir, *J. Am. Chem. Soc.*, **38**, 2221 (1916).
32. I. Langmuir, *J. Am. Chem. Soc.*, **40**, 1361 (1918).
33. J.D. Swalen, D.L. Allara, J.D. Andrade, E.A. Chandross, S. Garoff, J. Israelachvili, T.J. McCarthy, R. Murray, R.F. Pease, J.F. Rabolt, K.J. Wynne, and H. Yu, *Langmuir*, **3**, 932 (1987).
34. D.B. Neal, M.C. Petty, G.G. Roberts, M.M. Ahmad, W.J. Feast, I.R. Girling, N.A. Cade, P.V. Kolinsky, and I.R. Peterson, *Electron. Lett.*, **22**, 460 (1986).
35. C.W. Pitt and L.M. Walpita, *Electron. Lett.*, **12**, 479 (1977).
36. P.L. Edmiston, J.E. Lee, L.L. Wood, and S.S. Saavedra, *J. Phys. Chem.*, **100**, 775 (1996).
37. J. Souto, R. Aroca, and J.A. DeSaja, *J. Phys. Chem.*, **98**, 8998 (1994).
38. H-Y. Wang and J.B. Lando, *Langmuir*, **10**, 790 (1994).
39. E. Orti, J.L. Bredas, C. Clarisse, *J. Chem. Phys.*, **92**, 1228 (1990).
40. N. Ishikawa, O. Ohno, Y. Kaizu, H. Kobayashi, *J. Phys. Chem.*, **96**, 8832 (1992).
41. A. Ghosh, P.G. Gassman, J. Almlöf, *J. Am. Chem. Soc.* **116**, 1932 (1944).
42. D. Battisti, L.G. Tomilova, R. Aroca, *Chem. Mater.* **4**, 1323 (1992).
43. A. Ulman, *An Introduction to Ultrathin Organic Films: From Langmuir-Blodgett to Self-assembly*, Academic Press, San Diego, 1991.

44. R. Aroca, R.E. Clavijo, C.A. Jennings, .G.J. Kovacs, J.M. Duff, R.O. Loufty, *Spectrochimica Acta*, **45A**, 962, (1989).
45. J. Souto, J., R. Aroca, J.A. DeSaja, *J. Raman Spectrosc.* **22**, 349 (1991).
46. R. Aroca, H. Bolourchi, Battisti, D., K. Najafi, *Langmuir* **9**, 3138, (1993).
47. M. M'Sadak, J. Roncali, F. Garnier, *J. Electroanal. Chem.* **189**, 99, (1985).
48. P.N. Moskalev, N.I. Alimova, *Russian J. Inorg. Chem.* **20** 1474, (1975).
49. H. Sugimoto, T. Higashi, M. Mori, *Chem. Letters, The Chem. Soc. Japan*, 801, (1982).
50. C.A. Jennings, G. J. Kovacs, R. Aroca, *Langmuir* **9**, 2151-2155, (1993).
51. T-H. Tran-Thi, D. Markovitsi, R. Even, J. Simon, *Chem. Phys. Lett.* **137**, 107, (1987).
52. T. Tran-thi, T.A. Mattioli, D. Chabach, A. De Cian, R. Weiss, *J. Phys. Chem.*, **98**, 8279, (1994).
53. K.L. Trojan, J.L. Kendall, K.D. Kepler, W.E. Hatfield, *Inorg. Chim. Acta* **198-200**, 795, (1992).
54. R. Rousseau, M. Rodriguez-Mendez, and R. Aroca, *J. Mol. Structure*, **356**, 49 (1995).
55. A. De Cian, M. Moussavi, J. Fischer, and R. Weiss, *Inorg. Chem.* **24**, 3162 (1985).
56. K. Kasuga, M. Tsutsui, R.C. Petterson, K. Tatsumi, N. Van Opdenbosch, G. Pepe, and E.F. Meyer Jr., *J. Am. Chem. Soc.*, **102**, 4836 (1980).
57. J. Tang and A. C. Allbrecht, *Raman Spectroscopy, Theory and Practice*, Vol. 2, Chapter 2, H. A. Szymanski, Ed.; Plenum Press, New York, (1970).
58. D.L. Rousseau, J.M. Friedman, and P.F. Williams, *Top. Curr. Phys.*, **11**, 203 (1979).
59. *Handbook of Optical Constants of Solids*, E.D. Palik, Editor, Academic Press, NY, (1985).
60. P.M. Fredericks, *Chem. Phys. Lett.*, **253**, 251 (1996).
61. W.B. Lacy, J.M. Williams, L.A. Wenzler, T.P. Beebe, J.M. Harris, *Anal. Chem.*, **68**, 1003 (1996).
62. P. Matejka, J. Stavek, K. Volka, B. Schrader, *Appl. Spectrosc.*, **50**, 409, (1996).

63. M. Moskovits, *J. Chem. Phys.*, **77**, 4408 (1982).
64. G. Varsányi, *Vibrational Spectra of Benzene Derivatives*, Academic Press, New York, (1969).
65. W.A. Snow and W.R. Barger in *Phthalocyanines: Properties and Applications*, C.C. Leznoff and A.B.P. Lever, Eds., VCH Publishers, Inc., New York, (1989); pp. 341.
66. J. Simon and J.J. Andre, *Molecular Semiconductors*, Springer-Verlag, Berlin, (1985); pp.73.
67. J.D. Wright, *Progress in Surface Science*, **31**, 1 (1989).
68. T.G. Abdel-Malik, *Int. J. Electronics*, **72**, 875 (1992).
69. J. Souto, M.L. Rodriguez, J.A. DeSaja, and R. Aroca, *Int. J. Electron.*, **76**, 763 (1994).
70. B. Berno, A. Nazri, R. Aroca, *J. Raman Spec.*, **27**, 41 (1996).
71. P. Turek, P. Petit, J.-J. André, J. Simon, R. Evan, B. Boudjema, G. Guillaud, M. Maitrot, *J. Am. Chem. Soc.*, **109**, 5119 (1987).
72. S. Robinet and C. Clarisse, *Thin Solid Films*, **170**, L51 (1989).
73. S. Dogo, J-P. Germain, C. Maleysson, and A. Pauly, *Thin Solid Films*, **219**, 251 (1992).
74. D.O. Hayward and B.M.W. Trapnell, *Chemisorption*, Butterworth, London, (1964).
75. A. Asmussen and H. Riegler, *J. Chem. Phys.*, **104**, 8151 (1996).
76. F.K. Shokoohi, J-M. Tarascon, *US Pat. No. 5,110,696* (1992).
77. J.B. Bates, N.J. Dudney, D.C. Lubben, G.R. Gruzalski, B.S. Kwak, X.-H. Yu, and R.A. Zuhr, *J. Power Sources*, **54**, 58 (1995).
78. A.R. Armstrong and P.G. Bruce, *Nature*, **381**, 381 (1996).
79. T. Ohzuku, M. Kitagawa, and T. Hirai, *J. Electrochem. Soc.*, **137**, 769 (1990).
80. McMurdie, Golovato, *J. Res. Natl. Bur. Stand. (U.S.)*, **41**, 589 (1948).
81. K. Wakamura, T. Arai, S. Onari, K. Kudo, and T. Takahashi, *J. Phys. Soc. Jap.*, **35**, 1430 (1973).
82. S.I. Boldish and W.B. White, *J. Solid State Chem.*, **25**, 121 (1978).
83. H.A. Lauwers and M.A. Herman, *J. Phys. Chem. Solids*, **41**, 223 (1980).

84. J. Himmrich and H.D. Lutz, *Solid State Comm.*, **79**, 447 (1991).
85. S.J. Wen, T.J. Richardson, L. Ma, K.A. Striebel, P.N. Ross Jr., and E.J. Cairns, *J Electrochem. Soc.*, **143**, L136 (1996).
86. (a) M.M. Thackeray, R.J. Gummow, A. De Kock, A.P. de la Harpe, D.C. Liles, and M.H. Rossouw, <personal communication>, (b) M.M. Thackeray, A. De Kock, and M.H. Rossouw, *J. Electrochem. Soc.*, **139**, 363 (1992).
87. M. Verbrugge, B. Koch, *G.M. Internal Report, PC-876*, (1995).
88. S.U. Campisano, G. Foti, E. Rimini, S.S. Lau, and J.W. Wayer, *Phil. Mag.*, **31**, 903 (1975).
89. P.J. Pokela, E. Kolawa, R. Ruiz, J.S. Reid, and M.-A. Nicolet, *Thin Solid Films*, **208**, 33 (1992).

Vita Auctoris

Personal Information:

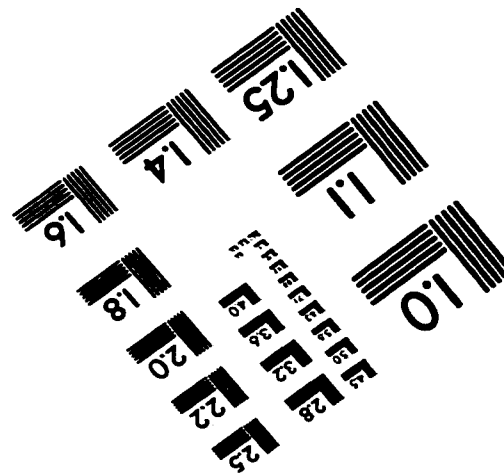
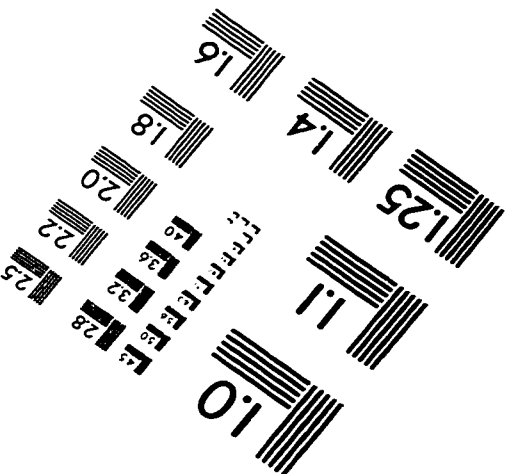
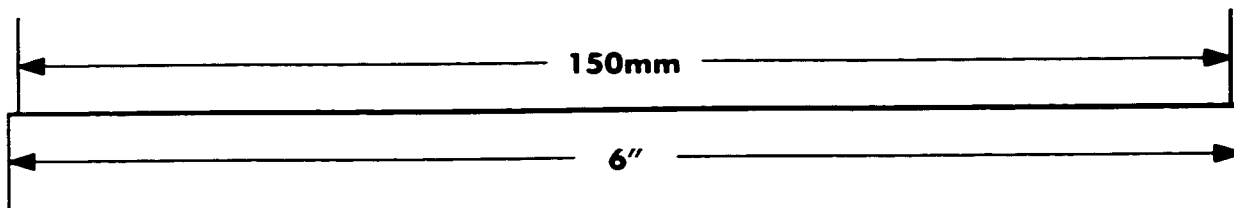
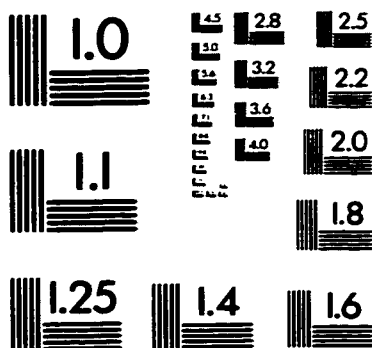
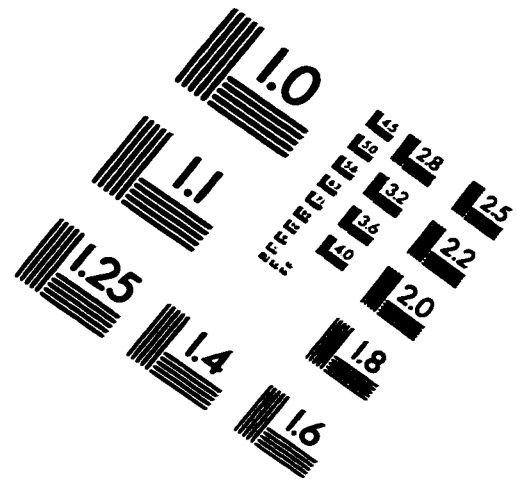
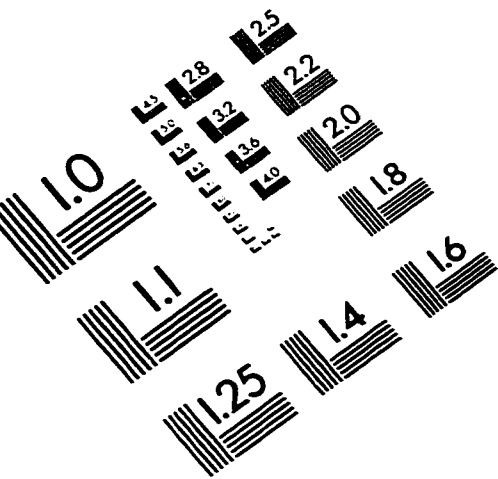
Name: Bob Berno
Date of Birth: 1964/12/18
Place of Birth: Guelph, Ontario, Canada

Education:

M.Sc., University of British Columbia, Vancouver, British Columbia, 1993,
under the direction of Dr. Anthony Merer. Thesis describes the details of the
high-resolution spectroscopic study of the $B^4\Pi-X^4\Sigma^-$ (0,0) band of vanadium
monoxide (VO).

B.Sc. (Honours Chemistry) University of Waterloo, Waterloo, Ontario, 1989.

IMAGE EVALUATION TEST TARGET (QA-3)



APPLIED IMAGE, Inc
 1653 East Main Street
 Rochester, NY 14609 USA
 Phone: 716/482-0300
 Fax: 716/288-5989

© 1993, Applied Image, Inc., All Rights Reserved